UNIVERSITY OF BIRMINGHAM

Simulation of Graphene Electronic Devices

by

Yudong Wu

A thesis submitted to the University of Birmingham
for the degree of Doctor of Philosophy

School of Electronic, Electrical and Computer Engineering
The University of Birmingham

Supervisor Dr. P.A Childs

Abstract

Since the publication of research in the mid-1980s describing the formation of freeform graphene there has been an enormous growth in interest in the material. Graphene is of interest to the semiconductor industry because of the high electron mobility exhibited by the material and, as it is planar, it is compatible with silicon technology. When patterned into nanoribbons graphene can be made into regions that are semiconducting or conducting and even into entire circuits. Graphene nanoribbons can also be used to form the channel of a MOSFET. This thesis describes numerical simulations undertaken on devices formed from graphene. The energy band structure of graphene and graphene nanoribbons is obtained using nearest-neighbour and third nearest-neighbour interactions within a tight binding model. A comparison of the current-voltage characteristics of MOS structures formed on graphene nanoribbons and carbon nanotubes suggests that the nanoribbon devices may be better for switching applications. Conductivities of graphene nanoribbons and junctions formed from them were obtained using a nonequilibrium Green's function formulation. The effects of defects and strain on these systems were also studied using this technique. Advancements were made when the self-energies used within the nonequilibrium Green's function were obtained from an iterative scheme including third nearest-neighbour interactions. An important result of this work is that accurate simulations of graphene based devices should include third nearest-neighbour interactions within the tight binding model of the energy band structure.

Acknowledgements

Firstly, I would like to thank my family for their continual support, especially for taking very good care of me when I was diagnosed with cancer during the last stage of my PhD study. A huge thank you should go to my supervisor, Dr Tony Childs, without whom I would never have been able to complete my thesis. Finally, I would like to thank the School of Electronic, Electrical and Computer Engineering and the Overseas Research Students Awards Scheme for the financial support during my PhD study.

Table of Contents

Chapter 1 Introduction

1.1 Significance of Graphene

Graphene is the name given to a flat monolayer of carbon atoms tightly packed into a two-dimensional honeycomb lattice, and is a basic building block for graphitic materials of all the other dimensionalities. It can be wrapped up into 0D buckyballs, rolled into 1D nanotubes or stacked into 3D graphite (Shown in Figure 1.1). Although it has been theoretically studied for sixty years [1], graphene was presumed not to exist in free state until Novoselov et.al in 2005 reported its formation and the anomalous features it exhibited [2, 3]. This experimental breakthrough has generated much excitement within the physics community. This can be clearly seen by studying the number of papers appearing in the search result on Web of Science containing the word "graphene" in the abstract shown in Figure 1.2.

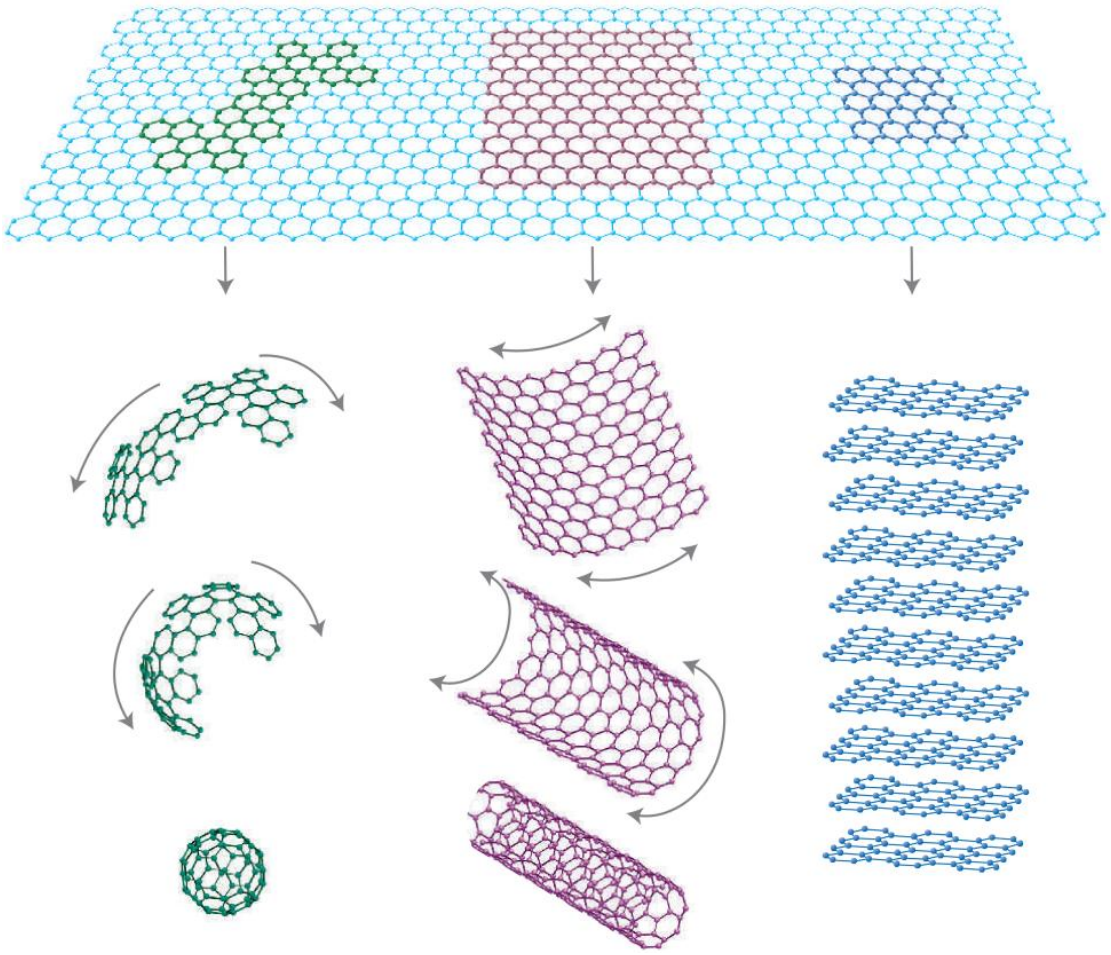

Figure 1.1 Graphene is a 2D building material for carbon materials of all other dimensionalities. [3]

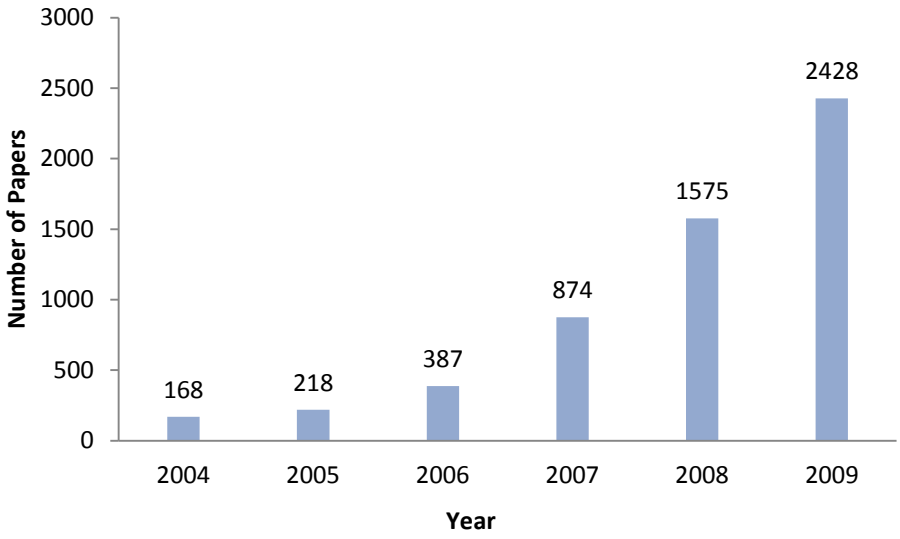

Figure 1.2 Number of Papers published during 2004-2009 containing the word "graphene" in the title. The result is obtained using Web of Science search engine.

Before the discovery of graphene, carbon nanotubes (CNTs) had attracted great interest in recent years because of their extraordinary mechanical and electrical properties. For electronic circuit applications it is the observed high electron mobility that makes CNT based devices attractive. The high mobility results from the energy band structure of the graphene coupled with quantization when the graphene sheet is rolled up to form a CNT. Simulations [4-9] of the electronic properties of metal-oxide-semiconductor (MOS) transistors based on CNTs suggest that they have great potential in future high speed electronic systems. However, in practice, it is difficult to control the chirality of carbon nanotubes and the structures cannot readily be integrated into an electronic system. The chirality is important because the energy bandgap of a semiconducting CNT is a function of it [10].

The advantage of graphene is that it is compatible with the planar technology employed within the semiconductor industry. Like CNTs graphene exhibits high electron mobilities [2, 11, 12], μ, in excess of 15,000cm^2/Vs and it can be metallic or semiconducting. When tailored to less than 100nm wide graphene nanoribbons may open a band gap due to the electron confinement. Electronic states of graphene largely depend on the edge structures and the width of the graphene nanoribbon [11]. One of the most important potential applications of graphene is as the channel for electron transport in a MOS structure. Structures of this kind have been demonstrated experimentally [13] using epitaxially synthesized graphene on silicon carbide substrates.

1.2 Energy Bandstructure of Graphene

Graphene has a honeycomb lattice structure of carbon atoms in the sp^2 hybridization state. Every unit cell of graphene lattice contains two carbon atoms and each atom contributes a free electron.

The bandstructure of graphene is unusual with the valence and the conduction bands meeting at a point at the six corners of the Brillouin zone (shown in Figure 1.3). Near these crossing points (named as Dirac points[3, 14, 15]), the electron energy is linearly dependent on the wave vector.

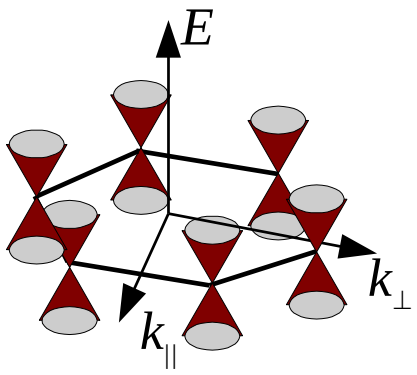

Figure 1.3 The valence and the conduction band of Graphene meet at a point at the six corners of the Brillouin zone

As a result of the linear energy-momentum dispersion relation, at the Dirac points an electron has an effective mass of zero and behaves more like a photon than a conventional massive particle whose energy-momentum dispersion is parabolic. The tight-binding calculation of the band structure of graphene is based on Schrödinger equation. At low energy levels, however, charge carrier transport can be described in a more natural way by using the Dirac equation.

1.3 Graphene Nanoribbons

As mentioned in section 1.1 when tailored to less than 100nm wide nanoribbons, graphene may open a band gap due to the electron confinement. This bandgap can be altered by simply changing the edge types or width, which makes it possible to use graphene as the channel of metal-oxide-semiconductor field-effect transistors (MOSFETs).

There are multiple types of Graphene nanoribbons (also called carbon nanoribbons, CNR). Like CNTs CNRs can be classified by the shape of their edges. Figures 1.4 (a) (b) [6], respectively, show armchair and zigzag nanoribbons N atoms wide. Figure 1.4 (c) shows a number of CNRs having more general edge forms.

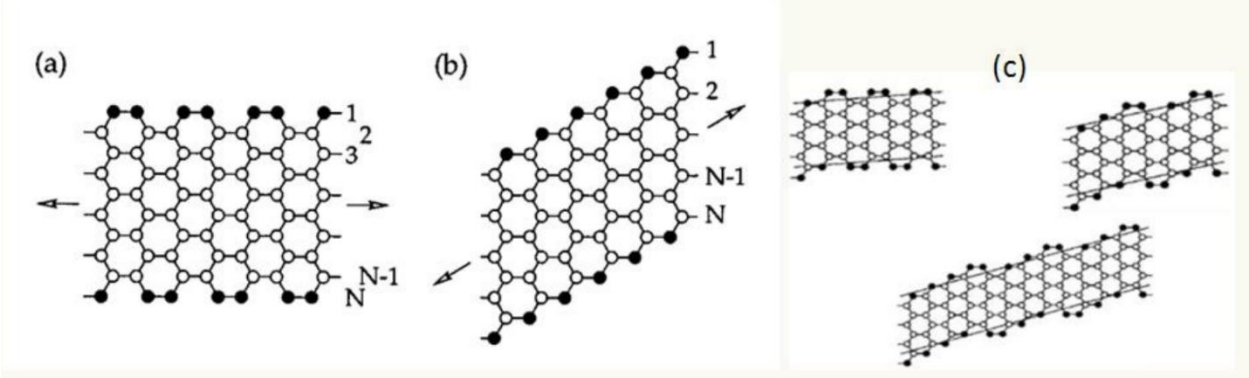

Figure 1.4 Different types of graphene nanoribbons[16].

Tight-binding calculations show that the conductivity of CNRs is highly dependent on their width and edge types. For armchair CNRs when N=3M-1 where M is an integer the CNRs will be metallic, otherwise they are semiconducting, and the energy band gap decreases as N increases. Unlike armchair CNRs, zigzag CNRs are all metallic; this is mainly because additional energy states appear on their edges[16].

1.4 Graphene Based Electronics Devices

By connecting graphene nanoribbons of different widths, graphene PN junctions or quantum dots can be formed. Figure 1.5 shows a graphene FET based on two armchair graphene nanoribbon junctions, the widths of the nanoribbons are carefully chosen so that the device has a semiconducting channel and conducting source and drain. The semiconducting channel is double gated in order to control the electric potential.

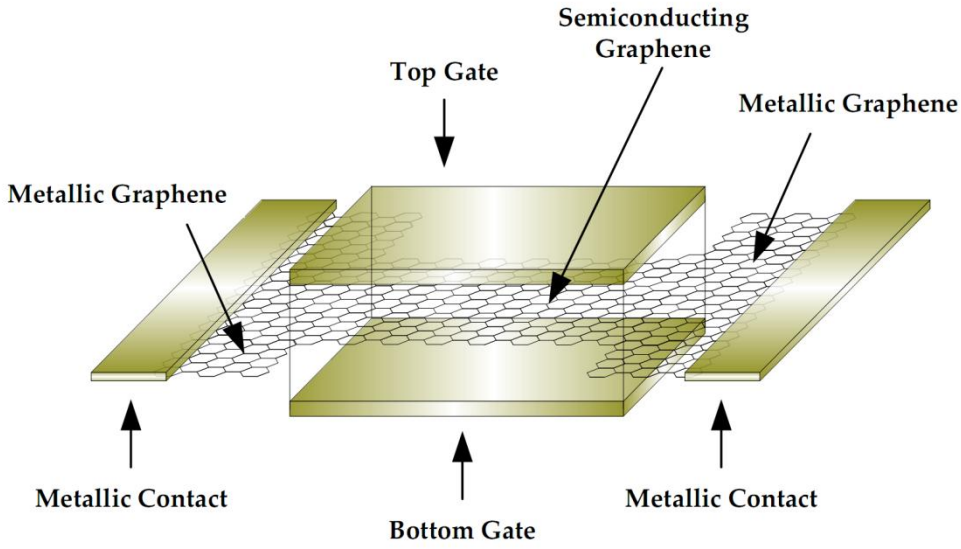

Figure 1.5 Graphene FET

Apart from changing the width, patterning graphene nanoribbons with different edge types is another way to form graphene electronic devices. Figure 1.6 illustrates an inverter circuit built from by patterning a structure containing conducting regions, semiconducting regions and junctions.

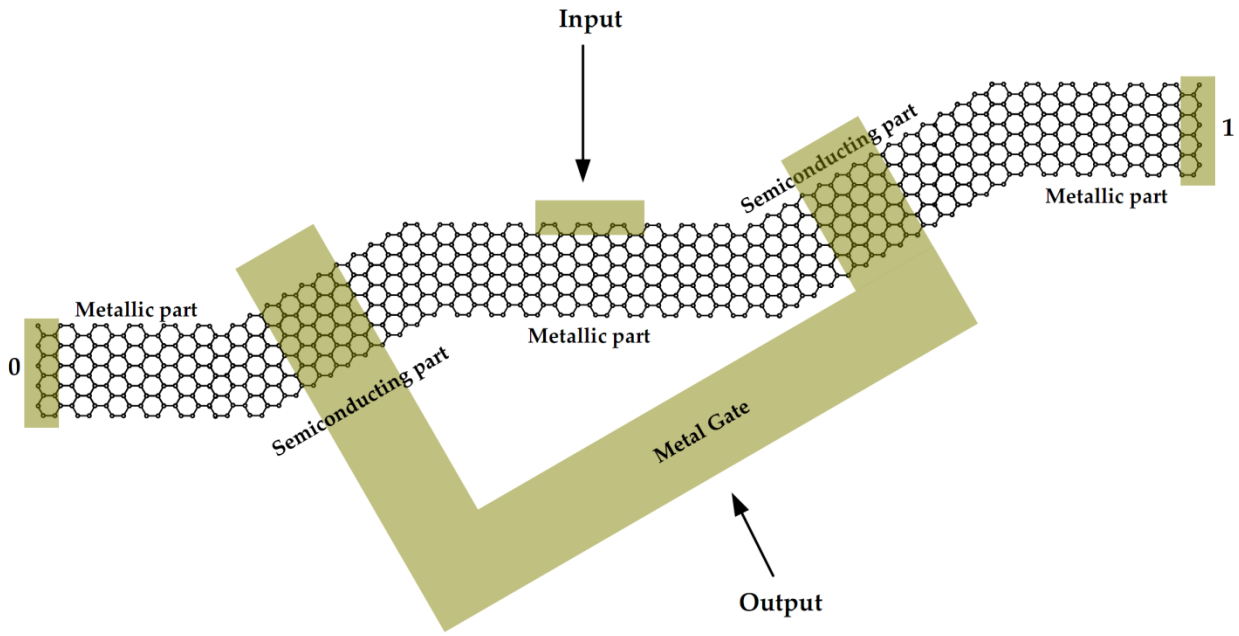

Figure 1.6 An inverter circuit built from Graphene Nanoribbons

1.5 Levels of Device Simulation

Simulation is an important tool for studying existing and future semiconductor devices. Devices can be simulated at different scale levels. Traditionally, the current-voltage characteristic of semiconductor devices has been obtained by a self consistent solution of Poisson's equation and the drift-diffusion equation. The latter has been used with various degrees of approximation. This classic approach to device simulation is computationally efficient and has been widely used within the semiconductor industry. More detailed solutions of the Boltzmann transport equation are usually obtained using the Monte Carlo method. This is computationally inefficient and is more likely to be used within academic institutions. As the physical dimensions of semiconductor devices decrease different modelling techniques have evolved. For instance, where quantum mechanical effects are deemed to be important Poisson's equation is solved self consistently with the Schrödinger equation. When device dimensions become comparable to the coherence length for charge carrier scattering the Landauer and Greens functions methods have come to the fore. It is these methods coupled with ab initio and atomic level calculations that are the focus for the research reported in this thesis.

This thesis reports simulations of the current-voltage characteristic of graphene based devices.

1.6 Thesis outline

Chapter 2 describes calculations of the energy band structure of graphene and graphene nanoribbons. The basis of the analysis is the tight binding method and different levels of approximation reported in this work. Initially, a nearest-neighbour approximation is used but it is found that the third nearest-neighbour approximation gives better agreement with ab initio calculations of the energy band structure. Numerical calculations of the band structure of armchair and zigzag nanoribbons reveal a strong dependence of the energy band gap on the width of the carbon nanoribbon. To increase computational efficiency a quasi-one dimensional model is developed resulting in energy band structures almost identical to those obtained using the more detailed simulation. The effects of edge distortion and strain are also considered and the chapter is concluded with an effective mass approximation suitable for use in the Poisson-Schrödinger solver developed in chapter 3. Within this chapter a description of the finite difference method employed to solve Poisson's equation is presented. Schrödinger's equation is solved using the scattering matrix method and the current-voltage characteristics subsequently obtained. The results are compared with those obtained from carbon nanotube structures and differences in the characteristics are attributed to the different forms of transmission coefficient. In chapter 4 the conductance and local density of states of graphene nanoribbons are obtained using a Green's function analysis. One of the key achievements reported in this thesis is the inclusion of third nearest-neighbour interactions within the Sancho-Rubio iterative scheme used to obtain the self energies. A key conclusion of this work is that third nearest-neighbour interactions must be included within simulations of the conductance of graphene nanoribbons. This chapter also describes the effects of defects and strain on the conductance of graphene nanoribbons. Finally, chapter 5 outlines the conclusions of this work and suggestions for future work. A natural development of the research reported here is a self-consistent solution of the charge transport problem within graphene nanoribbons. This work has been undertaken but it has not been possible to include it within this thesis. The research reported in this thesis has led to two journal publications. The first entitled 'Modeling charge transport in graphene nanoribbons and carbon nontubes using a Schrödinger-Poisson solver', was published in the Journal of Applied Physics [42] and the second entitled 'Conductance of graphene nanoribbon junctions and the tight binding model', was published in Nanoscale Research Letters [43].

Chapter 2 Bandstructure of Graphene and Graphene Nanoribbons

In this chapter the energy bandstructures of graphene and graphene nanoribbons are calculated using the tight-binding method. Both analytical and numerical results are obtained.

2.1 The Secular Equation

We start from the time independent Schrodinger's equation

$$E(\vec{k})\boldsymbol{\psi}(\vec{k},\vec{r}) = H_{op}\boldsymbol{\psi}(\vec{k},\vec{r}) \tag{2.1}$$

where H_{op} is the Hamiltonian operator, $E(\vec{k})$ and $\boldsymbol{\psi}(\vec{k},\vec{r})$ are the eigen energy and eigenfunctions in a graphene lattice and $\vec{k}$ and $\vec{r}$ represent the wave vector and position, respectivey. The *j*-th eigenvalue $E_j(\vec{k})$ as a function of $\vec{k}$ is given by

$$E_j(\vec{k}) = \frac{\langle\psi_j|H_{op}|\psi_j\rangle}{\langle\psi_j|\psi_j\rangle} = \frac{\int \psi_j^* H_{op}\psi_j d\boldsymbol{r}}{\int \psi_j^*\psi_j d\boldsymbol{r}} \tag{2.2}$$

Because of the translational symmetry of the carbon atoms in a graphene lattice, the eigenfunctions, $\psi_j(\vec{k},\vec{r})$ $(j = 1,\dots,n)$, where *n* is the number of Bloch wavefunctions can be written as a linear combination of Bloch orbital basis functions $u_m(\vec{r})$[datta].

$$\psi_j(\vec{k},\vec{r}) = \sum_{j'=1}^{n} \phi_{jj'}(\vec{k})u_{j'}(\vec{k},\vec{r}) \tag{2.3}$$

where $\phi_{jj'}(\vec{k})$ are coefficients to be determined, and $u_{j'}(\vec{k},\vec{r})$ satisfy

$$u_{j'}(\vec{k},\vec{r}+\vec{a}_i) = u_{j'}(\vec{k},\vec{r}) \quad (i = 1,2) \tag{2.4}$$

Substituting (2.3) into (2.2) and changing subscripts we obtain

$$E_i(\vec{k}) = \frac{\sum_{j,j'}^{n} \phi_{ij}^*\phi_{ij'}\langle u_j|H_{op}|u_{j'}\rangle}{\sum_{j,j'}^{n} \phi_{ij}^*\phi_{ij'}\langle u_j|u_{j'}\rangle} = \frac{\sum_{j,j'}^{n} H_{jj'}(\vec{k})\phi_{ij}^*\phi_{ij'}}{\sum_{j,j'}^{n} S_{jj'}(\vec{k})\phi_{ij}^*\phi_{ij'}} \tag{2.5}$$

Here the integrals over the Bloch orbitals, $H_{jj'}(\vec{k})$ and $S_{jj'}(\vec{k})$ are called the transfer integral matrix and overlap integral matrix, respectively, which are defined by [10]

$$H_{jj'}(\vec{k}) = \langle u_j | H_{op} | u_{j'} \rangle,\ S_{jj'}(\vec{k}) = \langle u_j | u_{j'} \rangle\ \ (j, j' = 1, \dots, n) \tag{2.6}$$

$H_{jj'}(\vec{k})$ and $S_{jj'}(\vec{k})$ have fixed values, for a given value of $\vec{k}$, and the coefficient ϕ_{ij}^* is optimized so as to minimize $E_i(\vec{k})$. Taking a partial derivative with respect to ϕ_{ij}^* to obtain the local minimum condition gives,

$$\frac{\partial E_i(\vec{k})}{\partial \phi_{ij}^*} = \frac{\sum_{j'=1}^{n} H_{jj'}(\vec{k})\phi_{ij'}}{\sum_{j,j'=1}^{n} S_{jj'}(\vec{k})\phi_{ij}^*\phi_{ij'}} - \frac{\sum_{i,j'=1}^{n} H_{jj'}(\vec{k})\phi_{ij}^*\phi_{ij'}}{\left(\sum_{j,j'=1}^{n} S_{jj'}(\vec{k})\phi_{ij}^*\phi_{ij'} \right)^2} \sum_{j'=1}^{n} S_{jj'}(\vec{k})\phi_{ij'} = 0 \tag{2.7}$$

Multiplying both sides of (2.7) by $\sum_{j,j'=1}^{n} S_{jj'}(\vec{k})\varphi_{ij}^*\varphi_{ij'}$ and substituting (2.5) into the second term of (2.7) we obtain

$$\sum_{j'=1}^{n} H_{jj'}(\vec{k})\phi_{ij'} = E_i(\vec{k}) \sum_{j'=1}^{n} S_{jj'}(\vec{k})\phi_{ij'} \tag{2.8}$$

(2.8) can be written into matrix form such that

$$\boldsymbol{H\phi_i} = E_i(\vec{k})\boldsymbol{S\phi_i} \tag{2.9}$$

where $\boldsymbol{\phi_i}$ is a column vector defined by

$$\boldsymbol{\phi_i} = [\phi_{i1} \cdots \phi_{in}]^T \tag{2.10}$$

(2.9) only has a non zero solution when

$$\det [\boldsymbol{H} - E_i(\vec{k})\boldsymbol{S}] = 0 \tag{2.11}$$

(2.11) is called the secular equation, whose solution gives all n eignvalues of $E_i(\vec{k})$ $(i = 1, \dots n)$ for a given wave vector $\vec{k}$.

2.2 Analytical solution of the Secular Equation for Graphene

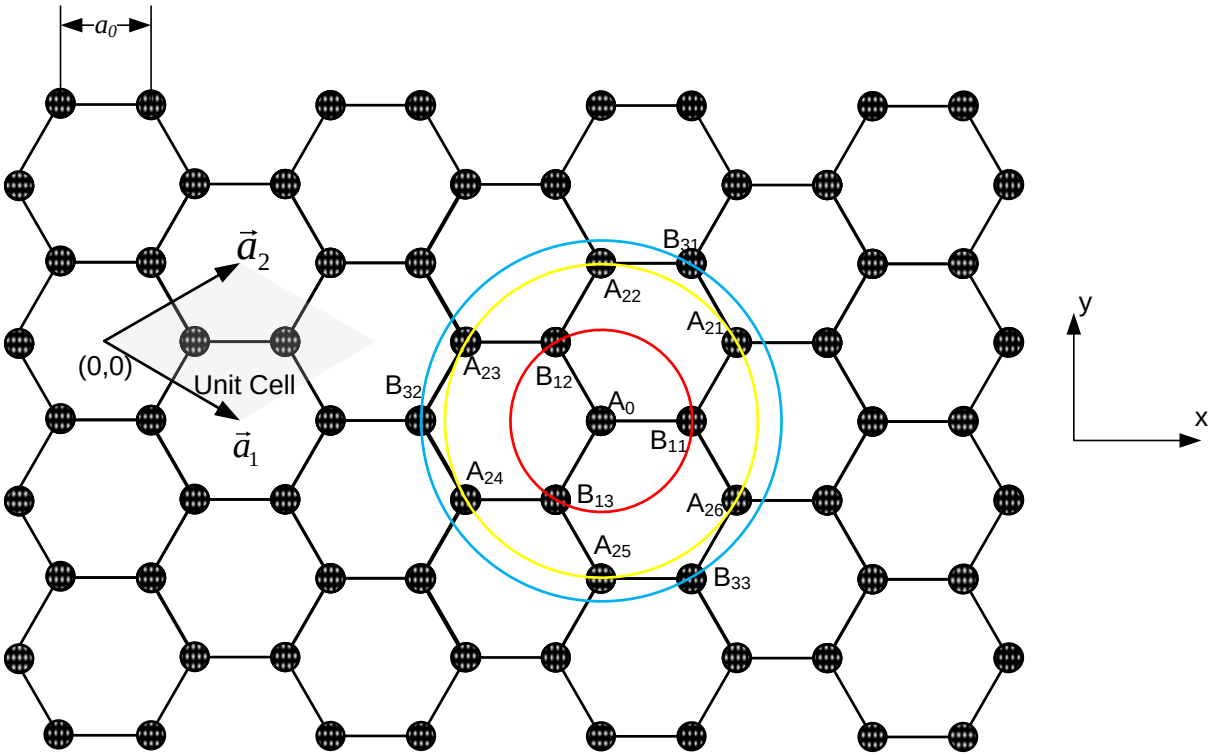

Figure 2.1 Graphene lattice. Carbon atoms are located at the crossings and the chemical bonds represented by the lines are derived from the Pz orbitals. The primitive lattice vectors are $\vec{a}_{1,2}$ and the unit-cell is the shaded region. There are two carbon atoms per unit-cell, represented by A and B. The concentric circles of increasing radius show first, second and third nearest neighbours of atom A_0 respectively.

Consider the graphene lattice structure shown in figure 2.1. Because there are two carbon atoms per unit cell at A and B, two Bloch functions $u_A(\vec{k},\vec{r})$ and $u_B(\vec{k},\vec{r})$ can be used as the basis functions for graphene.

$$u_A(\vec{k},\vec{r}) = \frac{1}{\sqrt{N}}\sum_A e^{i\vec{k}\cdot\vec{r}_A}\varphi_A(\vec{r}-\vec{r}_A)$$

$$u_B(\vec{k},\vec{r}) = \frac{1}{\sqrt{N}}\sum_B e^{i\vec{k}\cdot\vec{r}_B}\varphi_B(\vec{r}-\vec{r}_B) \qquad (2.12)$$

where N is the number of unit cells in the crystal, φ_A and φ_B are $2p_z$ atomic orbitals and r_A and r_B are the positions of A and B type atoms, respectively. Using these basis functions and (2.3), the eigenfunctions can be written as

$$\psi_j(\vec{k},\vec{r}) = \phi_{jA}(\vec{k})u_A(\vec{k},\vec{r}) + \phi_{jB}(\vec{k})u_B(\vec{k},\vec{r}) \tag{2.13}$$

Thus the transfer integral matrix *H* and overlap integral matrix *S* in (2.11) become 2x2 matrices.

$$H = \begin{bmatrix} H_{AA} & H_{AB} \\ H_{BA} & H_{BB} \end{bmatrix}, \qquad S = \begin{bmatrix} S_{AA} & S_{AB} \\ S_{BA} & S_{BB} \end{bmatrix} \tag{2.14}$$

Matrix elements H_{jj}, $and\ S_{jj'}(j,j' = A,B)$ are determined using (2.6)

$$H_{jj'}(\vec{k}) = \langle u_j | H_{op} | u_{j'} \rangle,\ S_{jj'}(\vec{k}) = \langle u_j | u_{j'} \rangle\ \ (j,j' = A,B) \tag{2.15}$$

Since the two carbon atoms in a graphene unit cell are equivalent, $H_{AA} = H_{BB}$ and $S_{AA} = S_{BB}$, also , $H_{BA} = H_{AB}^*$ and $S_{BA} = S_{AB}^*$ in which * donates the complex conjugate. Substituting (2.12) into (2.15) we have

$$H = \begin{bmatrix} H_{AA} & H_{AB} \\ H_{AB}^* & H_{AA} \end{bmatrix}, S = \begin{bmatrix} S_{AA} & S_{AB} \\ S_{AB}^* & S_{AA} \end{bmatrix}$$

$$H_{AA}(\vec{k}) = \frac{1}{N}\sum_A \sum_{A'} e^{i\vec{k}(\vec{r}_{A'} - \vec{r}_A)} \langle \varphi_A(\vec{r} - \vec{r}_A) | H_{op} | \varphi_A(\vec{r} - \vec{r}_{A'}) \rangle$$

$$H_{AB}(\vec{k}) = \frac{1}{N}\sum_A \sum_B e^{i\vec{k}\cdot(\vec{r}_B - \vec{r}_A)} \langle \varphi_A(\vec{r} - \vec{r}_A) | H_{op} | \varphi_A(\vec{r} - \vec{r}_B) \rangle \tag{2.16}$$

$$S_{AA}(\vec{k}) = \frac{1}{N}\sum_A \sum_{A'} e^{i\vec{k}\cdot(\vec{r}_{A'} - \vec{r}_A)} \langle \varphi_A(\vec{r} - \vec{r}_A) | \varphi_A(\vec{r} - \vec{r}_{A'}) \rangle$$

$$S_{AB}(\vec{k}) = \frac{1}{N}\sum_A \sum_B e^{i\vec{k}\cdot(\vec{r}_B - \vec{r}_A)} \langle \varphi_A(\vec{r} - \vec{r}_A) | \varphi_A(\vec{r} - \vec{r}_B) \rangle$$

2.2.1 Nearest neighbour approximation

When only the first nearest neighbour carbon atoms are considered, the summation in (2.16) to obtain H_{AA} will only contain one term,

$$H_{AA}(\vec{k}) = \frac{1}{N}\sum_{A}\langle\varphi_A(\vec{r}-\vec{r}_A)|H_{op}|\varphi_A(\vec{r}-\vec{r}_A)\rangle = E_{sp} \tag{2.17}$$

Similarly, $S_{AA} = 1$ because $\varphi_A(\vec{r}-\vec{r}_A)$ is assumed to be normalized, $\langle\varphi_A(\vec{r}-\vec{r}_A)|\varphi_A(\vec{r}-\vec{r}_{A'})\rangle = 1$

H_{AB} is simply a summation of three terms of the B type nearest neighbours shown by B_{11} B_{12} B_{13} in Figure 2.1

$$H_{AB}(\vec{k}) = \frac{1}{N}\sum_{A}\sum_{i=1}^{3} e^{i\vec{k}\left(\vec{r}_{B_{1i}}-\vec{r}_A\right)}\langle\varphi_A(\vec{r}-\vec{r}_A)|H_{op}|\varphi_A(\vec{r}-\vec{r}_{B_{1i}})\rangle \tag{2.18}$$

From Figure 2.1 we have $\vec{r}_{B_{11}} - \vec{r}_{A_0} = a_0\vec{x}$, $\vec{r}_{B_{12}} - \vec{r}_{A_0} = -\frac{1}{2}a_0\vec{x} + \frac{\sqrt{3}}{2}a_0\vec{y}$, and $\vec{r}_{B_{13}} - \vec{r}_{A_0} = -\frac{1}{2}a_0\vec{x} - \frac{\sqrt{3}}{2}a_0\vec{y}$. Substituting into (2.18) and defining $\gamma_0$as the hopping integral energy (eV)

$$\gamma_0 = \langle\varphi_A(\vec{r}-\vec{r}_A)|H_{op}|\varphi_A(\vec{r}-\vec{r}_{B_{1i}})\rangle \tag{2.19}$$

we obtain

$$H_{AB}(\vec{k}) = \gamma_0 f(\vec{k}) \; with \; f(\vec{k}) = e^{ik_x a_0} + 2e^{-\frac{1}{2}ik_x a_0}cos\frac{\sqrt{3}}{2}k_y a_0 \tag{2.20}$$

Similarly defining S_0 as the overlap integral

$$s_0 = \langle\varphi_A(\vec{r}-\vec{r}_A)|\varphi_A(\vec{r}-\vec{r}_{B_{1i}})\rangle \tag{2.21}$$

we have

$$S_{AB}(\vec{k}) = s_0 f(\vec{k}) \tag{2.22}$$

So that the explicit forms for H and S can be written as

$$H = \begin{bmatrix} E_{sp} & \gamma_0 f(\vec{k}) \\ \gamma_0 f(\vec{k})^* & E_{sp} \end{bmatrix}, S = \begin{bmatrix} 1 & sf(\vec{k}) \\ s_0 f(\vec{k})^* & 1 \end{bmatrix} \tag{2.23}$$

Solving the secular equation (2.11) and using H and S given in (2.23), the eigen energies are obtained as a function of wave vector.

$$E(\vec{k}) = \frac{E_{sp} \pm \gamma_0\sqrt{g(\vec{k})}}{1 \pm s_0\sqrt{g(\vec{k})}} \tag{2.24}$$

$$g(\vec{k}) = \left|f(\vec{k})\right|^2 = 1 + 4cos\frac{3k_x a_0}{2}cos\frac{\sqrt{3}k_y a_0}{2} + 4cos^2\frac{\sqrt{3}k_y a_0}{2}$$

2.2.2 Third nearest neighbour approximation

The nearest neighbour tight-binding approximation is only valid at low energy[17]. in order to match with experiment and first principle calculations the model needs to be extended to consider up to third nearest neighbour carbon atoms.

We start the calculation from the summation of H_{AA} in (2.16). Consider a type A atom (shown as A_0 in figure 2.2). As we now need to include six second nearest neighbour type A atoms (shown as A_{21} to A_{26} in figure 2.2) of A_0 an additional term is added in to (2.17) giving

$$\begin{aligned} H_{AA}(\vec{k}) &= E_{sp} + \frac{1}{N}\sum_{A}\sum_{i=1}^{6} e^{i\vec{k}\left(\vec{r}_{A_{2i}} - \vec{r}_A\right)}\left\langle\varphi_A(\vec{r} - \vec{r}_A)\middle|H_{op}\middle|\varphi_A\left(\vec{r} - \vec{r}_{A_{2i}}\right)\right\rangle \\ &= E_{sp} + \gamma_1 v(\vec{k}) \end{aligned} \tag{2.25}$$

where $\gamma_1 = \left\langle\varphi_A(\vec{r} - \vec{r}_A)\middle|H_{op}\middle|\varphi_A\left(\vec{r} - \vec{r}_{A_{2i}}\right)\right\rangle$ is the hopping integral energy for second nearest carbon atoms, and $v(\vec{k})$ is defined by

$$\begin{aligned} v(\vec{k}) &= \sum_{i=1}^{6} e^{i\vec{k}\left(\vec{r}_{A_{2i}} - \vec{r}_{A_0}\right)} \\ &= 2\cos\left(k_y\sqrt{3}a_0\right) + 4\cos(k_x 3a_0/2)\cos\left(k_y\frac{\sqrt{3}a_0}{2}\right) \end{aligned} \tag{2.26}$$

Similarly, defining $s_1 = \left\langle\varphi_A(\vec{r} - \vec{r}_A)\middle|\varphi_A\left(\vec{r} - \vec{r}_{A_{2i}}\right)\right\rangle$ as the overlap integral for second neighbour we have

$$S_{AA}(\vec{k}) = 1 + s_1 v(\vec{k}) \tag{2.27}$$

For the summation of H_{AB} in (2.17), an additional term is added to include the three third nearest B type carbon atoms (shown as B_{31} B_{32} B_{33}) of A_0

$$H_{AB}(\vec{k}) = \gamma_0 f(\vec{k}) + \frac{1}{N}\sum_{A}\sum_{i=1}^{3} e^{i\vec{k}\left(\vec{r}_{B_{3i}} - \vec{r}_A\right)}\left\langle \varphi_A(\vec{r} - \vec{r}_A)\middle| H_{op}\middle|\varphi_B(\vec{r} - \vec{r}_{B_{3i}})\right\rangle$$
$$= \gamma_0 f(\vec{k}) + \gamma_2 w(\vec{k}) \tag{2.28}$$

where $\gamma_2 = \left\langle \varphi_A(\vec{r} - \vec{r}_A)\middle| H_{op}\middle|\varphi_B(\vec{r} - \vec{r}_{B_{3i}})\right\rangle$ is the hopping integral energy for third nearest carbon atoms, and $w(\vec{k})$ is defined by

$$w(\vec{k}) = \sum_{i=1}^{3} e^{i\vec{k}\left(\vec{r}_{B_{3i}} - \vec{r}_{A_0}\right)}$$
$$= 2e^{ik_x a_0} cos 2\sqrt{3}k_y a_0 + e^{-2ik_x a_0} \tag{2.29}$$

S_{AB} can be obtained in the same way

$$S_{AB}(\vec{k}) = s_0 f(\vec{k}) + s_2 w(\vec{k}) \tag{2.30}$$

with $s_2 = \left\langle \varphi_A(\vec{r} - \vec{r}_A)\middle|\varphi_B(\vec{r} - \vec{r}_{B_{3i}})\right\rangle$.

Overall, the matrices H and S extended to include third nearest neighbours can be written as

$$H = \begin{bmatrix} E_{sp} + \gamma_1 v(\vec{k}) & \gamma_0 f(\vec{k}) + \gamma_2 w(\vec{k}) \\ \gamma_0 f(\vec{k})^* + \gamma_2 w(\vec{k})^* & E_{sp} + \gamma_1 v(\vec{k}) \end{bmatrix}$$
$$S = \begin{bmatrix} 1 + s_1 v(\vec{k}) & s_0 f(\vec{k}) + s_2 w(\vec{k}) \\ s_0 f(\vec{k})^* + s_2 w(\vec{k})^* & 1 + s_1 v(\vec{k}) \end{bmatrix} \tag{2.31}$$

The solution of the secular equation (2.11) is given by

$$E^{\pm}(\vec{k}) = \frac{\left[(2E_0 - E_1) \pm \sqrt{(E_1 - 2E_0)^2 - 4E_1E_2}\right]}{2E_3}$$

$$\begin{aligned} E_1 &= 2s_0\gamma_0 g(\vec{k}) + (s_2\gamma_2 + \gamma_0 s_2)t(k) + 2s_2\gamma_2 g(2k) \\ E_2 &= \left[E_{sp} + \gamma_1 v(\vec{k})\right]^2 - \left[\gamma_0^2 g(\vec{k}) + \gamma_0\gamma_2 t(\vec{k}) + \gamma_2^2 g(2\vec{k})\right] \\ E_3 &= [1 + s_1 v(\vec{k})]^2 - [s_0^2 g(\vec{k}) + s_0 s_2 t(\vec{k}) + s_2^2 g(2\vec{k})] \end{aligned} \tag{2.32}$$

where

$$\begin{aligned} t(\vec{k}) = {} & 2\cos(k_x a_0) + 4\cos(k_y\sqrt{3}a_0) + 4\cos\left(k_y\frac{\sqrt{3}}{2}a_0\right)\cos\left(k_x\frac{a_0}{2}\right) \\ & +8\cos(k_y\sqrt{3}a_0)\cos\left(k_y\frac{\sqrt{3}}{2}a_0\right)\cos\left(k_x\frac{a_0}{2}\right) \end{aligned} \tag{2.33}$$

2.2.3 Results

In the paper by Reich [18] tight binding parameters were obtained by fitting the band structure to that obtained by *ab initio* calculations. Recently, Kundo [19] has reported a set of tight biding parameters based on fitting to a first principle calculation but more directly related to the physical quantities of interest. These parameters have been utilised in our calculation and are presented in table 2.1. Using these parameters the energy dispersion relationship is obtained and shown in Figure 2.2.

Table 2.1 Tight-binding parameters

Neighbours	E_{sp}(eV)	γ_0(eV)	γ_1(eV)	γ_2(eV)	s_0	s_1	s_2
1st-nearest	0	-2.74			0.065		
3rd-nearest	-0.45	-2.78	-0.15	-0.095	0.117	0.004	0.002

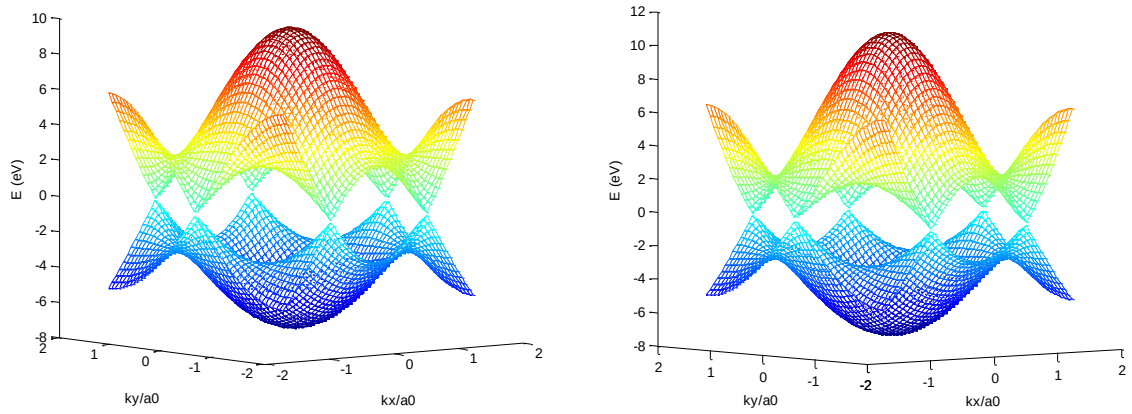

Figure 2.2 Energy dispersion relationship obtained based on (a) first nearest neighbour and (b) third nearest neighbour tight binding method

2.3 Numerical solution for the bandstructure of Graphene nanoribbons

When tailored into an armchair or zigzag nanoribbon of finite width, the translational symmetry only exists in x direction in graphene as shown in Figure 2.3. As a result a unit cell covering the whole width of the nanoribbon is chosen for tight-binding bandstructure calculation. The unit cell contains $2N_0$ (N_0 is the graphene nanoribbon index number defined in 1.3) carbon atoms which leads to a $2N_0 x 2N_0$ integral matrix *H* and overlap integral matrix *S*. In the literature most authors report matrices developed for this unit cell based on the first nearest neighbour assumption [17, 20-23]. However, in this section we extend the calculation to include up to third-nearest neighbours. An equivalent but computationally less expensive method is also developed.

2.3.1 Armchair nanoribbons

Consider an N_0=5 armchair graphene nanoribbon shown in Figure 2.3 as an example. The wavefunction can be written as a linear combination of $2N_0$ π orbital functions contributed by the carbon atoms in the unit cell (we assume the carbon atoms on the edge are hydrogen-terminated so all σ bonds are filled).

$$\psi(\vec{k}_x,\vec{r}) = \sum_{j=1}^{2N_0} \phi_j(\vec{k}_x) u_j(\vec{k}_x,\vec{r}) \tag{2.34}$$

$$u_j(\vec{k}_x,\vec{r}) = \frac{1}{\sqrt{N}} \sum_{\vec{r}_j} e^{i\vec{k}_x\cdot\vec{r}_j} \varphi_j(\vec{r}-\vec{r}_j) \quad (j = 1,2,\dots,2N_0)$$

Using (2.6) and (2.34) the $\boldsymbol{2N_0x2N_0}$ elements in the matrix integral H and overlap matrix integral S can be calculated. Here we derive the non-zero elements in the first row $H_{1,1}$,$H_{1,2}$, $H_{1,3}$, $H_{1,6}$, $H_{1,7}$ and $H_{1,8}$, all other none zero elements can be derived in the same manner.

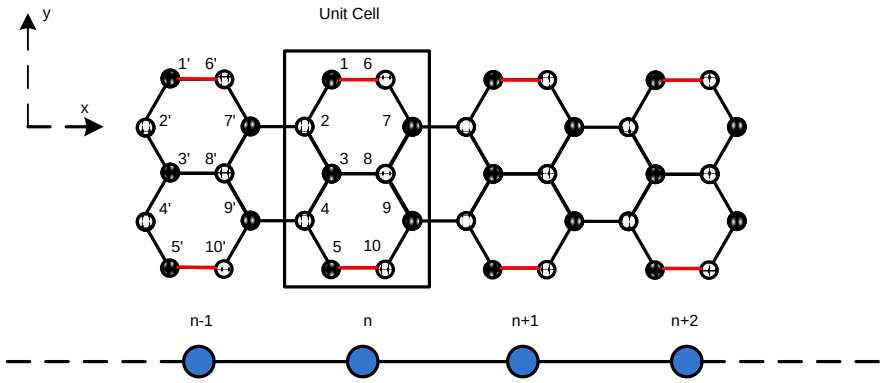

Figure 2.3 An N_0=5 armchair graphene nanoribbon. By choosing the unit cell shown as the rectangular box the nanoribbon can be treated as a 1D quantum wire. The red lines indicate edge bonding.

$$
\begin{aligned}
H_{1,1} &= \frac{1}{N}\sum_{\vec{r}_1}\left\langle \varphi_1(\vec{r}-\vec{r}_1)\middle| H_{op}\middle|\varphi_1(\vec{r}-\vec{r}_1)\right\rangle = E_{sp} \\
H_{1,2} &= \frac{1}{N}\sum_{\vec{r}_1} e^{i\vec{k}_x\cdot(\vec{r}_2-\vec{r}_1)}\left\langle \varphi_1(\vec{r}-\vec{r}_1)\middle| H_{op}\middle|\varphi_1(\vec{r}-\vec{r}_2)\right\rangle = e^{-ik_x\frac{a_0}{2}}\gamma_0 \\
&= a\gamma_0 \\
H_{1,3} &= \frac{1}{N}\sum_{\vec{r}_1} e^{i\vec{k}_x\cdot(\vec{r}_3-\vec{r}_1)}\left\langle \varphi_1(\vec{r}-\vec{r}_1)\middle| H_{op}\middle|\varphi_1(\vec{r}-\vec{r}_3)\right\rangle = \gamma_1 \\
H_{1,8} &= \frac{1}{N}\sum_{\vec{r}_1} e^{i\vec{k}_x\cdot(\vec{r}_8-\vec{r}_1)}\left\langle \varphi_1(\vec{r}-\vec{r}_1)\middle| H_{op}\middle|\varphi_1(\vec{r}-\vec{r}_8)\right\rangle = e^{ik_x a_0}\gamma_2 \\
&= b\gamma_2 \\
H_{1,7} &= \frac{1}{N}\sum_{\vec{r}_1}[e^{i\vec{k}_x\cdot(\vec{r}_7-\vec{r}_1)}\left\langle \varphi_1(\vec{r}-\vec{r}_1)\middle| H_{op}\middle|\varphi_1(\vec{r}-\vec{r}_7)\right\rangle \\
&\qquad + e^{i\vec{k}_x\cdot(\vec{r}_7{}'-\vec{r}_1)}\left\langle \varphi_1(\vec{r}-\vec{r}_1)\middle| H_{op}\middle|\varphi_1(\vec{r}-\vec{r}_7{}')\right\rangle] \\
&= \left(e^{-ik_x\frac{3a_0}{2}} + e^{ik_x\frac{3a_0}{2}}\right)\gamma_1 = 2\cos\left(k_x\frac{3a_0}{2}\right)\gamma_1 \\
&= d\gamma_1 \\
H_{1,6} &= \frac{1}{N}\sum_{\vec{r}_1}[e^{i\vec{k}_x\cdot(\vec{r}_6-\vec{r}_1)}\left\langle \varphi_1(\vec{r}-\vec{r}_1)\middle| H_{op}\middle|\varphi_1(\vec{r}-\vec{r}_6)\right\rangle \\
&\qquad + e^{i\vec{k}_x\cdot(\vec{r}_6{}'-\vec{r}_1)}\left\langle \varphi_1(\vec{r}-\vec{r}_1)\middle| H_{op}\middle|\varphi_1(\vec{r}-\vec{r}_6{}')\right\rangle] \\
&= e^{ik_x a_0}\gamma_0 + e^{-ik_x 2a_0} = b\gamma_0 + c\gamma_2
\end{aligned}
\tag{2.35}
$$

The non-zero elements of the 10x10 integral matrix *H* can be written as

$$
H = \begin{bmatrix}
E_{sp} & a\gamma_0 & \gamma_1 & & & b\gamma_0+c^*\gamma_2 & d\gamma_1 & b\gamma_2 & & \\
a^*\gamma_0 & E_{sp} & a^*\gamma_0 & \gamma_1 & & d\gamma_1 & b^*\gamma_0+c\gamma_2 & d\gamma_1 & b\gamma_2 & \\
\gamma_1 & a\gamma_0 & E_{sp} & a\gamma_0 & \gamma_1 & b^*\gamma_2 & d\gamma_1 & b\gamma_0+c^*\gamma_2 & d\gamma_1 & b\gamma_2 \\
 & \gamma_1 & a^*\gamma_0 & E_{sp} & a^*\gamma_0 & & b^*\gamma_2 & d\gamma_1 & b^*\gamma_0+c\gamma_2 & d\gamma_1 \\
 & & \gamma_1 & a\gamma_0 & E_{sp} & & & b^*\gamma_2 & d\gamma_1 & b\gamma_0+c^*\gamma_2 \\
b^*\gamma_0+c\gamma_2 & d\gamma_1 & b^*\gamma_2 & & & E_{sp} & a^*\gamma_0 & \gamma_1 & & \\
d\gamma_1 & b\gamma_0+c^*\gamma_2 & d\gamma_1 & b^*\gamma_2 & & a\gamma_0 & E_{sp} & a\gamma_0 & \gamma_1 & \\
b\gamma_2 & d\gamma_1 & b^*\gamma_0+c\gamma_2 & d\gamma_1 & b^*\gamma_2 & \gamma_1 & a^*\gamma_0 & E_{sp} & a^*\gamma_0 & \gamma_1 \\
 & b\gamma_2 & d\gamma_1 & b\gamma_0+c^*\gamma_2 & d\gamma_1 & & \gamma_1 & a\gamma_0 & E_{sp} & a\gamma_0 \\
 & & b\gamma_2 & d\gamma_1 & b^*\gamma_0+c\gamma_2 & & & \gamma_1 & a^*\gamma_0 & E_{sp}
\end{bmatrix}
\tag{2.36}
$$

Similarly the overlap matrix *S* can be written as

$$S=\begin{bmatrix}
1 & as_0 & s_1 & & & bs_0+c^*s_2 & ds_1 & bs_2 & & \\
a^*s_0 & 1 & a^*s_0 & s_1 & & ds_1 & b^*s_0+cs_2 & ds_1 & bs_2 & \\
s_1 & as_0 & 1 & as_0 & s_1 & b^*s_2 & ds_1 & bs_0+c^*s_2 & ds_1 & bs_2 \\
 & s_1 & a^*s_0 & 1 & a^*s_0 & & b^*s_2 & ds_1 & b^*s_0+cs_2 & ds_1 \\
 & & s_1 & as_0 & 1 & & & b^*s_2 & ds_1 & bs_0+c^*s_2 \\
b^*s_0+cs_2 & ds_1 & b^*s_2 & & & 1 & a^*s_0 & s_1 & & \\
ds_1 & bs_0+c^*s_2 & ds_1 & b^*s_2 & & as_0 & 1 & as_0 & s_1 & \\
bs_2 & ds_1 & b^*s_0+cs_2 & ds_1 & b^*s_2 & s_1 & a^*s_0 & 1 & a^*s_0 & s_1 \\
 & bs_2 & ds_1 & bs_0+c^*s_2 & ds_1 & & s_1 & as_0 & 1 & as_0 \\
 & & bs_2 & ds_1 & b^*s_0+cs_2 & & & s_1 & a^*s_0 & 1
\end{bmatrix} \tag{2.37}$$

The energy dispersion relationship is then obtained by solving the secular equation (2.11). By using the same Tight-binding parameters as in Table 2.1, the energy dispersion relations for armchair graphene nanoribbons with N_0=5,6,7 are calculated under first-nearest as well as third-nearest assumption. The results are summarized in Figure 2.4.

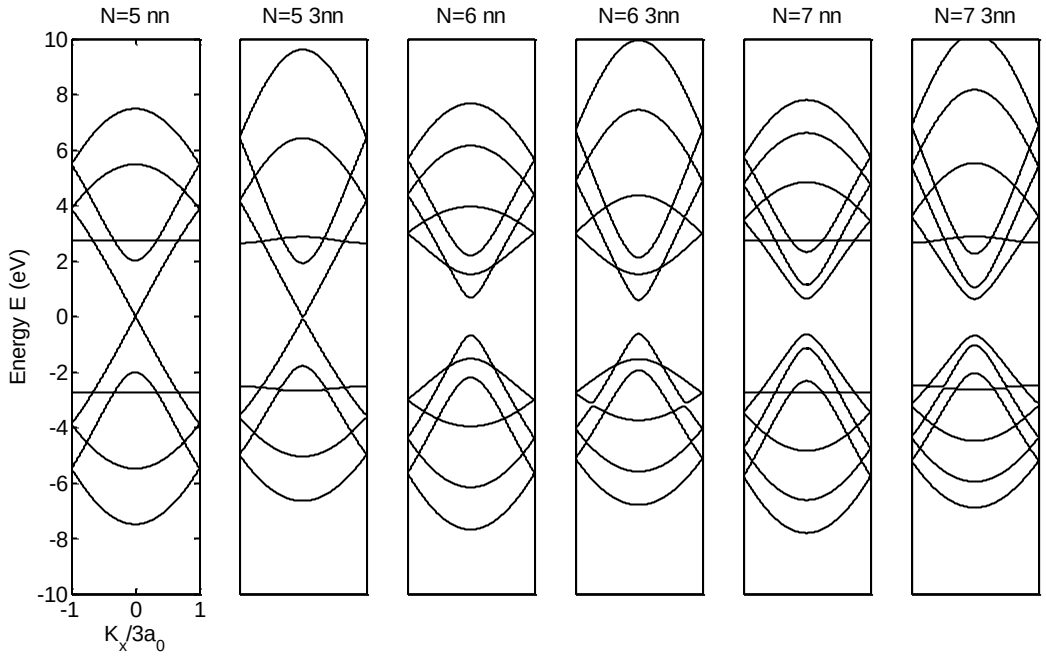

Figure 2.4 Energy dispersion relationship of armchair graphene nanoribbons with N_0=5,6,7 under nn (nearest-neighbour) and 3nn(3rd-nearest-neighbour) assumptions

2.3.2 Energy band gap of armchair graphene nanoribbons

It should be noted that around $k_x=0$ the conduction band and valance band shows a Dirac-like linear dispersion. This can be easily understood by projecting the graphene bandstructure onto the axis

corresponding to the armchair orientation [3]. Both numerical calculation and analytical results[23, 24] based on the first-nearest tight-binding assumption give the relationship of band gap δ as a function of the width of GNRs. The ribbon is metallic if $N_0=3m+2$ where m is an integer number and semiconducting in other cases. In particular we have

$$\begin{cases} \delta_{3m} = |\gamma_0|\left(4cos\frac{\pi m}{3m+1} - 2\right) \\ \delta_{3m+1} = |\gamma_0|\left(4cos\frac{\pi m}{3m+1} - 2\right) \\ \delta_{3m+2} = 0 \end{cases} \tag{2.38}$$

with $\delta_{3m} > \delta_{3m+1} > \delta_{3m+2}$. However our numerical result under the assumption of third-nearest interactions points out that even for $N_0 = 3m + 2$ the nanoribbon still opens a small band gap and this result is also confirmed by a number of first principle calculations[12, 25-28].

Figure 2.5 shows a graph of the band gaps in armchair GNRs as a function of width index ranging from $N_0=5$ to $N_0=34$ under both first-nearest and third-nearest assumptions. It should be noted that (a) third-nearest interaction opens a small bad gap when $N_0 = 3m + 2$; (b) When $N_0 = 3m + 1$ *or* $N_0 = 3m$ third-nearest interactions show a slightly decrease in the band gap and; (c) the band gap generally decreases as $1/N_0$ under both assumptions. This is similar to the case of zigzag carbon nanotubes in which the band gap decreases as *1/d*, where *d* is the diameter of the tube.

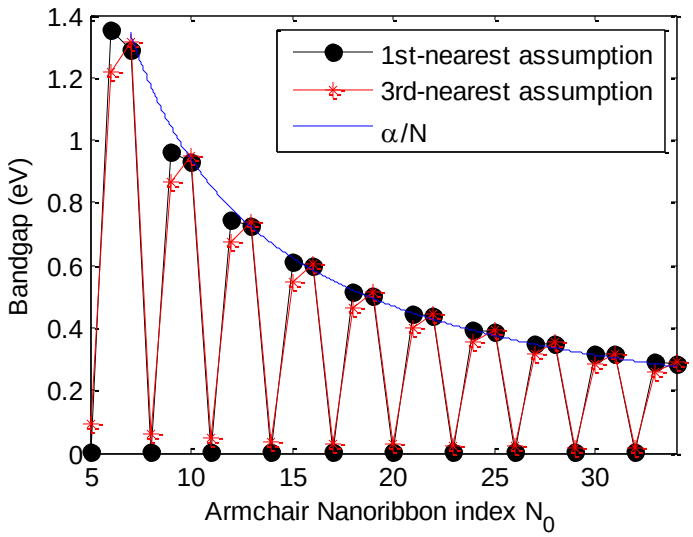

Figure 2.5 Energy band gap of armchair graphene nanoribbons as a function of their width index N_0 under first and third nearest neighbour tight-binding assumption.

Figure 2.6 compares first-nearest with third-nearest neighbour results and gives a clearer view of the increasing/decreasing bandgap.

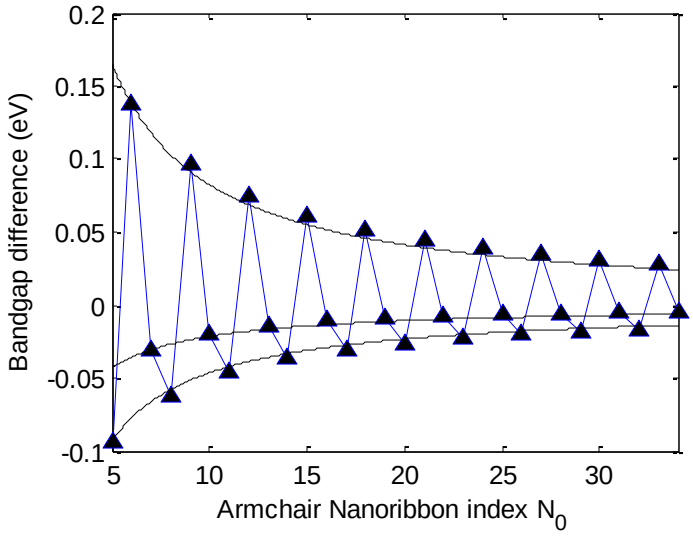

Figure 2.6 Energy band gap difference of first and third nearest neighbour tight-binding assumptions in the armchair graphene nanoribbon as a function of width index. The lines are also fitted to α/N_0 ,where α is a fitting parameter.

2.3.3 Zigzag nanoribbons

For the zigzag graphene nanoribbon with index N_0 shown in Figure 2.7, H and S can be obtained using the same method as we developed in 2.3.2. Here we show the derivation of the non-zero elements in the first row $H_{1,1}$,$H_{1,2}$, $H_{1,3}$ and $H_{1,4}$

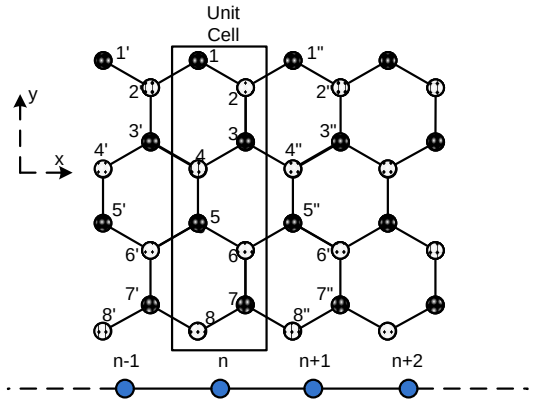

Figure 2.7 An N_0=4 zigzag graphene nanoribbon. By choosing the unit cell shown as the rectangular box, the nanoribbon can be treated as a 1D quantum wire.

$$
\begin{aligned}
H_{1,1} &= \frac{1}{N}\sum_{\vec{r}_1}\Big[\langle\varphi_1(\vec{r}-\vec{r}_1)|H_{op}|\varphi_1(\vec{r}-\vec{r}_1)\rangle \\
&\qquad + e^{i\vec{k}_x\cdot(\vec{r}_{1'}-\vec{r}_1)}\langle\varphi_1(\vec{r}-\vec{r}_1)|H_{op}|\varphi_1(\vec{r}-\vec{r}_{1'})\rangle \\
&\qquad + e^{i\vec{k}_x\cdot(\vec{r}_{1''}-\vec{r}_1)}\langle\varphi_1(\vec{r}-\vec{r}_1)|H_{op}|\varphi_1(\vec{r}-\vec{r}_{1''})\rangle\Big] \\
&= E_{sp} + e^{-ik_x\sqrt{3}a_0}\gamma_1 + e^{-ik_x\sqrt{3}a_0}\gamma_1 \\
&= E_{sp} + 2cos(k_x\sqrt{3}a_0)\gamma_1 = E_{sp} + p\gamma_1 \\
H_{1,2} &= \frac{1}{N}\sum_{\vec{r}_1}\Big[e^{i\vec{k}_x\cdot(\vec{r}_{2'}-\vec{r}_1)}\langle\varphi_1(\vec{r}-\vec{r}_1)|H_{op}|\varphi_1(\vec{r}-\vec{r}_{2'})\rangle \\
&\qquad + e^{i\vec{k}_x\cdot(\vec{r}_2-\vec{r}_1)}\langle\varphi_1(\vec{r}-\vec{r}_1)|H_{op}|\varphi_1(\vec{r}-\vec{r}_2)\rangle\Big] \\
&= E_{sp} + e^{-ik_x\frac{\sqrt{3}}{2}a_0}\gamma_0 + e^{-ik_x\frac{\sqrt{3}}{2}a_0}\gamma_0 \qquad (2.39) \\
&= 2cos(k_x\frac{\sqrt{3}}{2}a_0)\gamma_0 = q\gamma_0 \\
H_{1,3} &= \frac{1}{N}\sum_{\vec{r}_1}\Big[e^{i\vec{k}_x\cdot(\vec{r}_{3'}-\vec{r}_1)}\langle\varphi_1(\vec{r}-\vec{r}_1)|H_{op}|\varphi_1(\vec{r}-\vec{r}_{3'})\rangle \\
&\qquad + e^{i\vec{k}_x\cdot(\vec{r}_3-\vec{r}_1)}\langle\varphi_1(\vec{r}-\vec{r}_1)|H_{op}|\varphi_1(\vec{r}-\vec{r}_3)\rangle\Big] \\
&= e^{-ik_x\frac{\sqrt{3}}{2}a_0}\gamma_1 + e^{-ik_x\frac{\sqrt{3}}{2}a_0}\gamma_1 \\
&= 2cos(k_x\frac{\sqrt{3}}{2}a_0)\gamma_1 = q\gamma_1 \\
H_{1,4} &= \frac{1}{N}\sum_{\vec{r}_1} e^{i\vec{k}_x\cdot(\vec{r}_4-\vec{r}_1)}\langle\varphi_1(\vec{r}-\vec{r}_1)|H_{op}|\varphi_1(\vec{r}-\vec{r}_4)\rangle = \gamma_2
\end{aligned}
$$

The 8x8 matrices H and S are given below

$$
H = \begin{bmatrix}
E_{sp}+p\gamma_1 & q\gamma_0 & q\gamma_1 & \gamma_2 & & & & \\
q\gamma_0 & E_{sp}+p\gamma_1 & q\gamma_0 & q\gamma_1 & \gamma_2 & & & \\
q\gamma_1 & q\gamma_0 & E_{sp}+p\gamma_1 & q\gamma_0 & q\gamma_1 & \gamma_2 & & \\
\gamma_2 & q\gamma_1 & q\gamma_0 & E_{sp}+p\gamma_1 & q\gamma_0 & q\gamma_1 & \gamma_2 & \\
 & \gamma_2 & q\gamma_1 & q\gamma_0 & E_{sp}+p\gamma_1 & q\gamma_0 & q\gamma_1 & \gamma_2 \\
 & & \gamma_2 & q\gamma_1 & q\gamma_0 & E_{sp}+p\gamma_1 & q\gamma_0 & q\gamma_1 \\
 & & & \gamma_2 & q\gamma_1 & q\gamma_0 & E_{sp}+p\gamma_1 & q\gamma_0 \\
 & & & & \gamma_2 & q\gamma_1 & q\gamma_0 & E_{sp}+p\gamma_1
\end{bmatrix} \qquad (2.40)
$$

$$S=\begin{bmatrix} 1+ps_1 & qs_0 & qs_1 & s_2 & & & & \\ qs_0 & 1+ps_1 & qs_0 & qs_1 & s_2 & & & \\ qs_1 & qs_0 & 1+ps_1 & qs_0 & qs_1 & s_2 & & \\ s_2 & qs_1 & qs_0 & 1+ps_1 & qs_0 & qs_1 & s_2 & \\ & s_2 & qs_1 & qs_0 & 1+ps_1 & qs_0 & qs_1 & s_2 \\ & & s_2 & qs_1 & qs_0 & 1+ps_1 & qs_0 & qs_1 \\ & & & s_2 & qs_1 & qs_0 & 1+ps_1 & qs_0 \\ & & & & s_2 & qs_1 & qs_0 & 1+ps_1 \end{bmatrix} \quad (2.41)$$

Substituting (2.40) and (2.41) into secular equation (2.11) and using the parameters in Table 2.1 the energy band can be found numerically. As an example the energy dispersion relationship of a zigzag graphene nanoribbon with N_0=20 is shown in Figure 2.6.

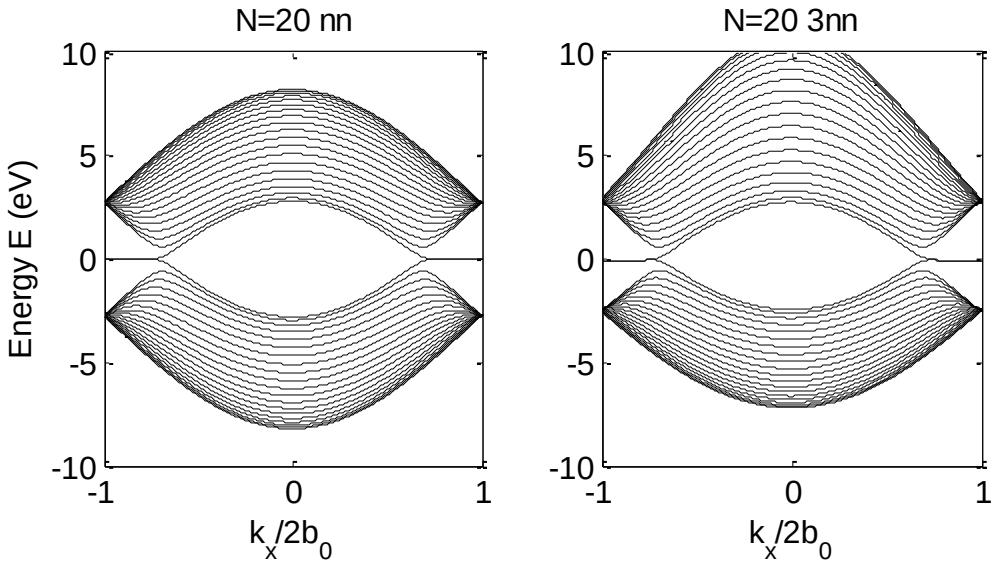

Figure 2.8 Energy dispersion relationship of an armchair graphene nanoribbon with N_0=20 under nn (nearest-neighbour) and 3nn(3rd-nearest-neighbour) assumptions

The energy bands present some typical features: (a) the Dirac points of the 2D graphene are mapped into $k_x = \pm 2\pi/(3a_0)$, (b) there are two partially flat degenerate bands with zero energy between the Dirac points and the border of the Brillouin zone; the corresponding states are mainly located at the edges.

2.3.4 Quasi one-dimensional model

The integral matrix *H* and overlap matrix *S* used in the previous calculation are functions of the Bloch wave vector k_x. As a result, H and S need to be rebuilt for each solution of the secular equation which takes a lot of computational time for a graphene nanoribbon with a large index number. However if we treat the nanoribbon as a quasi-one dimensional structure as shown in figure 2.5 and 2.7, *H* and *S* only contain constant matrix elements.

We start by writing the time-independent Schrodinger equation in block matrix form.

$$E\begin{bmatrix} S_{0,0} & S_{0,1} & & & & \\ & \ddots & & & & \\ & S_{n,n-1} & S_{n,n} & S_{n,n+1} & & \\ & & & \ddots & & \\ & & & S_{N,N-1} & S_{N,N} \end{bmatrix}\begin{Vmatrix} \varphi_0 \\ \vdots \\ \varphi_n \\ \vdots \\ \varphi_N \end{Vmatrix} = \begin{bmatrix} H_{0,0} & H_{0,1} & & & & \\ & \ddots & & & & \\ & H_{n,n-1} & H_{n,n} & H_{n,n+1} & & \\ & & & \ddots & & \\ & & & H_{N,N-1} & H_{N,N} \end{bmatrix}\begin{Vmatrix} \varphi_0 \\ \vdots \\ \varphi_n \\ \vdots \\ \varphi_N \end{Vmatrix} \quad (2.42)$$

Where ϕ_n is the $2N_0$-dimensional vector representing the wave function at the n_{th} unit cell. Taking the n_{th} row of (2.42) we have

$$H_{n,n-1}\phi_{n-1} + H_{n,n}\phi_n + H_{n,n+1}\phi_{n+1} - E(S_{n,n-1}\phi_{n-1} + S_{n,n}\phi_n + S_{n,n+1}\phi_{n+1}) = 0 \quad (2.43)$$

The Hamiltonians $H_{n,n-1}$, $H_{n,n}$,$H_{n,n+1}$ and overlap matrices, $S_{n,n-1}$, $S_{n,n}$, $S_{n,n+1}$ are all $2N_0$x$2N_0$ constant matrices. Due to the periodicity of the structure we can also obtain: $H_{n,n} = H_a$, $H_{n,n-1} = H_b$, $H_{n+1,n} = H_c$, $S_{n,n} = S_a$, $S_{n,n-1} = S_b$,$S_{n+1,n} = S_c$.

Because of the property of the Bloch function we have $\phi_n \sim e^{ikn}$ ($k = k_x$/d) where d is the distance between two neighbouring unit cells. For armchair GNRs, $d = 3a_0$, and in the case of zigzag GNRs, $d = \sqrt{3}a_0$. Substituting ϕ_n into (2.43) we have

$$det\,[H_b e^{-ik} + H_a + H_c e^{ik} - E(S_b e^{-ik} + S_a + S_c e^{ik})] = 0 \quad (2.44)$$

(2.44) gives $2N_0$ solutions for E(k) corresponding to N_0 subbands of the dispersion relation. In the case of first nearest approximation without orbital overlap, S_b , S_c are empty matrices and S_a becomes an identity matrix.

$$det\,[H_b e^{-ik} + H_a + H_c e^{ik} - EI] = 0 \quad (2.45)$$

As an example, H_a, H_b, H_c of the N_0=5 armchair shown in Figure 2.3 are given by

$$H_a = \begin{bmatrix} E_{sp} & \gamma_0 & \gamma_1 & & & \gamma_0 & \gamma_1 & \gamma_2 & & \\ \gamma_0 & E_{sp} & \gamma_0 & \gamma_1 & & \gamma_1 & \gamma_2 & \gamma_1 & & \\ \gamma_1 & \gamma_0 & E_{sp} & \gamma_0 & \gamma_1 & \gamma_2 & \gamma_1 & \gamma_0 & \gamma_1 & \gamma_2 \\ & \gamma_1 & \gamma_0 & E_{sp} & \gamma_0 & & & \gamma_1 & \gamma_2 & \gamma_1 \\ & & \gamma_1 & \gamma_0 & E_{sp} & & & \gamma_2 & \gamma_1 & \gamma_0 \\ \gamma_0 & \gamma_1 & \gamma_2 & & & E_{sp} & \gamma_0 & \gamma_1 & & \\ \gamma_1 & \gamma_2 & \gamma_1 & & & \gamma_0 & E_{sp} & \gamma_0 & \gamma_1 & \\ \gamma_2 & \gamma_1 & \gamma_0 & \gamma_1 & \gamma_2 & \gamma_1 & \gamma_0 & E_{sp} & \gamma_0 & \gamma_1 \\ & & \gamma_1 & \gamma_2 & \gamma_1 & & \gamma_1 & \gamma_0 & E_{sp} & \gamma_0 \\ & & \gamma_2 & \gamma_1 & \gamma_0 & & & \gamma_1 & \gamma_0 & E_{sp} \end{bmatrix} \tag{2.46}$$

$$H_b = H_c^* = \begin{bmatrix} & & & & & & & & & \\ & & & & & & & & & \\ & & & & & & & & & \\ & & & & & & & & & \\ & & & & & & & & & \\ & & & & & & & & & \\ \gamma_2 & \gamma_1 & & & & & & & & \\ \gamma_1 & \gamma_0 & \gamma_1 & \gamma_2 & & & & & & \\ & \gamma_1 & \gamma_2 & \gamma_1 & & & & & & \\ & \gamma_2 & \gamma_1 & \gamma_0 & \gamma_1 & & & & & \\ & & & \gamma_1 & \gamma_2 & & & & & \end{bmatrix} \tag{2.47}$$

Using this model the energy dispersion relationship of armchair graphene nanoribbons with N_0=5 is obtained and shown in Figure 2.9. The result agree extremely well with those in Figure 2.4 within a round off error less than 10^{-14}.

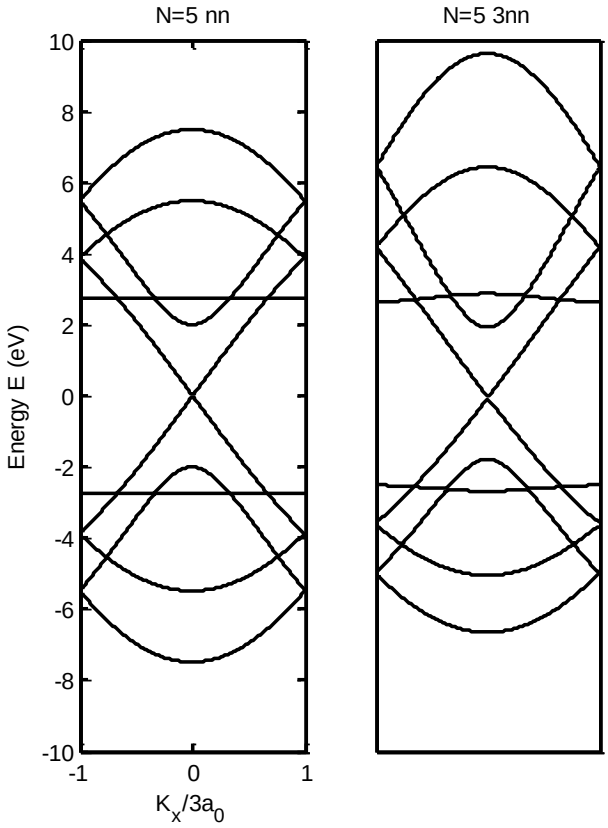

Figure 2.9 Energy dispersion relationship of armchair graphene nanoribbons with N_0=5 obtained by the quasi-one dimensional model

2.4 Edge distortion in armchair graphene nanoribbons

In the previous calculation of the band structure of an armchair graphene nanoribbon we use the same tight-binding parameters at the edge of the nanoribbon as in the centre. However, this assumption has been shown to be inaccurate in most cases by a number of first-principle calculations [11, 25-28]. In the paper by White et al. [17] an edge distortion parameter $\Delta\gamma_0 = -0.2eV$ is introduced in to the tight-binding model. By simply adding the distortion parameter to the first-nearest neighbour hopping parameter at the armchair nanoribbon edges (shown by the red lines in figure 2.3) the Hamiltonian H_a in (2.46) can be rewritten as

$$H_a = \begin{bmatrix}
E_{sp} & \gamma_0 & \gamma_1 & & & \gamma_0+\Delta\gamma_0 & \gamma_1 & \gamma_2 & & \\
\gamma_0 & E_{sp} & \gamma_0 & \gamma_1 & & \gamma_1 & \gamma_2 & \gamma_1 & & \\
\gamma_1 & \gamma_0 & E_{sp} & \gamma_0 & \gamma_1 & \gamma_2 & \gamma_1 & \gamma_0 & \gamma_1 & \gamma_2 \\
 & \gamma_1 & \gamma_0 & E_{sp} & \gamma_0 & & & \gamma_1 & \gamma_2 & \gamma_1 \\
 & & \gamma_1 & \gamma_0 & E_{sp} & & & \gamma_2 & \gamma_1 & \gamma_0+\Delta\gamma_0 \\
\gamma_0+\Delta\gamma_0 & \gamma_1 & \gamma_2 & & & E_{sp} & \gamma_0 & \gamma_1 & & \\
\gamma_1 & \gamma_2 & \gamma_1 & & & \gamma_0 & E_{sp} & \gamma_0 & \gamma_1 & \\
\gamma_2 & \gamma_1 & \gamma_0 & \gamma_1 & \gamma_2 & \gamma_1 & \gamma_0 & E_{sp} & \gamma_0 & \gamma_1 \\
 & & \gamma_1 & \gamma_2 & \gamma_1 & & \gamma_1 & \gamma_0 & E_{sp} & \gamma_0 \\
 & & \gamma_2 & \gamma_1 & \gamma_0+\Delta\gamma_0 & & & \gamma_1 & \gamma_0 & E_{sp}
\end{bmatrix} \quad (2.48)$$

Figure 2.10 compares the bandstructure result obtained using the edge distortion model with the one obtained from a normal third-nearest neighbour tight-binding model. It can be clearly seen that with edge distortion a larger bandgap opens in the armchair nanoribbon.

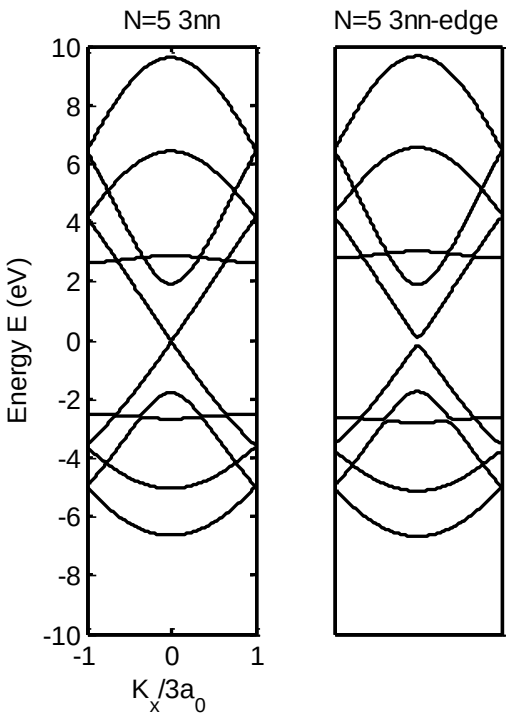

2.10 Energy bandstructure of an $N_0=5$ armchair nanoribbon obtained by the normal third-nearest tight-binding approximation (left) and third-nearest tight-binding approximation with an additional edge distortion parameter.

2.5 Bandstructure of strained graphene nanoribbons

Strain could have a significant effect on the electronic properties of a material and is used in the silicon electronics industry to boost device performance. The mobility of Si, SiGe and Ge has been successfully improved by the effects of strain[29]. For carbon nanotubes both experiments and simulations have confirmed that the band structure can be dramatically altered by strain[30]. Because of the close relation between graphene and carbon nanotubes, researchers have naturally explored the effects of strain in graphene.

As discussed previously, graphene, being an atomically thin 2-dimensional material does not have a bandgap. A bandgap might be introduced by patterning the 2-D graphene into nanoribbons. Density functional theory (DFT) calculations show that strain can be a useful way to further tailor the bandstructure of graphene nanoribbons [31]. In this section we study the effects of uniaxial strain in graphene using the tight-binding model described in [32]. The tight-binding Hamiltonian obtained and the band structure will be used to study the other electronic properties of graphene nanoribbons in Chapter 4.

Consider the graphene nanoribbon shown in figure 2.11.

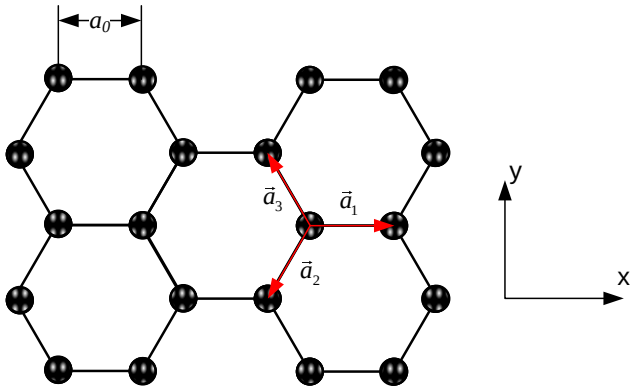

2.11 Graphene nanoribbon built up from bond vectors $\vec{a}_1\ \vec{a}_2\ \vec{a}_3$

The unstrained bond vectors are given by

$$\vec{a}_1 = a_0\vec{x}$$
$$\vec{a}_2 = -\frac{1}{2}a_0\vec{x} - \frac{\sqrt{3}}{2}a_0\vec{y} \qquad (2.49)$$
$$\vec{a}_3 = -\frac{1}{2}a_0\vec{x} + \frac{\sqrt{3}}{2}a_0\vec{y}$$

If we set $\vec{x}$ to be the transport direction then the application of a uniaxial strain causes the following change of the bond vectors,

$$\vec{a}_{ix} \to (1+\sigma)\vec{a}_{ix}$$
$$\vec{a}_{iy} \to (1+v\sigma)\vec{a}_{iy} \qquad (2.50)$$

where *i=1,2,3* and $\vec{a}_{ix}$, $\vec{a}_{iy}$ are the x and y component of $\vec{a}_i$ respectively. σ is defined as the uniaxial strain along x direction where $v \approx 0.165$ is the Poisson ratio[32]. We use the same tight-binding Hamiltonian parameters as in 2.4, which includes the effects of edge bond relaxation and the third nearest neighbor coupling. When the nanoribbon is under uniaxial strain, each tight-binding parameter is scaled by a dimensionless factor $\xi = \left(\frac{a_0}{a}\right)^2$, where a_0 is the unstrained bond length shown in Figure 2.11.

Using this simple tight-binding model, the bandstructure of the graphene nanoribbons under different strain strength can be calculated. As an example, the first two subbands of a $N_0=13$ armchair graphene nanoribbon without and with 0.03 uniaxial strain are plotted in Figure 2.12. The calculation shows that this specific strain length (0.03) will decrease the bandgap of the first subband but increase the bandgap of the second subband.

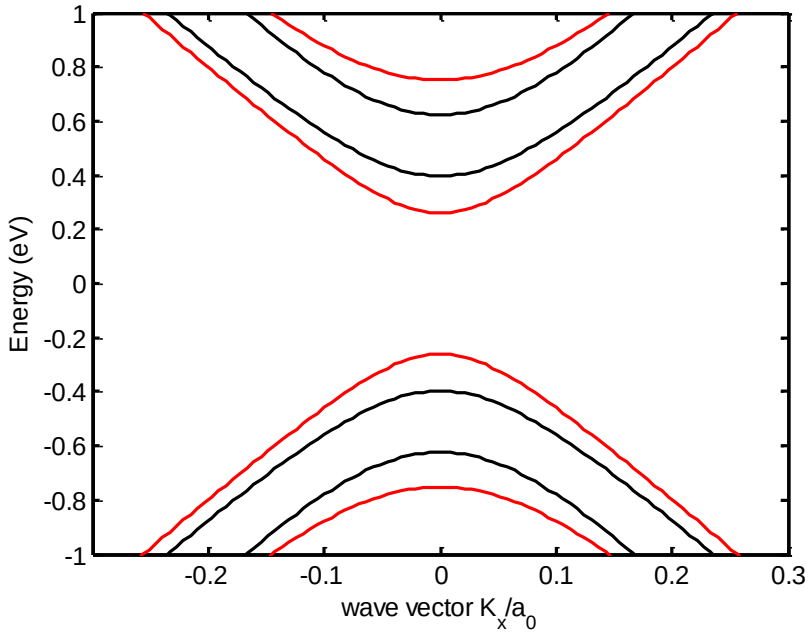

2.12 Energy dispersion relation of the first two subbands of an $N_0=13$ armchair graphene nanoribbon. Black lines correspond to an unstrained nanoribbon, red lines correspond to a nanoribbon under $\sigma = 0.03$ uniaxial strain.

2.6 Effective mass of armchair graphene nanoribbons

In the field of semiconductor simulation the effective mass is often introduced to describe the movement of electrons obeying Newton's law. For a simple parabolic E-k relationship, the effetive mass m^* of the electrons in a certain conduction band E can be found by fitting the following equation.

$$E - (E_i + \frac{E_g^b}{2}) = \frac{\hbar^2 k^2}{2m_b^*} \tag{2.51}$$

where $E_g^b = E_c^b - E_v^b$ is the bandgap of the subband, b, and E_i is the instrinsic energy level. Usually E_i is set to be zero.

However in the case of graphene, the parabolic relationship only exsists at low energies in armchair graphene nanoribbons with the index number $N_0 \neq 3m+2$ (otherwise we have a linear dispersion relationship). As a result the following nonparabolic fitting equation is introduced [33].

$$\left(E - \frac{E_g^b}{2}\right)\left(\frac{1}{2} + \frac{E}{E_g^b}\right) = \frac{\hbar^2 k^2}{2m_b^*} \tag{2.52}$$

Figure 2.13 shows the lowest two subbands of a N_0=13 armchair graphene nanoribbon. Both parabolic and nonparabolic models are plotted on the same graph. The parabolic model only fits the results from the tight-binding model in the low energy range (in the example $-0.15 < \frac{k_x}{3a_0} < 0.15$) while the nonparabolic model gives excellent agreement with the tight-binding model over a extended energy range.

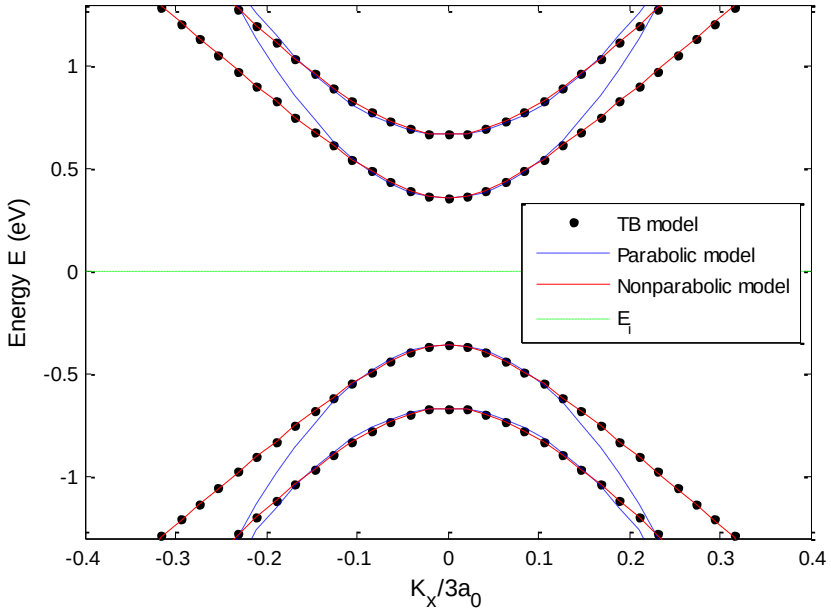

2.13 Energy dispersion relations for the two lowest conduction/valence pairs of subbands of an N_0=13 GNR calculated using the Tight-binding (TB) model and Nonparabolic and parabolic models

Figure 2.14 compares the two models in an N_0=14 armchair nanoribbon where the tight-binding model shows a liner dispersion relationship in the lowest subband.

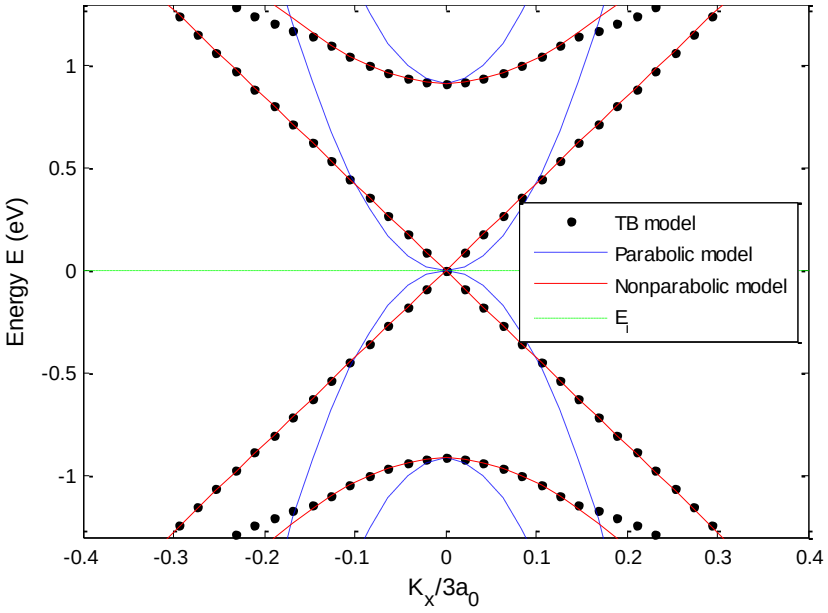

2.14 Energy dispersion relations for the two lowest conduction/valence pairs of subbands of an N_0=14 GNR calculated using the Tight-binding (TB) model and the Nonparabolic and parabolic models

In chapter 3 nonparabolic and parabolic fitting parameters are used to obtain an effective mass for use in a Poisson-Schrödinger solver applied to a graphene field effect transistor.

2.7 Conclusions

In this chapter the energy band structures of graphene and graphene nanoribbons are obtained using the tight binding model. Initially, only first nearest-neighbour interactions are considered but it is found that third nearest-neighbour interactions must be taken into account to achieve an accurate bandstructure. The method is used to determine the bandstructure and energy bandgap in armchair and zigzag graphene nanoribbons. In order to improve computational efficiency a quasi-one dimensional model of graphene nanoribbons is developed to obtain the energy bandstructures with no loss of accuracy. The effect of edge distortion and strain on the energy bandstructures of graphene nanoribbons are also considered. Finally, parabolic and non-parabolic expressions are used to fit to the energy bandstructures to obtain an effective mass for use in a Poisson-Schrödinger solver developed in chapter 3 to simulate charge transport in a graphene field effect transistor.

Chapter 3 Simulation of charge transport in a graphene nanoribbon transistor using a Schrödinger-Poisson solver in the effective mass approximation

3.1 Introduction

In this chapter we model a graphene based field effect transistor as shown in Figure 3.1. This device consists of a semiconducting graphene nanoribbon with a wrap around gate at four faces of the cuboid geometry. An insulator with relative permittivity ε_{ox}=11.7 separates the semiconductor region of the device from the surrounding gate contact. The ends of the device are terminated by the metal source and drain contacts. Device parameters include the length=20nm (along x-direction) of the nanoribbon, its width=4nm (along z-direction) and the thickness of the insulator t_{ox} =2.5nm separating the graphene from the gate contact.

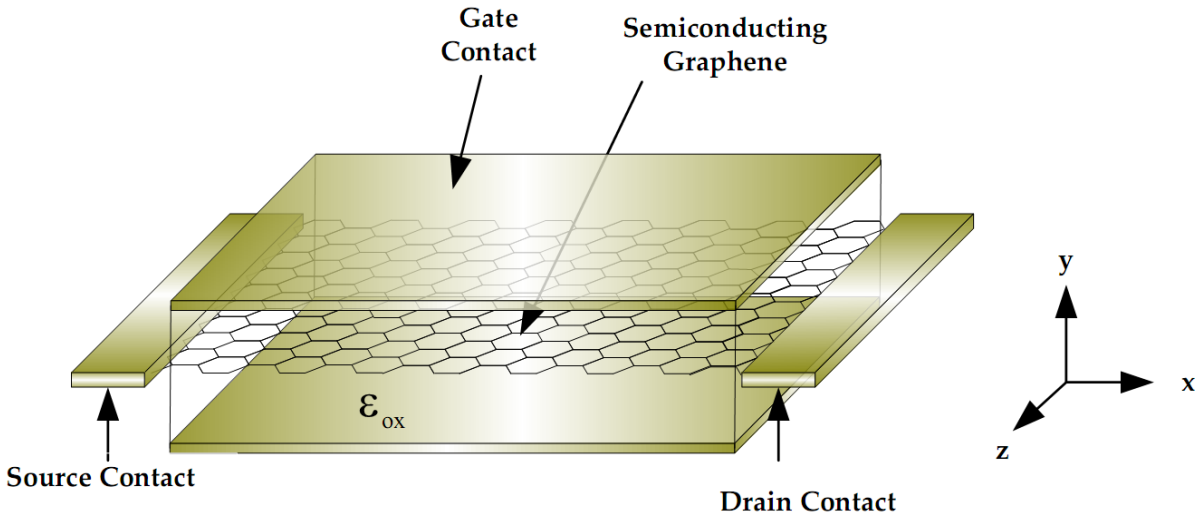

Figure 3.1 Cubical geometry of Graphene FET

The graphene used as the channel material in the model device is an armchair nanoribbon with the width of the graphene sheet defined by N_0=19. The bandstructure is obtained using the tight-binding Hamiltonian of the armchair nanoribbon that includes the first nearest neighbour (1NN), third nearest neighbour (3NN) and the 1NN edge distortion Hamiltonians. Details of the bandstructure calculation were given in chapter 2.

In the simulation, the charge transport in graphene is investigated through the self-consistent solution of the charge and local electrostatic potential. The quantum mechanical treatment of electron transport is included by solving a 1D Schrödinger's equation where the evanescent wavefunction from the metallic graphene to the semiconducting region is considered. Although this procedure has already been used in the simulation of a silicon quantum wire [34] and carbon nanotube field effect transistor [4], here it is applied to a graphene nanoribbon transistor with improvements to the Poisson-Schrodinger solver for 3-D structures.

The potential profile in the entire model is obtained from the solution to a three-dimensional Poisson equation for a cuboid system given by:

$$\left(\frac{\partial^2}{\partial x^2}+\frac{\partial^2}{\partial y^2}+\frac{\partial^2}{\partial z^2}\right)V(x,y,z)=-\frac{\rho(x,y,z)}{\varepsilon} \tag{3.1}$$

Here $V(x,y,z)$ and $\rho(x,y,z)$ are, respectively, the potential and charge density in the device at position (x,y,z).

The nanoribbon is divided into unit cells which allow us to treat the graphene as a quasi-one-dimensional conductor and the charge distribution on the surface of the material is obtained by solving the time-independent Schrödinger equation given by:

$$\frac{\partial^2\psi}{\partial z^2}=-\frac{2m_*}{\hbar^2}(E-U)\psi=-k^2\psi \tag{3.2}$$

Here $\psi(E,x)$ is the wavefunction of the charge carrier having an Energy E, m^* the effective mass obtained from the bandstructure of the nanoribbon and U is the local effective potential seen by the carrier:

$$U=qV_{graphene}(x,z)-X_{cn} \tag{3.3}$$

Here X_{cn} is the electron affinity of graphene, $V_{graphene}(x,z)$ is the potential on the graphene sheet at position (x,z). Iteration starts by guessing the initial charge density on every point of the grid inside the device (usually zero). Next, by solving the Poisson equation we can know the electron potential of every point inside the device. Using the scattering matrix method we can then get obtain a new charge density distribution in the device from the Schrodinger equation. Using this new charge density to solve the Poisson equation again and repeating these steps many times until a new value of the charge density

matches the older one, we can get a final solution of the charge density by iteration. Hence, transmission probability, current and other characteristics of the device can be found. A flow chart of this method is shown below.

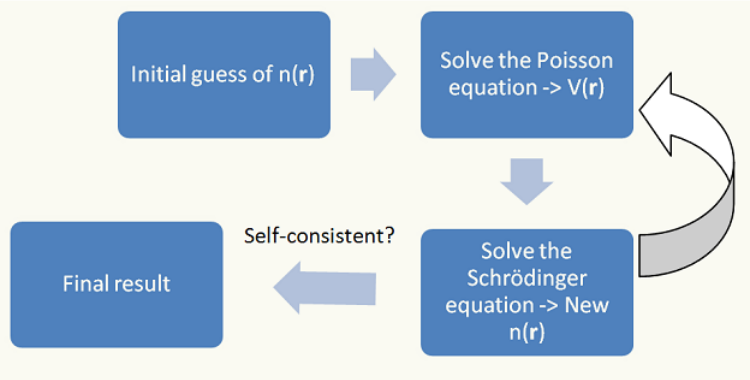

Figure 3.2 Flow Chart showing the self-consistent solution of the Poisson-Schrödinger problem

3.2 Solution of Poisson's Equation

In the field of device simulation Poisson's equation is often used to describe the potential in the device region. In this section Poisson's equation is solved using the finite difference method.

3.2.1 Finite difference method

Given a function *f(x)* shown in the figure below, one can approximate its derivative, slope of the tangent at *P,* by the slope of arc PB, giving the forward-difference formula,

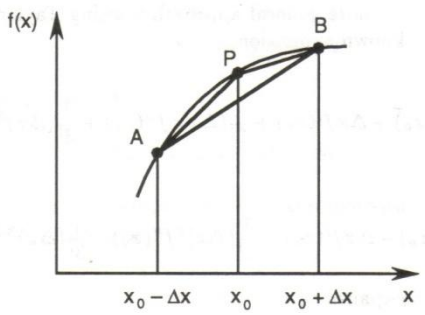

Figure 3.3 Estimates for the derivative of f(x) at P using forward, backward, and central differences

$$f'(x_0) \approx \frac{f(x_0 + \Delta x) - f(x_0)}{\Delta x} \tag{3.4}$$

or the slope of the arc AP, yielding the backward-difference formula as;

$$f'(x_0) \approx \frac{f(x_0) - f(x_0 - \Delta x)}{\Delta x} \tag{3.5}$$

or the slope of the arc AB, resulting in the central-difference formula;

$$f'(x_0) \approx \frac{f(x_0 + \Delta x) - f(x_0 - \Delta x)}{2\Delta x} \tag{3.6}$$

Also, the second derivative of $f(x)$ at *P* can be estimated as;

$$f''(x_0) \approx \frac{f(x_0 + \Delta x) - 2f(x_0) + f(x_0 - \Delta x)}{(\Delta x)^2} \tag{3.7}$$

(3.4),(3.5) and (3.6) are named as forward, backward and central difference respectively. In general, any approximation of a derivative in terms of values at a discrete set of points is called finite difference approximation.

3.2.2 3-D discretization

From the Poisson equation (1) Let $\mathrm{V_{ijk}}$ represent an approximation to $\mathrm{V(x, y, z)}$. In order to discretize (3.1) we replace both the x and y derivatives with centered finite differences which gives:

$$\begin{aligned} &\frac{1}{(\Delta x)^2}\left(V_{i-1,j,k} - 2V_{i,j,k} + V_{i+1,j,k}\right) + \frac{1}{(\Delta y)^2}\left(V_{i,j-1,k} - 2V_{i,j,k} + V_{i,j+1,k}\right) \\ &\qquad + \frac{1}{(\Delta z)^2}\left(V_{i,j,k-1} - 2V_{i,j,k} + V_{i,j,k-1}\right) = -\frac{\rho_{i,j,k}}{\varepsilon} \end{aligned} \tag{3.8}$$

Consider special case where $\Delta x = \Delta y = \Delta z \equiv h$ we can rewrite (2) as

$$\frac{1}{h^2}\left(V_{i-1,j,k} + V_{i+1,j,k} + V_{i,j-1,k} + V_{i,j+1,k} + V_{i,j-1,k} + V_{i,j+1,k} - 6V_{i,j,k}\right) = -\frac{\rho_{i,j,k}}{\varepsilon} \tag{3.9}$$

Dividing the 3-D box into $l \times m \times n$ grids and numbering each grid by an index α, where

$$\alpha = i + (j-1)\cdot l + (k-1)\cdot l \cdot m \tag{3.10}$$

3.10 is transformed into

$$V_{\alpha-l\cdot m} + V_{\alpha-l} + V_{\alpha-1} - 6V_\alpha + V_{\alpha+1} + V_{\alpha+l} + V_{\alpha+l\cdot m} = -\frac{\rho_\alpha h^2}{\varepsilon} \tag{3.11}$$

In matrix form this equation can be written as

$$\boldsymbol{AV} = -\frac{h^2}{\varepsilon}\boldsymbol{\rho} \tag{3.12}$$

Where, $\boldsymbol{V} = [V_1\ V_2\ \cdots\ V_\alpha\ \cdots\ V_{l\times m\times n}]^{\mathrm{T}}$, $\boldsymbol{\rho} = [\rho_1\ \rho_2\ \cdots\ \rho_\alpha\ \cdots\ \rho_{l\times m\times n}]^{\mathrm{T}}$ and $\boldsymbol{A}$ is an $(\mathrm{l}\times\mathrm{m}\times\mathrm{n})^2$ sparse matrix with $[1\cdots 1\cdots 1-6\ \ 1\cdots 1\cdots 1]$ on its diagonal as shown in Figure 3.4.

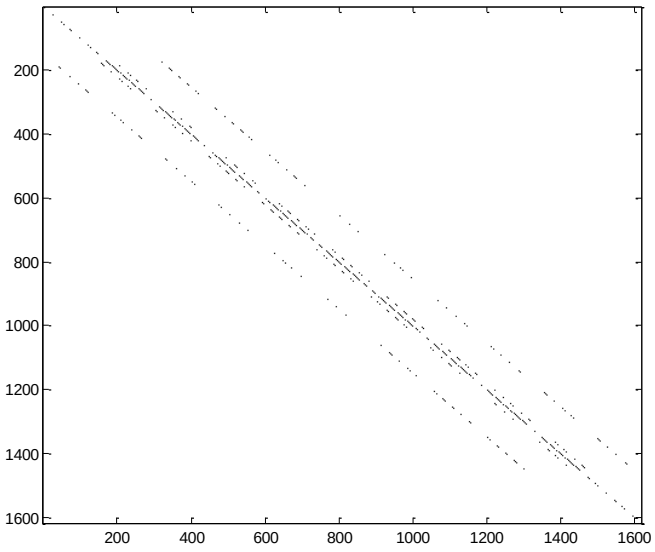

Figure 3.4 A sparse matrix obtained when solving 3-D Poisson equation. The non-zero elements are shown in black.

Once the vector $\boldsymbol{\rho}$ containing charge density on every grid point is given, we can calculate the potential by simply inversing the A matrix.

$$\boldsymbol{V} = -\boldsymbol{A}^{-1}\frac{h^2}{\varepsilon}\boldsymbol{\rho} \tag{3.13}$$

3.2.3 Boundary conditions

Equation (3.11) is the general form for all the grids inside the cuboid. Assume the grid with index j is on the boundary, when the calculation comes to the jth row of matrix ***A***, (3.11) is no longer useful because it requires knowledge the potential outside the box. To avoid this, we need to modify the matrix ***A*** and also the jth element of $\boldsymbol{\rho}$.

An easy implementation is setting $-\frac{h^2}{\varepsilon}\rho_j$ to be the value of the potential of grid index j which is defined by the source, drain and gate voltage of the graphene transistor.

$$\begin{aligned} V_s &= -\frac{\phi}{q} \\ V_g &= V_s + V_{gs} \\ V_d &= V_s + V_{ds} \end{aligned} \tag{3.14}$$

where Ø is the work function. As a result, the j_{th} row of modified ***A*** matrix will become $[0 \cdots 1 \cdots 0]$ and ρ_j is now related to the voltage by the constant $-\frac{h^2}{\varepsilon}$.

3.3 Solution of the Schrodinger equation

The charge distribution on the graphene surface is obtained by solving the Schrödinger equation using the scattering matrix method thereby providing a numerical solution at a given energy, E. Although the graphene sheet is two-dimensional, in order to use the one-dimensional energy dispersion relation and effective mass (same for electrons and holes due to symmetry), we treat it as a one-dimensional system. The charge density in the model device is given by:

$$Q(x) = \frac{-q(n(x) - p(x))}{\Delta^3}\Delta \tag{1}$$

where q is the electron charge, Δ is the length of a single interval on the grid, and n(x) and p(x) are the number of electrons and holes in the graphene as a function of position.

3.3.1 Scattering matrix method

The scattering matrix theory is derived in terms of carrier fluxes and their backscattering probabilities [35]. Consider a semiconductor slab with a finite thickness Δz, as shown in Fig 3.5. Assuming steady state conditions, $a(z)$ and $b(z)$ are the position-dependent, steady state, right- and left-directed fluxes. There is a right-directed flux incident on the left face of the slab and a left-directed flux incident on the right face.

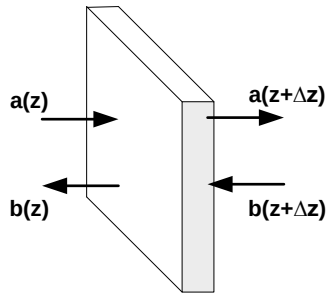

Figure 3.5 Fluxes of charge carriers incident upon and reflected from a slab of finite thickness.

In this example, fluxes $b(z)$ and $a(z+\Delta z)$ that emerge from the slab are to be determined. These fluxes can be expressed in scattering matrix form, which relates both fluxes emerging from the slab to the two incident fluxes on the slab:

$$\begin{pmatrix} a(z+\Delta z) \\ b(z) \end{pmatrix} = \begin{bmatrix} T & 1-T' \\ 1-T & T' \end{bmatrix} \begin{pmatrix} a(z) \\ b(z+\Delta z) \end{pmatrix} \tag{3.15}$$

where T and T' denote the fraction of the steady-state right- and left-directed fluxes transmitted across the slab.

The device under consideration can be divided into a set of thin slabs connected so that the output fluxes from one slab provide the input fluxes to its neighbouring slabs. The two fluxes injected from the left and right contacts are used as the boundary conditions. Fig. 3.6 shows two interconnected scattering matrices.

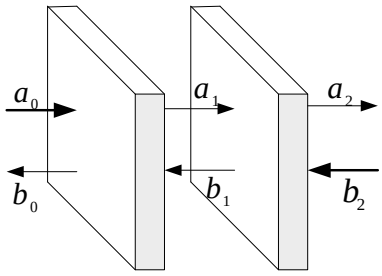

Figure 3.6 Two scattering matrices cascaded to produce a single, composite scattering matrix.

Taking only the fluxes emerging from the set of two scattering matrices, a_2 and b_0 into account, the two scattering matrices can be replaced by a single scattering matrix. Assuming that the two scattering matrices have transmission elements t_1, t_1', t_2 and t_2' then the elements of the composite scattering matrix are:

$$\begin{aligned} t_{21} &= t_1[1 - r_2' r_2]^{-1} t_2 \\ r_{21} &= r_1 + t_1' r_2 [1 - r_1' r_2]^{-1} t_1 \\ r_{21}' &= r_2' + t_2 [1 - r_1' r_2]^{-1} r_1' t_2' \\ t_{21}' &= t_1' [1 - r_1' r_2]^{-1} t_2' \end{aligned} \tag{3.16}$$

where $r_1 = 1 - t_1$, etc. Eq. 3.16 describes the multiple reflection processes that occur when a flux entering from the left or right, transmits across the first slab then backscatters and reflects from the interiors of the two slabs.

In real applications, the device is divided into a finite number of scattering matrices. These matrices are then cascaded two at a time until the entire device is described by a single scattering matrix. Once this matrix is computed, the current through the device is determined by subtracting the right- and left-directed fluxes. In the next section, this modelling technique is applied to a MOS device based on graphene.

3.3.2 Discretisation of the quantum mechanical problem

The entire system is divided into N grids and for each grid the electron wavefunction Ψ is expressed as:

$$\psi_n = A_n e^{ik_n z} + B_n e^{-ik_n z} \tag{3.17}$$

where k is the wavevector, A and B are the amplitudes of the wavefunctions. The wavefunction and its derivative are matched on the boundary between intervals n and $n+1$ using the relations:

$$\begin{aligned} \psi_n &= \psi_{n+1} \\ \frac{\partial \psi_n}{\partial z} &= \frac{\partial \psi_{n+1}}{\partial z} \end{aligned} \tag{3.18}$$

The relationship between $[A_n\ B_n]^{\mathrm{T}}$ and $[A_{n+1}\ B_{n+1}]^T$ is obtained using:

$$\begin{bmatrix} A_n \\ B_n \end{bmatrix} = S_n \begin{bmatrix} A_{n+1} \\ B_{n+1} \end{bmatrix} \tag{3.19}$$

where $[A_n\ B_n]^{\mathrm{T}}$ is the transpose of the matrix $[A_n\ B_n]$, S_n is the scattering coefficient, and Ψ_1 and Ψ_N are the wavefunctions in the source and drain contacts, respectively. When computing the wavefunctions for the source injection, the amplitude of the wavefunction at the drain end is set to zero. An analogous calculation is performed when considering the drain injection.

The Landauer equation is expected to hold for the flux and the probability current I_P equated to the Landauer current I_L [4]:

$$\begin{aligned} I_P(E) &= \frac{q\hbar}{2m} i \left[\left(\frac{\partial \Psi}{\partial z} \right)^* \Psi - \Psi^* \left(\frac{\partial \Psi}{\partial z} \right) \right] \\ I_L(E) &= \frac{q}{\pi\hbar} f_s(E) T(E) \\ \frac{2q}{\pi\hbar} f_s T &= \frac{q\hbar}{m^*} k_N |A_N|^2 \end{aligned} \tag{3.20}$$

where f_s is the Fermi-Dirac carrier distribution in the source and T is the transmission probability, specified by: $T = \frac{k_N |A_N|^2}{k_1 |A_1|^2}$

The normalization condition is:

$$|A_1| = \frac{2mf_s}{\pi\hbar^2 k_1} \tag{3.21}$$

The total carrier density in the system is computed from the normalized wavefunctions. In order to obtain the carrier distribution along the surface of graphene, Ψ is integrated over all possible energy levels.

$$\begin{aligned} n(z) &= \int_{E_{min}}^{E_{max}} (|\psi_{e,S}|^2 + |\psi_{e,D}|^2) dE \\ p(z) &= \int_{E_{min}}^{E_{max}} (|\psi_{h,S}|^2 + |\psi_{h,D}|^2) dE \end{aligned} \tag{3.22}$$

where E_{min} is the bottom of the energy band, E_{max} is the vacuum energy level. $\Psi_{e,S}$ and $\Psi_{h,S}$ are wavefunctions, respectively, corresponding to electron and hole injection from the source, and $\Psi_{e,D}$ and $\Psi_{h,D}$ are the equivalent wavefunctions corresponding to injection from the drain. Eq. 3.22 can be solved using the adaptive Simpson's method [36].

The integrations were performed using the adaptive Simpson's method which can be expressed as:

$$\begin{aligned} I_1 &= \int_a^b f(x)dx = \frac{h}{6}(f(a) + 4f(c) + f(b)) \\ I_2 &= \int_a^c f(x)dx + \int_c^b f(x)dx \\ &= \frac{h}{12}(f(a) + 4f(d) + 2f(c) + 4f(e) + f(b) \end{aligned} \tag{3.23}$$

where $c = \frac{a+b}{2}$ $d = \frac{a+c}{2}$ $e = \frac{c+b}{2}$

If $|I_2 - I_1|/15 < \varepsilon$, where ε is a predefined tolerance, the algorithm calls for further division of the integration interval into two, and the adaptive Simpson's method is applied to each subinterval in a recursive manner. In this approach, the points in the integration intervals are non-equidistant, so there are many points around the resonances while there are only few points in other regions.

Using a numerical damping factor, the coupled Schrödinger-Poisson equation model was solved iteratively. An initial assumption of zero charge Q^n distribution on the graphene surface was made and the electrostatic potential V^n was computed from the Poisson program. The new charge density Q_{int}^{n+1} is computed using the electrostatic potential V^n. This new charge density is used for the calculation of the new potential V_{int}^{n+1} and finally the new potential V^{n+1} is calculated as:

$$V^{n+1} = \alpha V_{int}^{n+1} + (1 - \alpha)V^n \tag{3.24}$$

where $0 < \alpha < 1$. The convergence of the system is achieved when the defined criterion is met.

3.3.3 Simulation Procedure

To start the simulation, a guess of the initial charge density inside the device is made, usually zero. The next step is to compute the electron potential inside the device by solving Poisson's equation. The new charge density in the device is computed by using the scattering matrix method to solve the Schrodinger equation. This new charge density is then used to solve the Poisson equation again and these steps are repeated a number of times until the new value of the charge density match the older one. At this point, the criterion for convergence of the system is achieved and other properties of the device are observed via numerical integrations.

3.4 Results

The graphene nanoribbon used in this study has dimensions $20nm \times 4nm$. Results are compared with those obtained from a similar study on carbon nanotubes conducted by Odili [41]. The carbon nanotubes are formed by rolling the nanoribbon resulting in tubes of radius $0.64nm$. For both structures the work-functions of the source and drain regions were taken to be $4.5eV$ and the conduction band edge in the channel in equilibrium is $0.15eV$ above the Fermi energy level. The work function is chosen to be consistent with the value for silver (Ag) used in the experimental work reported in ref [6]. Only the first subband was considered as the energies of the upper subbands exceed the drain voltage in the structures used in this simulation. A single effective mass was used in the model devices to allow

comparison of their output characteristics. The effective mass was $0.0311m_0$ for both electrons and holes, where, m_0 is the free electron mass [17].

Fig. 3.7a shows a three-dimensional (3D) plot of the electron potential energy within the graphene sheet with V_{ds} = 0V and V_{gs} = 0.5V. The electron potential energy, represented by the conduction band edge, is lower at the edges of the sheet due to the wrap around gate. Increasing V_{ds} lowers the conduction band edge in the central region as shown in Fig. 3.7b. Cross-sections of the electron energy profiles along the edge of the sheet and in the centre of the channel, giving a clearer picture of the effect of drain voltage on electron energy, are shown in Figs. 3.7c and 3.7d respectively.

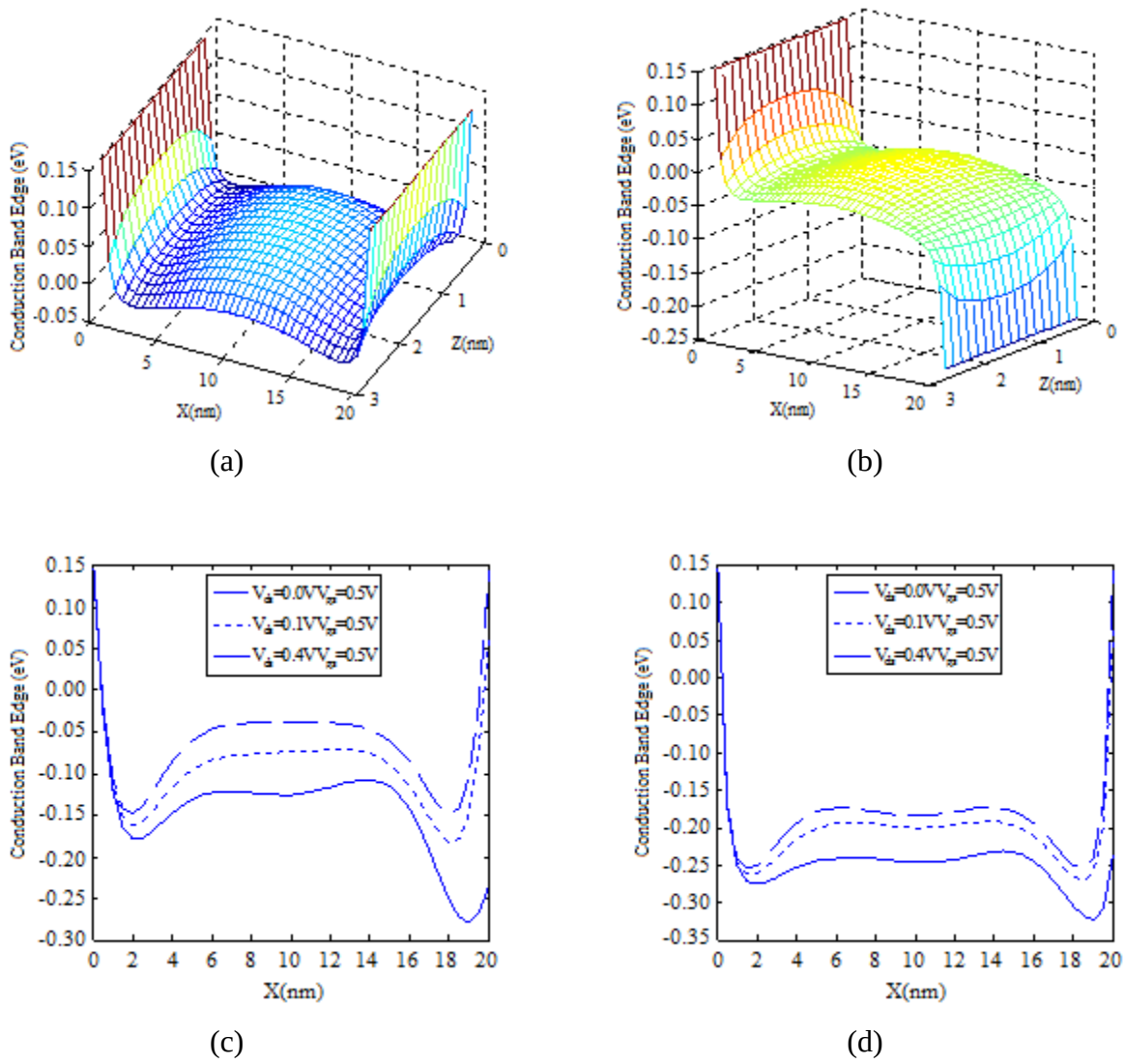

Figure 3.7 Simulation of the potential energy seen by the electrons at $V_{gs} = 0.5V$ (a) 3D view of the conduction band edge at $V_{ds} = 0.0V$ (b) 3D view of the conduction band edge at $V_{ds} = 0.4V$ (c) Conduction band edge along the length of the device for different V_{ds} at the edge of the graphene sheet (d) Conduction band edge along the length of the device for different V_{ds} at the centre of the graphene sheet.

Figures 3.8a and 3.8b show the electron density throughout the graphene sheet resulting from tunneling through the potential barrier at the contact. When the $V_{ds} = 0V$, the electron density is higher at the edges than in the centre, a result consistent with the variation of the conduction band edge. As the drain voltage is increased to $0.4\ V$, the electron density falls within the centre and at the edges. Again,

this can be seen more clearly from the cross-sections of the energy density profile through the centre of the device and at the edges.

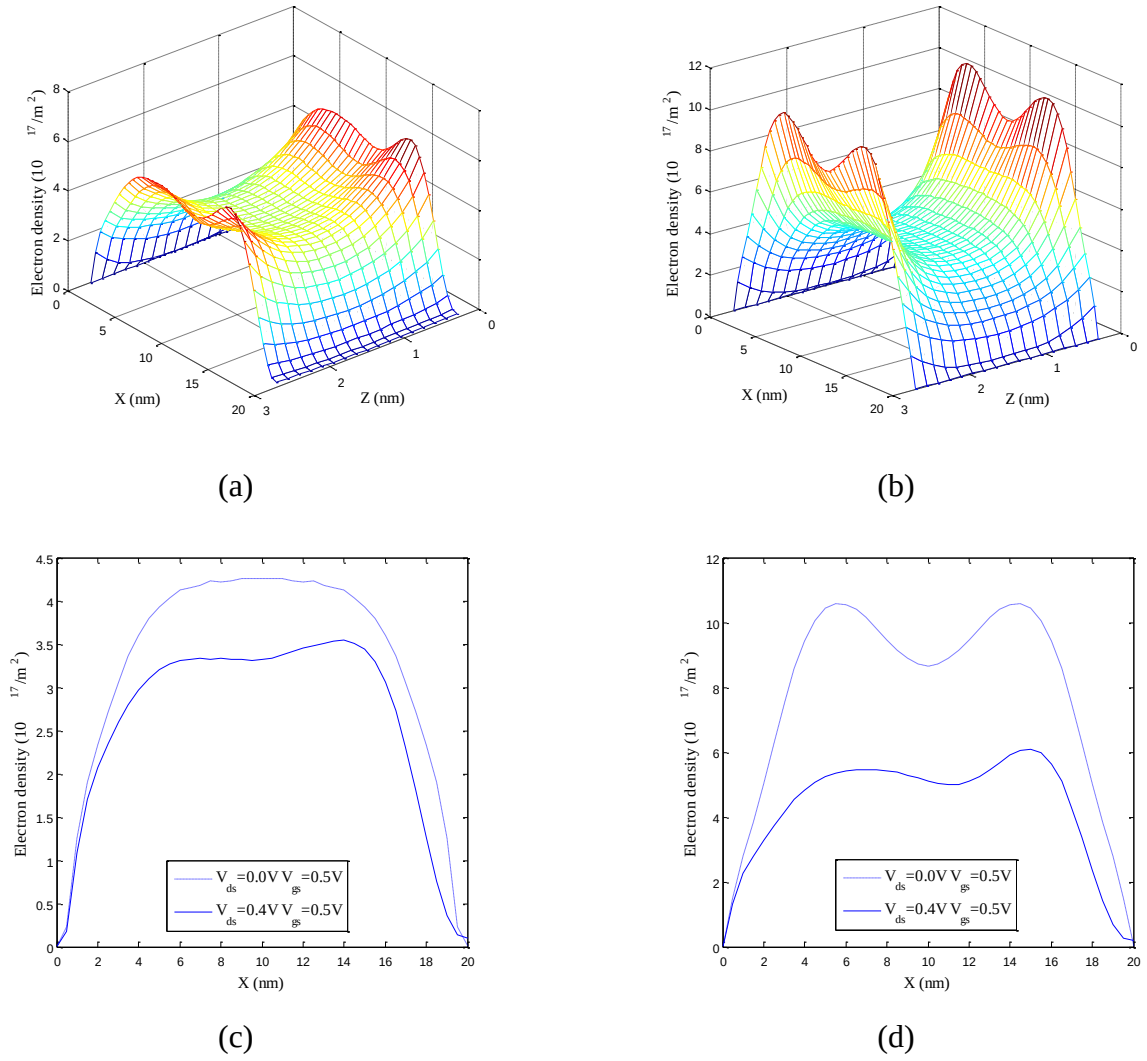

Figure 3.8 Simulation of the carrier density at $V_{gs} = 0.5V$. (a) 3D view of the net carrier density as a function of position at $V_{ds} = 0.0V$. (b) 3D view of the net carrier density as a function of position at $V_{ds} = 0.4V$. (c) Cross-section of carrier density for different V_{ds} at the centre of graphene sheet (d) Cross-section of carrier density for different V_{ds} at the edge of the graphene sheet.

Figures 3.9 (a) and (b), respectively, show the output characteristics of MOSFETs based on a graphene ribbon and a carbon nanotube. The width of the graphene nanoribbon equals the circumference of CNT. Comparing the I-V characteristics of these devices it is observed that for graphene the maximum current drive is achieved at a much lower drain bias. This result suggests that circuits based on graphene MOSFETs may have a superior switching performance than those based on CNTs. The saturation

currents for the graphene and CNT devices are $1.7uA$ and $3.3uA$, respectively. The low bias conductance of the devices can be approximated from the slope of the I-V characteristics. Based on this approximation, the maximum conductance for the graphene and CNT devices are $8.5uS$ and $17uS$, respectively.

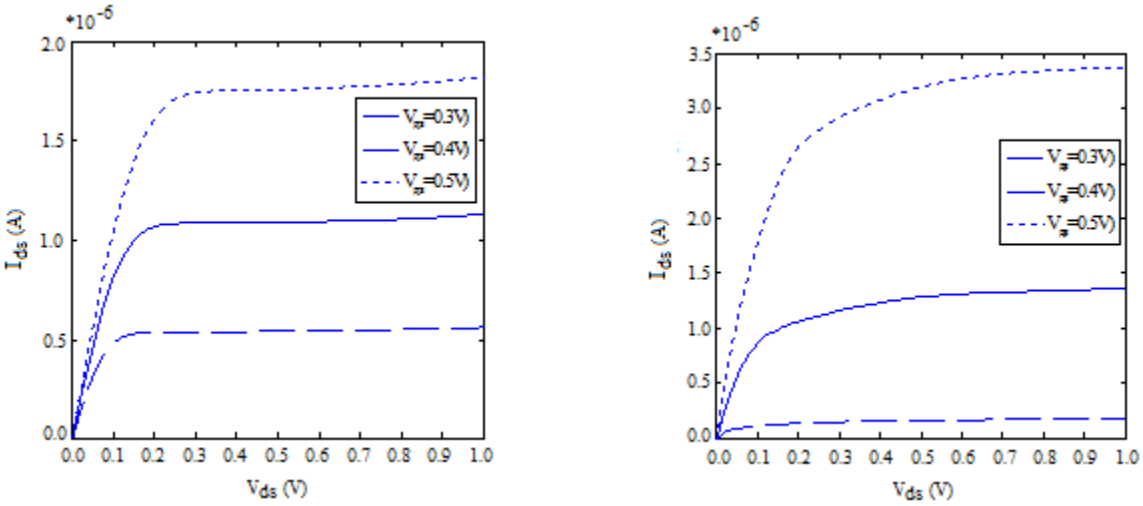

Figure 3.9 I-V characteristics of Graphene (a) and CNT (b)

The physical origin of the difference in the output characteristics can be understood by considering the relationship between the drain current, I_{DS}, the transmission probability, T_E and Fermi Dirac function $f(E)$:

$$I_{DS} = \frac{2e}{h}\int T_E\,(f_s - f_d)dE \tag{3.25}$$

Figures 3.10 (a) – (f) show plots of T_E, $f_s - f_d$ and $T_E(f_s - f_d)$ for the graphene and CNT based MOSFETs at three drain-source voltages, $V_{ds} = 0.1, 0.24$ and $0.4V$. Figures 3.10 (a), (c) & (e) are the results for the graphene-based device while figures 3.10 (b), (d), & (f) are the corresponding results for the CNT-based device. The drain current is represented by the area under the graph of $T_E(f_s - f_d)$ versus energy. The physical difference in the output characteristics of the two devices stems from differences in transmission probabilities. For the graphene based device the transmission probability rises rapidly but oscillates between 80% and 100%. However, in the CNT based device, transmission probability rises slowly with energy and exhibits oscillations between 5% and 90% where $f_s - f_d$ is significant.

$V_{ds} = 0.1V$

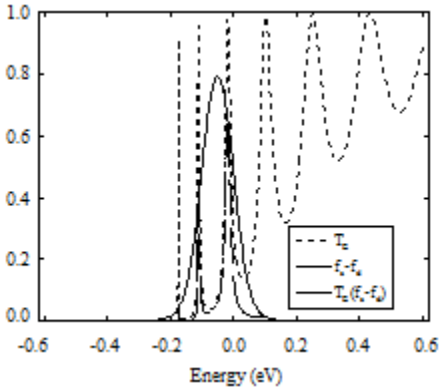

(a)

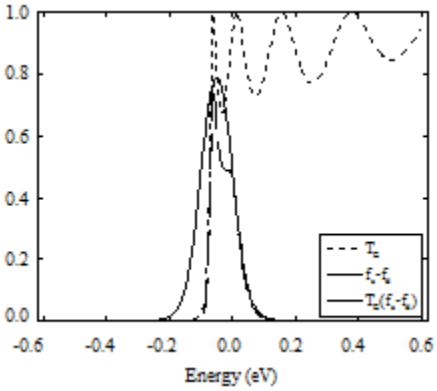

(b)

$V_{ds} = 0.24V$

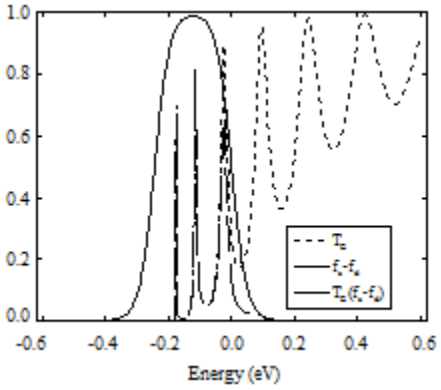

(c)

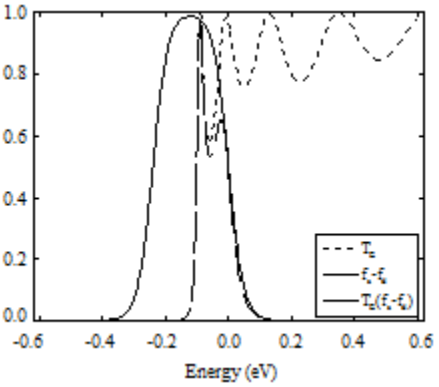

(d)

$V_{ds} = 0.4V$

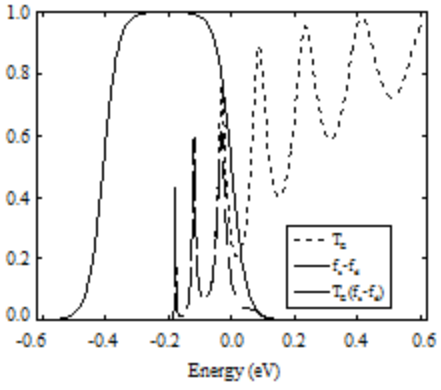

(e)

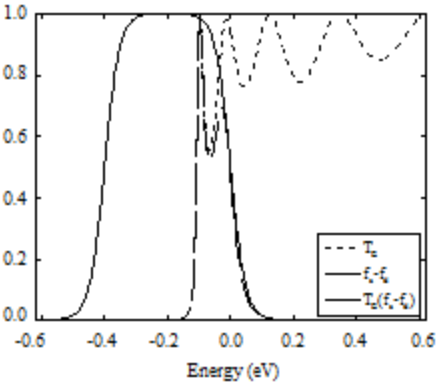

(f)

Figure 3.10 Transmission Probability and Fermi Dirac Distribution for different V_{ds}. Carbon nanotubes – (a), (c), (e) and graphene – (b), (d), (f)

As shown in Fig. 3.9, the current increases until the maximum value of $(f_s - f_d)$ is unity. Beyond that point, the current is mainly determined by T_E while the change in $(f_s - f_d)$ has no effect on the net current. The T_E plot shows that above the conduction band edge all the energy states in graphene make a contribution to the current where the transmission probabilities are well above zero. For a CNT, the transmission probabilities for electrons at some states are close to zero thereby making little contribution to the current and increasing the magnitude of V_{ds} required to obtain maximum current.

3.5 Conclusions

In this work charge transport in MOS systems based on graphene nanoribbons and carbon nanotubes has been modeled and compared. Poisson's equation is discretized in three-dimensions and solved self-consistently with Schrödinger's equation with the latter solved using the scattering matrix method. The band structure of graphene is obtained through a tight-binding Hamiltonian of the armchair-edge nanoribbon. To improve immunity to short channel effects, a fully wrapped gate is assumed for both devices [37].

In the graphene-based FET edge effects influence the energy band structure and charge density. Differences are observed in the output characteristics of the two devices that stem from differences in transmission probabilities. For CNFET's the transmission probability is the same at all points on the circumference of the nanotube. However, the structure chosen for the graphene FET results in potential differences between the edges and the centre of the graphene sheet leading to differences in the amplitudes of the electron wavefunction. The total transmission probability for the graphene FET is, therefore, a summation of transmission probabilities over the width of the graphene nanoribbon. As each element of the summation has the characteristic form exhibited by the CNT structure the total transmission probability for the nanoribbon displays smaller oscillations and a more rapid rise in average value with increasing energy. Comparing the I-V characteristics of these devices it is observed that for graphene the maximum current drive is achieved at a much lower drain bias. This result suggests that circuits based on graphene MOSFETs may have a superior switching performance than those based on CNTs.

Chapter 4 Conductance of Graphene nanoribbons

4.1 Landauer formalism

In chapter 3 we treated Graphene nanoribbon as a quasi-1D conductor. For such a nanoscale system the Landauer Formula is widely used in the calculation of current.

$$I = \frac{2q}{h}\int_{-\infty}^{+\infty} T(E)[f(E-\mu_1) - f(E-\mu_2)]dE \tag{4.1}$$

Here *T(E)* is the transmission coefficient , *f(E)* is the Fermi-Dirac distribution function and μ_1 and μ_2 are the Fermi energies of the left and right contact of the conductor. The coefficient 2 is to take account of electron spin.

Applying a small bias voltage δμ, and writing the Fermi function as $f(E-\mu_1) - f(E-\mu_1+\delta\mu)$ results in a first order Taylor expansion

$$f(E-\mu_1) - f(E-\mu_1+\delta\mu) = -\delta\mu\frac{\partial f(E-\mu_1)}{\partial E} \tag{4.2}$$

The change in current can therefore be written as

$$\delta I = \frac{2q}{h}\int_{-\infty}^{+\infty} -T(E)\delta\mu\frac{\partial f(E-\mu_1)}{\partial E}dE \tag{4.3}$$

and the conductance at the applied source potential, $\mathbb{G}_1$, is given by

$$\begin{aligned}\mathbb{G}(\mu_1) = \frac{\delta I}{\delta\mu/q} &= \frac{2q^2}{h}\int_{-\infty}^{+\infty} -T(E)\frac{\partial f(E-\mu_1)}{\partial E}dE \\ &= \frac{2q^2}{h}T_0\end{aligned} \tag{4.4}$$

Where $T_0 = \int_{-\infty}^{+\infty} T(E)F_T(\mu_1)dE$, $F_T = -\frac{\partial f(E-\mu_1)}{\partial E} = \frac{1}{4k_BT}\mathrm{sech}^2\left(\frac{E}{2k_BT}\right)$ is called the thermal broadening function.

Figure 4.1 is a sketch of the thermal broadening function at different temperatures. Its maximum value is $\frac{1}{4k_BT}$ while its width is proportional to k_BT. The area obtained by integrating F_T is equal to one.

Considering the simplest case where the temperature is 0 K, the thermal broadening function becomes a standard Dirac delta function with area equal to one. As a result (4.4) becomes (μ_1 is changed to E in the expression)

$$\mathbb{G}(E) = \frac{2q^2}{h} T(E) \tag{4.5}$$

(4.4) and (4.5) are called Landauer formulae and will be used in the following calculation of conductance in graphene nanoribbons.

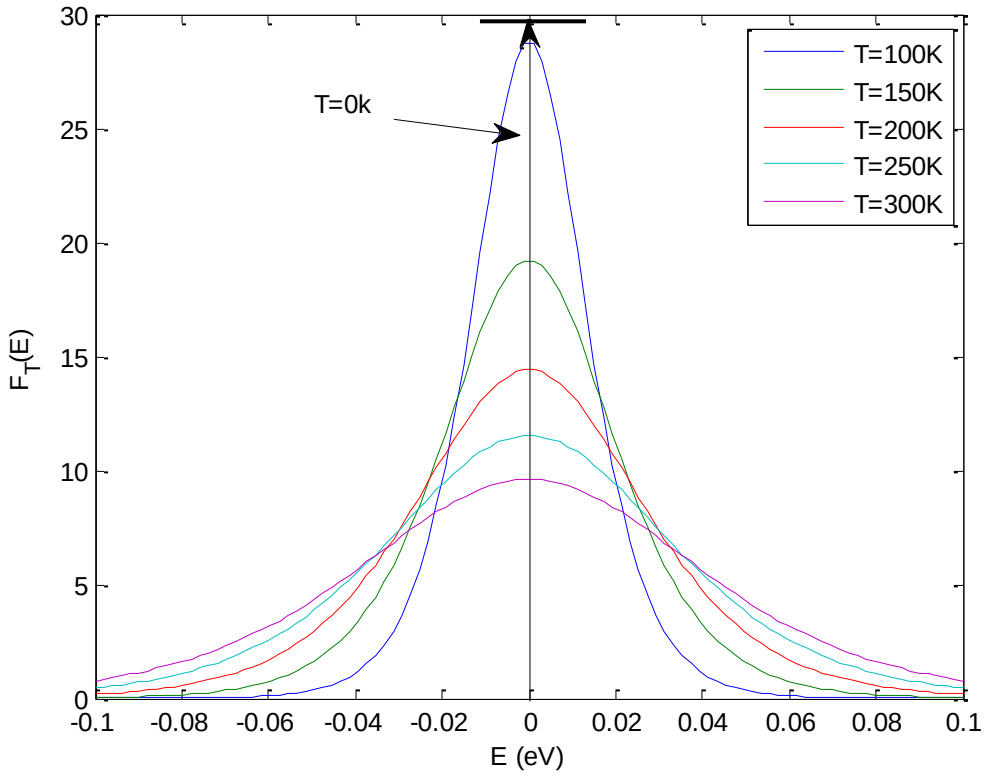

Figure 4.1 Plot of thermal broadening function at different temperatures. At T=0 K the broadening function is a Dirac delta function with area equal to one.

In the Landauer formalism, the nanoscale conductor is assumed to be connected to the contacts by two uniform leads that can be viewed as quantum wires with multiple subbands. If the energy-dispersion relation (E-k relation) is known, a *t-matrix* similar to a microwave waveguide can be formulated using the scattering matrix method. This original method of calculating the transmission in (4.5) is given by [38]

$$T(E) = \sum_m \sum_n |t_{nm}|^2 = \mathrm{Tr}[tt^T] \tag{4.6}$$

Here t is the t-matrix whose element t_{nm} gives the amplitude for an electron incident in mode *m* in lead 1 transmitting to a mode n in lead 2.

4.2 Green's function model

The Nonequilibrium Green's Function (NEGF) is a convenient method for calculating the transmission coefficient. Consider a graphene nanoribbon with 2 semi-infinite contacts shown in Figure 4.2.

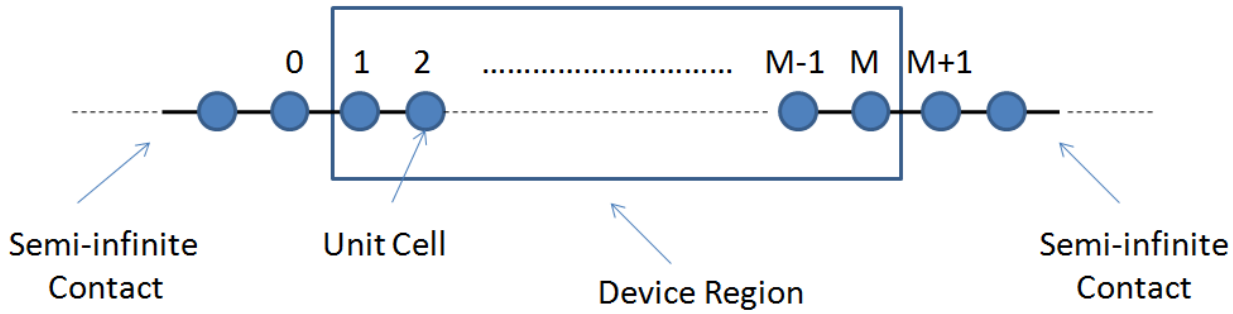

Figure 4.2 quasi-1D model of graphene nanoribbon having infinite contact length

The matrix representation of the Schrodinger equation including the overlap integrals is given by

$$(E\boldsymbol{S} - \boldsymbol{H})\boldsymbol{\phi} = \mathbf{0} \tag{4.7}$$

Where *H and S* are block matrices defined in (2.42). Define $\mathrm{A} = (E + i\eta)\boldsymbol{S} - \boldsymbol{H}$ and $\mathrm{G} = A^{-1}$. We have

$$AG = I \tag{4.8}$$

η is a small positive energy value (10^{-5}eV in this simulation) which circumvents the singular point of the matrix inversion . Matrix A is an infinite large tri-diagonal block matrix whose none zero elements in the *q*th row are

$$\begin{aligned} A_{q,q} &= (E + i\eta)S_{q,q} - H_{q,q} \\ A_{q,q-1} &= (E + i\eta)S_{q,q-1} - H_{q,q-1} = A_{q-1,q}^T \\ A_{q,q+1} &= (E + i\eta)S_{q,q+1} - H_{q,q+1} = A_{q+1,q}^T \end{aligned} \tag{4.9}$$

4.2.1 Green's function in the device region

Matrix G is called the Green's function of the system. If we divide the graphene nanoribbon into a left contact region (unit cells0,-1,-2 …), a device region (unit cells 1,2 … M-1,M) and a right contact region (unit cells M+1,M+2,…) as shown in Figure 4.2, matrices A and G can also be divided into corresponding block matrices, and (4.8) can then be written as

$$\begin{bmatrix} A_{LL} & A_{LD} & O \\ A_{DL} & A_{DD} & A_{DR} \\ O & A_{RD} & A_{RR} \end{bmatrix} \begin{bmatrix} G_{LL} & G_{LD} & G_{LR} \\ G_{DL} & G_{DD} & G_{DR} \\ G_{RL} & G_{RD} & G_{RR} \end{bmatrix} = \begin{bmatrix} I & O & O \\ O & I & O \\ O & O & I \end{bmatrix} \tag{4.10}$$

where *O* represent zero matrices and

$$A_{LL} = \begin{bmatrix} \bullet & \bullet & \bullet & & & & \\ & \bullet & \bullet & \bullet & & & \\ & & A_{-2,-3} & A_{-2,-2} & A_{-2,-1} & & \\ & & & A_{-1,-2} & A_{-1,-1} & A_{-1,0} & \\ & & & & A_{0,-1} & A_{0,0} & \end{bmatrix} \tag{4.11}$$

corresponds to the left semi-infinite contact, while

$$A_{RR} = \begin{bmatrix} A_{M+1,M+1} & A_{M+1,M+2} & & & & & \\ A_{M+2,M+1} & A_{M+2,M+2} & A_{M+2,M+3} & & & & \\ & A_{M+3,M+2} & A_{M+3,M+3} & A_{M+3,M+4} & & & \\ & & \bullet & & \bullet & \bullet & \\ & & & & \bullet & \bullet & \bullet \end{bmatrix} \tag{4.12}$$

corresponds to the right semi-infinite contact, and

$$A_{DD} = \begin{bmatrix} A_{1,1} & A_{1,2} & & & & & & \\ A_{2,1} & A_{2,2} & A_{2,3} & & & & & \\ & \bullet & \bullet & \bullet & & & & \\ & & \bullet & \bullet & \bullet & & & \\ & & & \bullet & \bullet & \bullet & & \\ & & & & A_{M-1,M-2} & A_{M-1,M-1} & A_{M-1,M} & \\ & & & & & A_{M-1,M} & A_{M,M} & \end{bmatrix} \tag{4.13}$$

corresponds to the device region.

$$A_{LD} = \begin{bmatrix} O & O & \bullet & \bullet & O & O \\ O & O & \bullet & \bullet & O & O \\ O & O & \bullet & \bullet & O & O \\ O & O & \bullet & \bullet & O & O \\ A_{0,1} & O & O & \bullet & \bullet & O \end{bmatrix} = A_{DL}^{T} \tag{4.14}$$

corresponds to the coupling between left contact and the device region and

$$A_{RD} = \begin{bmatrix} O & \bullet & \bullet & O & O & A_{M,M+1} \\ O & O & \bullet & \bullet & O & O \\ O & O & \bullet & \bullet & O & O \\ O & O & \bullet & \bullet & O & O \\ O & O & \bullet & \bullet & O & O \end{bmatrix} = A_{DL}^{T} \tag{4.15}$$

corresponds to the coupling between right contact and the device region

From (4.10) we have

$$\begin{aligned} A_{LL}G_{LD} + A_{LD}G_{DD} &= 0 \\ A_{DL}G_{LD} + A_{DD}G_{DD} + A_{DR}G_{RD} &= I \\ A_{RD}G_{DD} + A_{RR}G_{RD} &= 0 \end{aligned} \tag{4.16}$$

Simple manipulation of (4.16) yields

$$[A_{DD} - A_{DL}A_{LL}^{-1}A_{LD} - A_{DR}A_{RR}^{-1}A_{RD}]G_{DD} = I \tag{4.17}$$

(4.17) reduced the infinite Green's function to a finite device Green's function G_{DD} coupling to the right and left contacts. $\Sigma_L = A_{DL}A_{LL}^{-1}A_{LD}$ and $\Sigma_R = A_{DR}A_{RR}^{-1}A_{RD}$ are referred to as the self energies of the left and right contacts respectively. Note that because A_{DL} A_{LD} A_{DR} and A_{RD} only contain one block matrix element we only need to seek the last diagonal block in A_{LL}^{-1} and the first diagonal block in A_{RR}^{-1} in order to calculate self energies.

4.2.2 Surface Green's function

Define $g^L = A_{LL}^{-1}$ and $g^R = A_{RR}^{-1}$ as the Green's functions of the isolated semi-infinite contacts. The surface Green's functions $g_{0,0}^L$ and $g_{M+1,M+1}^R$ (also called the left and right connected Green's functions) of the Left and Right contacts are the Green's function elements corresponding to the boundary unit cell 0 and M + 1 respectively,

$$g_{0,0}^L = A_{LL_{0,0}}^{-1} \text{ and } g_{M+1,M+1}^R = A_{LL_{M+1,M+1}}^{-1} \tag{4.18}$$

(4.17) can be rewritten as

$$G_{DD} = [A_{DD} - \Sigma_L - \Sigma_R]^{-1} \tag{4.19}$$

where

$$\Sigma_{L_{1,1}} = A_{1,0} g_{0,0}^L A_{0,1} \text{ and } \Sigma_{R_{M,M}} = A_{M,M+1} g_{M+1,M+1}^L A_{M+1,M} \tag{4.20}$$

All other elements in Σ_L and Σ_R are zero. The surface green's functions $g_{0,0}^L$ and $g_{M+1,M+1}^L$ are the main elements required to solve (4.19). The method to obtain these surface green's functions will be discussed in 4.3.

4.2.3 Simple model

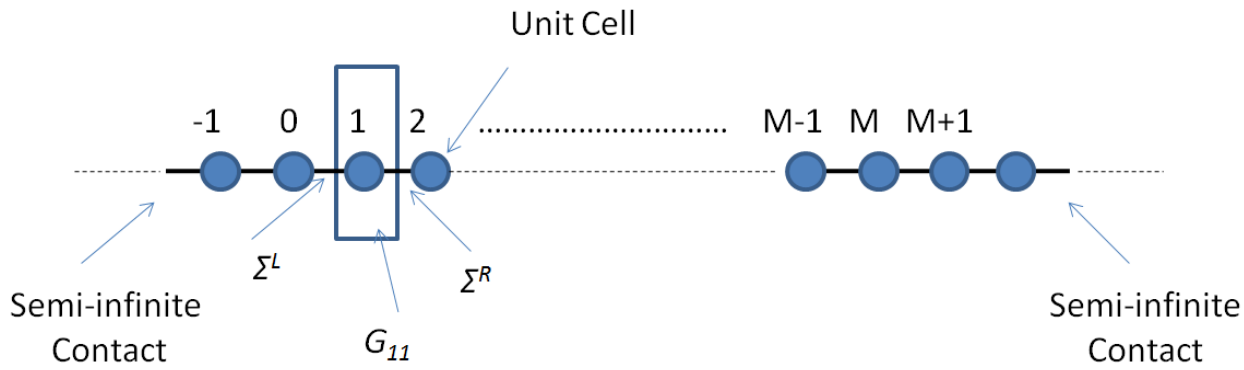

Figure 4.3 quais-1D model of infinite length graphene nanoribbon with only one unit cell in the device region

When only the conductance of the graphene nanoribbon is of interest, the potential on the entire nanoribbon is constant and we can divide the unit cells 2 to M so that the Green's function in the device

only corresponds to the remaining unit cell 1. Figure 4.3 shows a Schematic diagram of this model. As in 4.19 the Green's function of the first unit cell is given by

$$[(E+i\eta)S_{11}-H_{11}-\Sigma_L^{11}-\Sigma_R^{11}]G_{11}=I \tag{4.21}$$

where

$$\begin{aligned}\Sigma_L^{11}&=[(E+i\eta)S_{10}-H_{10}]g_{0,0}^{L}[(E+i\eta)S_{01}-H_{01}]\\ \Sigma_R^{11}&=[(E+i\eta)S_{12}-H_{12}]g_{2,2}^{L}[(E+i\eta)S_{21}-H_{21}]\end{aligned} \tag{4.22}$$

The transmission is then given by

$$\begin{aligned}T(E)&=Tr[\Gamma_L G_{11}\Gamma_R G_{11}]\\ \text{with } \Gamma_{L,R}&=i[\Sigma_{L,R}^{11}-\Sigma_{L,R}^{11}]\end{aligned} \tag{4.23}$$

The local density of states on the site *j* in unit cell 1 is given by [38]

$$n_j=-\frac{1}{\pi}\mathrm{Im}[G_{11_{(j,j)}}] \tag{4.24}$$

where $G_{11_{(j,j)}}$ is the matix element of Green's function at site *j*.

The advantage of this simple model is that it avoids the inversion of the large matrix $[A_{DD}-\Sigma_L-\Sigma_R]^{-1}$ so that no matrix larger than $2N_0X2N_0$ is involved.

4.3 Iterative scheme for the surface Green's function

4.3.1 Matrix quadratic equations

The semi-infinite matrix A_{LL} can be divided into

$$A_{LL}=\begin{bmatrix}A_{L'L'} & A_{L'0}\\ A_{0L'} & A_{00}\end{bmatrix} \tag{4.25}$$

where

$$A_{L'L'} = \begin{bmatrix} \bullet & \bullet & \bullet & & \\ & \bullet & \bullet & \bullet & \\ & & A_{-2,-3} & A_{-2,-2} & A_{-2,-1} \\ & & & A_{-1,-2} & A_{-1,-1} \end{bmatrix}$$

$$A_{0L'} = \begin{bmatrix} \bullet & \bullet & O & O & A_{0,-1} \end{bmatrix} \tag{4.26}$$

$$A_{L'0} = A_{0L'}^{\dagger}$$

As in (4.17) we have

$$\begin{aligned} g_{0,0}^{L} &= \left[A_{0,0} - A_{0L'} A_{L'L'}^{-1} A_{L'0}\right] \\ &= \left[A_{0,0} - A_{0,-1} g_{-1,-1}^{L'} A_{-1,0}\right] \end{aligned} \tag{4.27}$$

Note that the potential through the entire left contact is constant; the coupling Hamiltonian matrix and overlap matrix between nearest unit cells do not change for the unit cell index.

$$\begin{aligned} &ES_{0,0} - H_{0,0} = A_{0,0} = A_{-1,-1} = A_{-2,-2} = \ldots \\ &ES_{-1,0} - H_{-1,0} = A_{-1,0} = A_{-2,-1} = A_{-3,-2} = \ldots \\ &ES_{0,-1} - H_{0,-1} = A_{0,-1} = A_{-1,-2} = A_{-2,-3} = \ldots \\ &A_{0,-1} = A_{-1,0}^{\dagger} \end{aligned} \tag{4.28}$$

Furthermore because both $A_{L'L'}$ and A_{LL} are semi-infinite with the same block elements we have

$$A_{L'L'} = A_{LL} \text{ and } g_{0,0}^{L} = g_{-1,-1}^{L'} \tag{4.29}$$

Combining (4.29) with (4.27) we obtain the matrix quadratic equation for $g_{0,0}^{L}$

$$g_{0,0}^{L} = [A_{0,0} - A_{0,-1} g_{0,0}^{L} A_{-1,0}] \tag{4.30}$$

The matrix quadratic equation for $g_{M+1,M+1}^{R}$ can be obtained in a similar manner

$$g_{M+1,M+1}^{R} = [A_{0,0} - A_{-1,0} g_{M+1,M+1}^{R} A_{0,-1}] \tag{4.31}$$

Given an initial guess of $g_{0,0}^{L}$ and $g_{M+1,M+1}^{R}$ the updated value of $g_{0,0}^{L}$ and $g_{M+1,M+1}^{R}$ can be calculated from (4.30) and (4.31). Repeating this process until the new values change very little, the final value of the surface green's functions are obtained.

4.3.2 Sancho-Rubio iterative scheme

The matrix quadratic equation gives a simple iterative scheme for calculating surface green's functions. However, they must be calculated by iterating until self-consistency is achieved. This usually involves more than 50 iterations. Especially, when $g^L_{0,0}$ or $g^R_{M+1,M+1}$ is in the neighbourhood of singularities when several hundred iterations may be needed to get an accurate result [39].

Sancho et.al. developed an iterative scheme which converges much faster. After *n* iterations 2^n unit cells instead of *n* unit cells are taken into account. The original Sancho-Rubio iterative scheme only included the Hamiltonian matrix ***H*** while the overlap matrix ***S*** is assumed to be an identity matrix. Here we extend this method using a more general expression so that ***S*** is also taken into account.

Starting from the definition of the Green's function of left semi-infinite contact, $A_{LL}g^L = I$, we have

$$\begin{bmatrix} \bullet & \bullet & \bullet & & & \\ & \bullet & \bullet & \bullet & & \\ & & A_{-2,-3} & A_{-2,-2} & A_{-2,-1} & \\ & & & A_{-1,-2} & A_{-1,-1} & A_{-1,0} \\ & & & & A_{0,-1} & A_{0,0} \end{bmatrix} \begin{bmatrix} \bullet & \bullet & \bullet & \bullet & \bullet & \bullet \\ \bullet & \bullet & \bullet & \bullet & \bullet & \bullet \\ \bullet & \bullet & \bullet & \bullet & g^L_{-2,-1} & g^L_{-2,0} \\ \bullet & \bullet & \bullet & g^L_{-1,-2} & g^L_{-1,-1} & g^L_{-1,0} \\ \bullet & \bullet & \bullet & g^L_{0,-2} & g^L_{0,-1} & g^L_{0,0} \end{bmatrix} = I \tag{4.32}$$

Taking the block matrix multiplication of A_{LL} and the last column of g^L we obtain

$$\begin{bmatrix} \bullet & \bullet & \bullet & & & \\ & \bullet & \bullet & \bullet & & \\ & & A_{-2,-3} & A_{-2,-2} & A_{-2,-1} & \\ & & & A_{-1,-2} & A_{-1,-1} & A_{-1,0} \\ & & & & A_{0,-1} & A_{0,0} \end{bmatrix} \begin{bmatrix} \bullet \\ \bullet \\ g^L_{-2,0} \\ g^L_{-1,0} \\ g^L_{0,0} \end{bmatrix} = \begin{bmatrix} \bullet \\ \bullet \\ O \\ O \\ I \end{bmatrix} \tag{4.33}$$

(4.33) is equivalent to a series of matrix equations as shown below

$$
\begin{aligned}
A_{0,0}g^L_{0,0} &= I - A_{0,-1}g^L_{-1,0} \\
A_{-1,-1}g^L_{-1,0} &= -A_{-1,0}g^L_{0,0} - A_{-1,-2}g^L_{-2,0} \\
A_{-2,-2}g^L_{-2,0} &= -A_{-2,-1}g^L_{-1,0} - A_{-2,-3}g^L_{-3,0}
\end{aligned} \tag{4.34}
$$

....

Using the relation in (4.28) again, the general term of (4.34) can be written as

$$
\begin{aligned}
g^L_{-n,0} &= A^{-1}_{0,0}\left(-A_{0,-1}g^L_{-n+1,0} - A_{0,-1}g^L_{-n-1,0}\right) \\
&= t_0 g^L_{-n+1,0} + \tilde{t_0} g^L_{-n-1,0}
\end{aligned} \tag{4.35}
$$

with $t_0 = -A^{-1}_{0,0}A_{0,-1}$ and $\tilde{t_0} = -A^{-1}_{0,0}A_{0,-1}$

Applying (4.35) to $g^L_{-n+1,0}$ and $g^L_{-n-1,0}$ we have

$$
\begin{aligned}
g^L_{-n,0} &= t_0\left(t_0 g^L_{-n+2,0} + \tilde{t_0} g^L_{-n,0}\right) + \tilde{t_0}\left(t_0 g^L_{-n,0} + \tilde{t_0} g^L_{-n-2,0}\right) \\
g^L_{-n,0} &= t_1 g^L_{-n+2,0} + \tilde{t_1} g^L_{-n-2,0}
\end{aligned}
$$

where

$$
\begin{aligned}
t_1 &= (I - t_0\tilde{t}_0 - \tilde{t}_0 t_0)^{-1} t_0^2 \\
\tilde{t}_1 &= (I - t_0\tilde{t}_0 - \tilde{t}_0 t_0)^{-1} \tilde{t}_0{}^2
\end{aligned} \tag{4.36}
$$

Equation (4.36) is isomorphic to equation (4.35) and the process can be repeated iteratively. After *i* iterations we have

$$
g^L_{-n,0} = t_i g^L_{-n+2^i,0} + \tilde{t}_i g^L_{-n-2^i,0}
$$

where

$$
\begin{aligned}
t_i &= (I - t_{i-1}\tilde{t}_{i-1} - \tilde{t}_{i-1} t_{i-1})^{-1} t_{i-1}^2 \\
\tilde{t}_i &= (I - t_{i-1}\tilde{t}_{i-1} - \tilde{t}_{i-1} t_{i-1})^{-1} \tilde{t}_{i-1}^2
\end{aligned} \tag{4.37}
$$

Using (4.37) the following chain of equation is obtained

$$
\begin{aligned}
g^L_{-1,0} &= t_0 g^L_{0,0} + \tilde{t}_0 g^L_{-2,0} \\
g^L_{-2,0} &= t_1 g^L_{0,0} + \tilde{t}_1 g^L_{-4,0}
\end{aligned} \tag{4.38}
$$

$$g^L_{-4,0} = t_2 g^L_{0,0} + \tilde{t}_2 g^L_{-8,0}$$

…

$$g^L_{-2^n,0} = t_n g^L_{0,0} + \tilde{t}_n g^L_{-2^{n+1},0}$$

where

$$\begin{aligned} g^L_{-1,0} &= t_0 g^L_{0,0} + \tilde{t}_0 g^L_{-2,0} \\ &= (t_0 + \tilde{t}_0 t_1) g^L_{0,0} + \tilde{t}_1 g^L_{-4,0} \\ &= (t_0 + \tilde{t}_0 t_1 + \tilde{t}_0 \tilde{t}_1 t_2) g^L_{0,0} + \tilde{t}_2 g^L_{-8,0} \\ &= (t_0 + \tilde{t}_0 t_1 + \cdots + \tilde{t}_0 \ \ldots \ \tilde{t}_{n-1} t_n) g^L_{0,0} + \tilde{t}_n g^L_{-2^{n+1},0} \end{aligned} \tag{4.39}$$

The process is repeated until $t_n \tilde{t}_n < \delta$ with δ arbitrarily small. $g^L_{-2^{n+1},0} \approx 0$. (4.39) then gives

$$g^L_{-1,0} = \theta g^L_{0,0} \quad \text{with} \quad \theta = t_0 + \tilde{t}_0 t_1 + \tilde{t}_0 \tilde{t}_1 t_2 + \cdots + \tilde{t}_0 \tilde{t}_1 \tilde{t}_2 \cdots t_n \tag{4.40}$$

Substituting (4.40) into the first equation in (4.34) the surface Green's function of the left contact can be obtained from

$$\begin{aligned} g^L_{0,0} &= \left(A_{0,0} + A_{0,-1}\,\theta\right)^{-1} \\ &= [ES_{0,0} - H_{0,0} - (ES_{0,-1} - H_{0,-1})\theta]^{-1} \end{aligned} \tag{4.41}$$

Similarly defining

$$\tilde{\theta} = \tilde{t}_0 + t_0 \tilde{t}_1 + t_0 t_1 \tilde{t}_2 + \cdots + t_0 t_1 t_2 \cdots \tilde{t}_n \tag{4.42}$$

the surface Green's function of the left contact can be obtained from

$$g^L_{M+1,M+1} = [ES_{0,0} - H_{0,0} - (ES_{-1,0} - H_{-1,0})\theta]^{-1} \tag{4.43}$$

4.4 Results

In this section we simulate the conductance of different types of graphene nanoribbon and nanoribbon junctions including the effects of defects.

4.4.1 Quantization of conductance

Armchair nanoribbon

We look firstly at the $N_0=13$ armchair graphene nanoribbon shown in Figure 4.4.

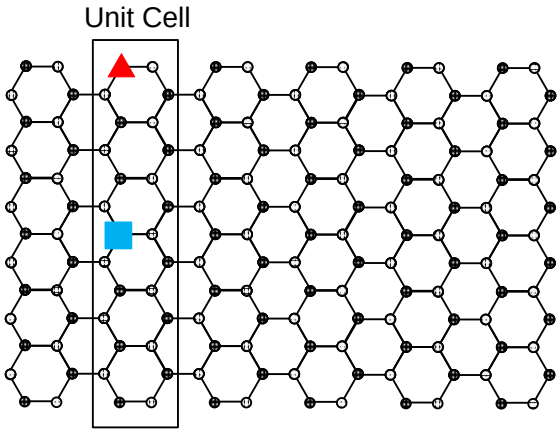

Figure 4.4 $N_0=13$ armchair graphene nanoribbon. The rectangle shows the unit cell and the triangle and square, edge and centre defects, respectively.

Defining the carbon atoms in the rectangle as a unit cell and using a first-nearest neighbour tight-binding Hamiltonian with the parameter γ_0=-2.66eV, the bandstructure of the nanoribbon is obtained and plotted in figure 4.5.

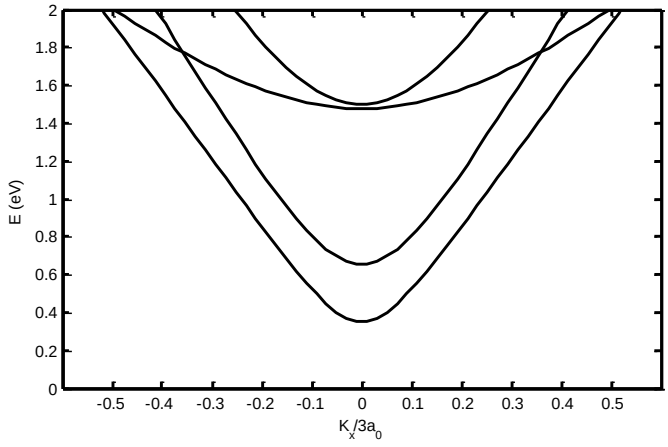

Figure 4.5 Energy bandstructure of an $N_0=13$ armchair graphene nanoribbon

Using the simple Green's function model described in section 4.3 the transmission probability *T(E)* is calculated in the energy range [0 - 2eV]. The conductance $\mathbb{G}(E)$ is then obtained using (4.5) and (4.4) at temperatures, T=0K and T=300K respectively. Figure 4.6 shows these results.

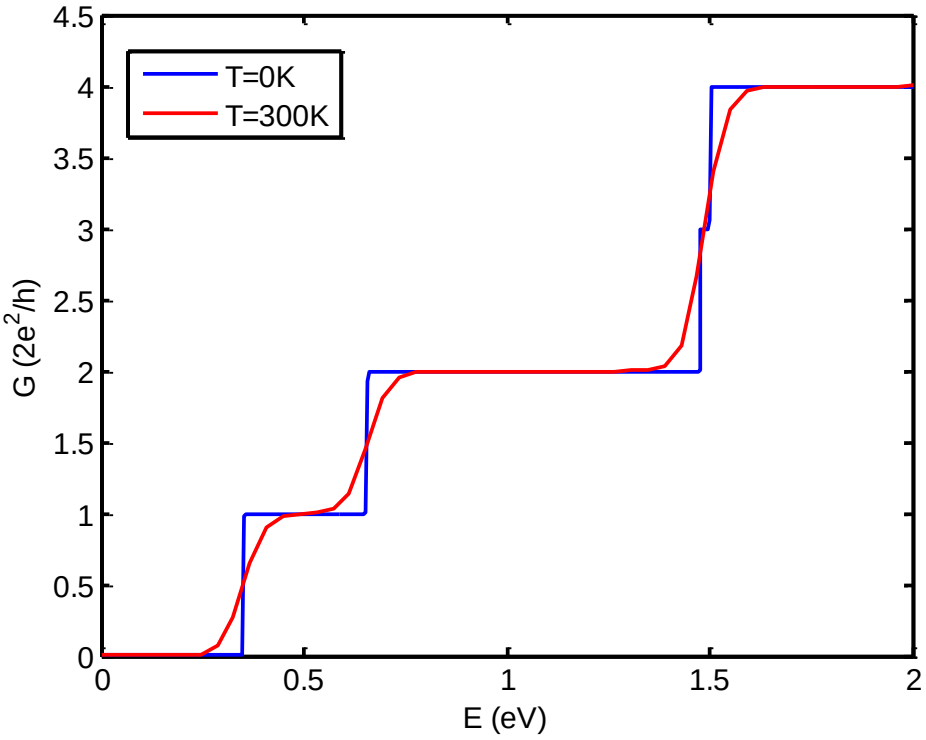

Figure 4.6 Calculated conductance of a N_0=13 armchair graphene nanoribbon at different temperature.

It can be clearly observed that the conductance of the nanoribbon is quantized at both low temperature and room temperature, although the step-like conductance is smoothed by the thermal broadening function in the latter case.

The quantization of the conductance can be explained by reference to the bandstructure of the nanoribbon. In figure 4.5 the 4 conduction bands in the range [0 - 2eV] are plotted. Within this energy range electrons can only be transported in the 4 conduction bands. Each of the conduction bands contributes one unit of the fundamental ballistic conductance $\frac{2q^2}{h}$.

Steps in conductance occur at T=0K at energies corresponding to conduction band edges at 0.35eV, 0.66eV, 1.48eV and 1.51eV.

Zigzag nanoribbon

Figure 4.7 shows an N_0=8 zigzag nanoribbon with a unit defined by the rectangle.

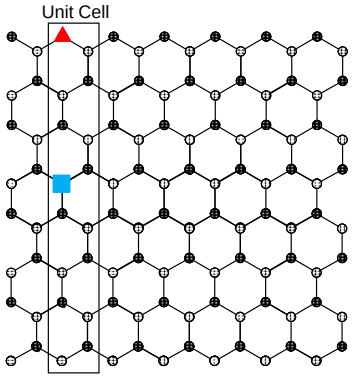

Figure 4.7 *N_0=8* zigzag graphene nanoribbon. The rectangle shows the unit cell and the triangle and square, edge and centre defects, respectively.

The conductance of the nanoribbon is calculated using same method used for the armchair nanoribbon. Figure 4.8 shows the calculation result. Note that because all zigzag nanoribbons are metallic there is no bandgap and the nanoribbon has a minimum conductance of $\frac{2q^2}{h}$ even when *E=0 eV.*

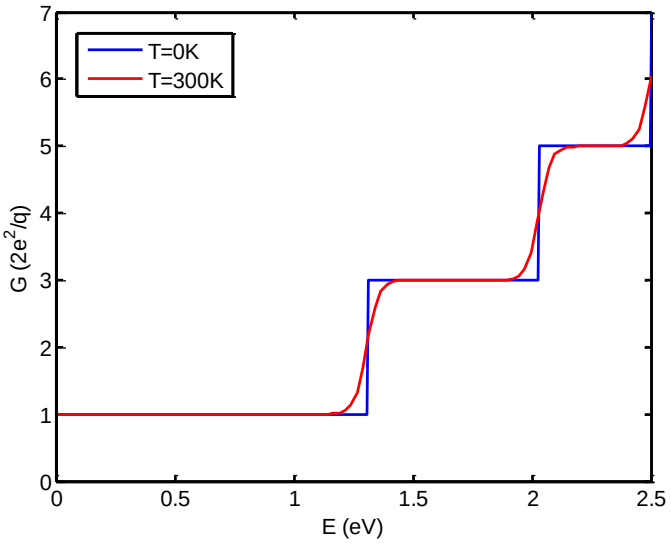

Figure 4.8 Calculated conductance of a *N_0=8* zigzag graphene nanoribbon at different temperatures.

4.4.2 Effects of defects

The triangles and squares in figures 4.4 and 4.7 correspond, respectively, to edge and centre defects (vacancies). Figure 4.9 shows the conductance and local density of states of an N_0=13 armchair the GNR shown in figure 4.4.

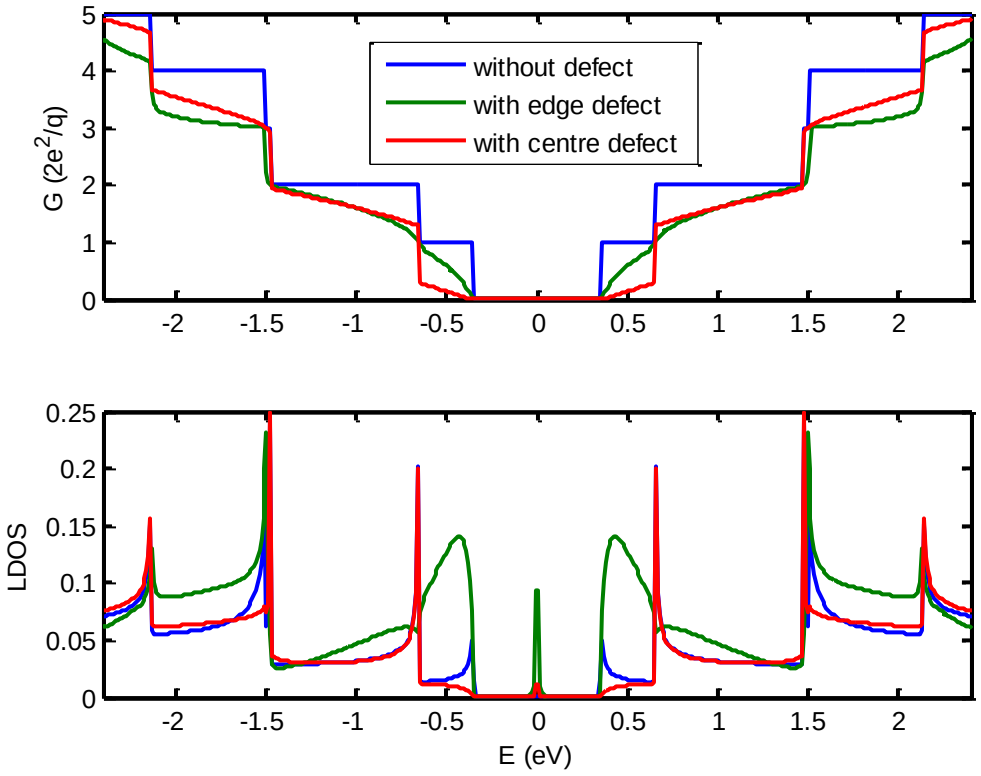

Fig 4.9 Conductance and local density of states of the N_0=13 armchair GNR shown in figure 4.4. Blues line are for GNRs without defects, while green lines are for a GNRs with an edge defect (triangle in figure 4.4) and red lines are for the GNRs with a centre defect (rectangle in figure 4.4).

Clearly even minor defects have a significant effect on the conductance of graphene nanoribbons, an effect that can be potentially be exploited in device applications. The defects are also observed to have a strong effect on the local density of states.

Figure 4.10 shows the conductance and local density of states of the N_0=8 zigzag GNR shown in figure 4.7.

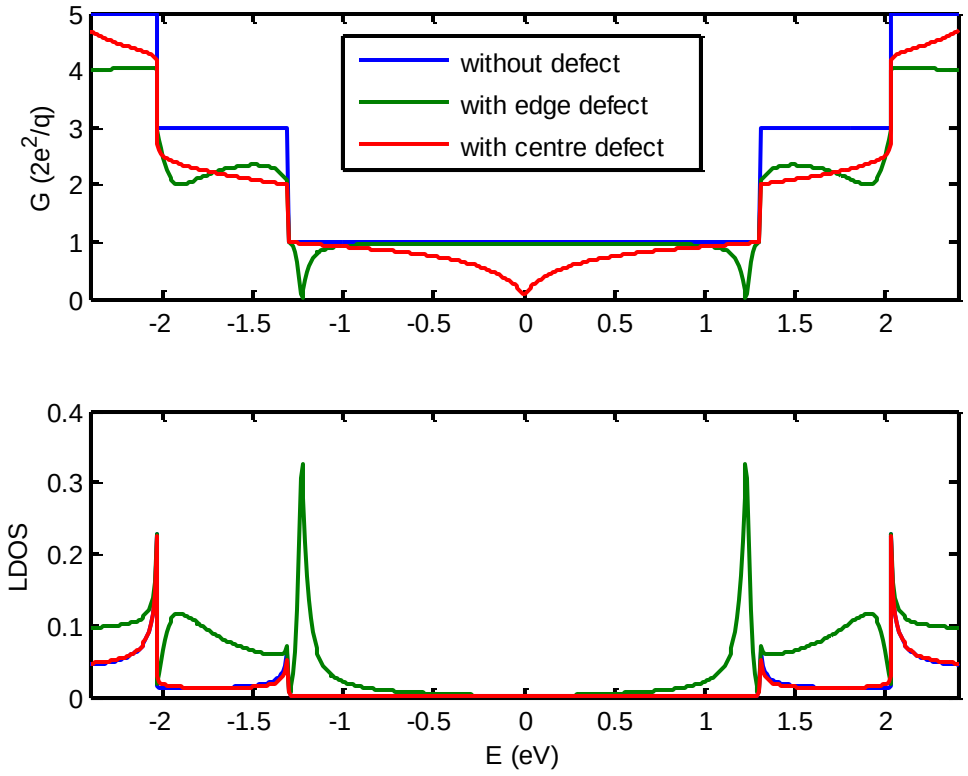

Figure 4.10 Conductance and local density of states of the N_0=8 zigzag GNR shown in figure 4.7. Blues lines are for GNRs without defects, while green lines are for a GNRs with an edge defect (triangle in figure 4.7), and red lines are for the GNRs with a centre defect (rectangle in figure 4.7).

As expected the energy band gap expected for a GNR ribbon with N_0=8 is larger than for the N_0=13 GNR. The conductance and local density of states are again affected by the presence of defects but in this case the changes are different.

4.4.3 Conductance of graphene junctions

Figure 4.9 shows two types of graphene junctions containing defects. Single vacancy defects indicated by a triangle and a rectangle are referred to as type A and type B.

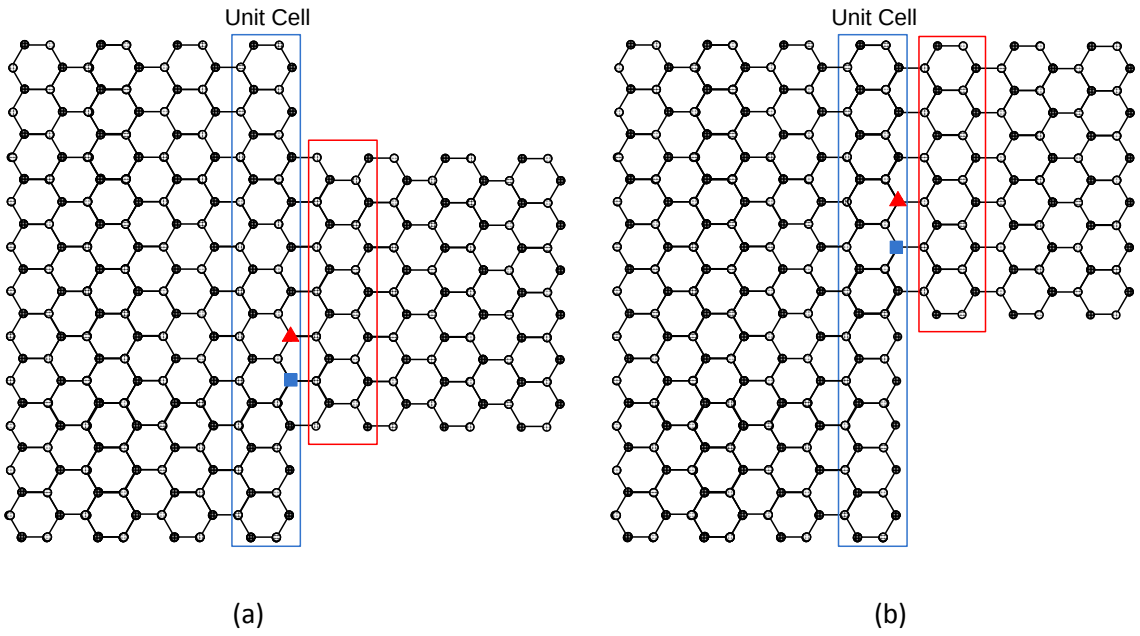

Figure 4.9 two types of metal-semiconductor junctions: (a) A GNR with index N_0=23 connected to a GNR with index N0=13 in the centre; (b) The same type of GNRs as in (a) but connected at the edge. Single defects of type A are indicated by a triangle while type B defects are represented by rectangles.

Figure 4 10 (a) and (b) compares the conductance of a graphene armchair-edge nanoribbon of index N=13 and metal/semiconductor junction formed with the nanoribbon when defects are absent and when they are present.

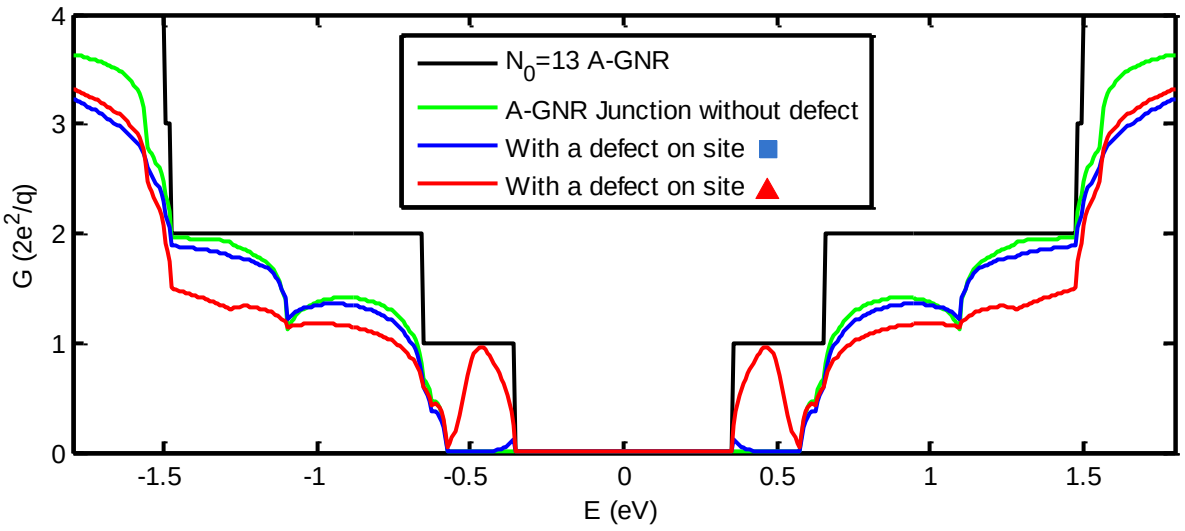

Figure 4.10(a) Conductance vs Energy for the junction shown in Figure 4.9, (a) using first nearest-neighbour parameters.

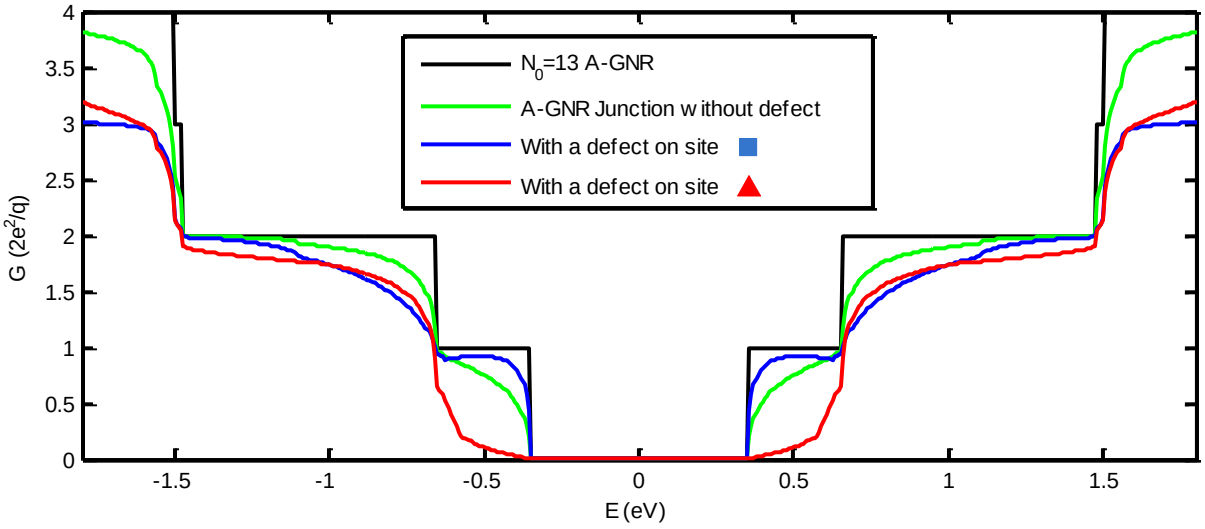

Figure 4.10(b) Conductance vs Energy for the junction shown in Figure 4.9, (b) using first nearest-neighbour parameters.

Significant differences in conductivity are observed suggesting the possibility of engineering structures using vacancies.

4.4.4 Effects of third-nearest neighbour interactions

Figures 4.11(a) and (b) compare the conductance of a graphene armchair-edge nanoribbon of index N=13 and metal/semiconductor junction formed with the nanoribbon assuming first and third nearest-neighbour interactions respectively. For graphene nanoribbons differences are observed in the step-like structure, reflecting differences in the calculated band structure. When only first nearest-neighbour interactions are considered the conductance of the conduction and valence bands is always symmetric as determined by the formulation of the energy dispersion relation.

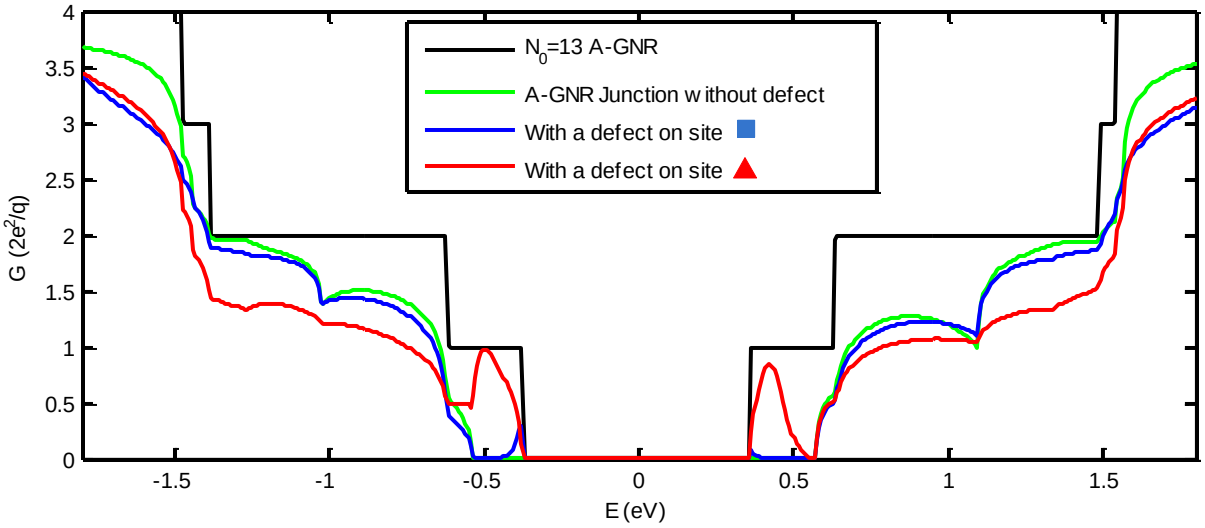

Figure 4.11 (a) Conductance vs Energy for the junction shown in Figure 4.9, (a) using third nearest-neighbour parameters

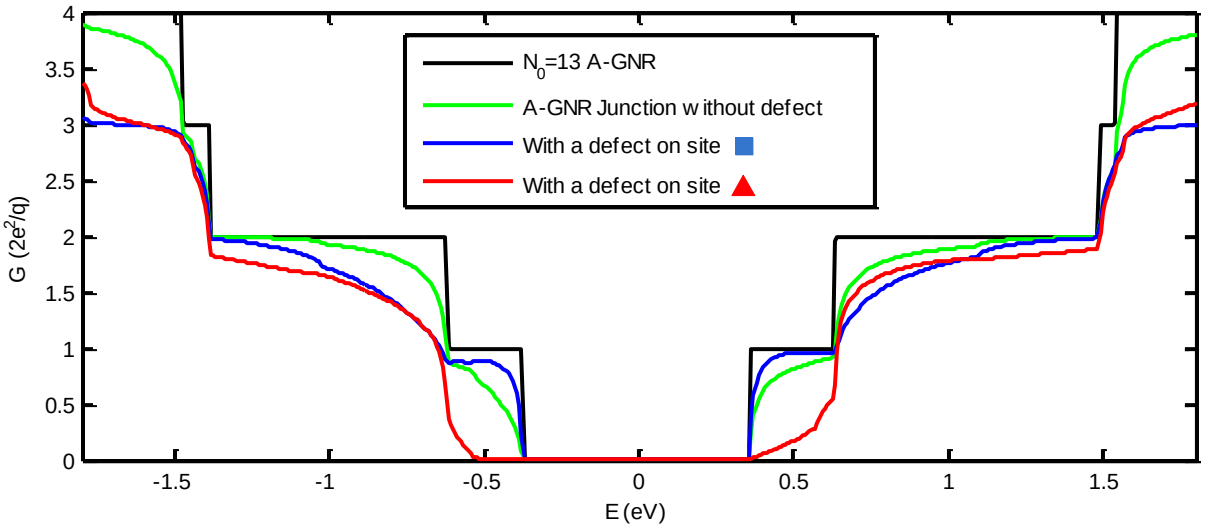

Figure 4.11 (b) Conductance vs Energy for the junction shown in Figure 4.9, (b) using third nearest-neighbour parameters

In the case of graphene nanoribbons the conductance within a few electronvolts of the Fermi energy is symmetrical for both first and third nearest-neighbour interactions. However, it is notable that at higher energies (not shown in the figure) overlap integrals introduced by third nearest neighbour interactions result in asymmetry between the conductance in the conduction and valence bands. For metal/semiconductor junctions significant differences in conductivity occur even at low energies due to mismatches of the subbands. Asymmetry in the conduction and valence band conductance (absent for first nearest neighbour interactions) are also apparent when third nearest neighbours interactions are included in the Green's function. Differences are also seen when defects are incorporated within a

metal/semiconductor junction, an interesting system explored by Hong et.al. [40]. In this work vacancies are introduced in the lattice at the positions marked by the solid rectangle and triangle in figure 4.9 and the conductance obtained in each case. Hong et. al derive a coupling term associated with associated with differences in band structure. For third nearest-neighbour the solution to the coupling strength must be derived numerically.

4.4.5 Strained graphene nanoribbons

In chapter 2 it was shown that strain can modify the energy band structure of graphene nanoribbons. Figure 4.11 shows the effects of uniaxial strain on the conductance and local density of states graphene nanoribibbons of width N_0=13. Strain has been used to improve the performance of silicon MOSFETs and the results below suggest that strain can be used to engineer the current-voltage characteristics of devices formed on graphene nanoribbons.

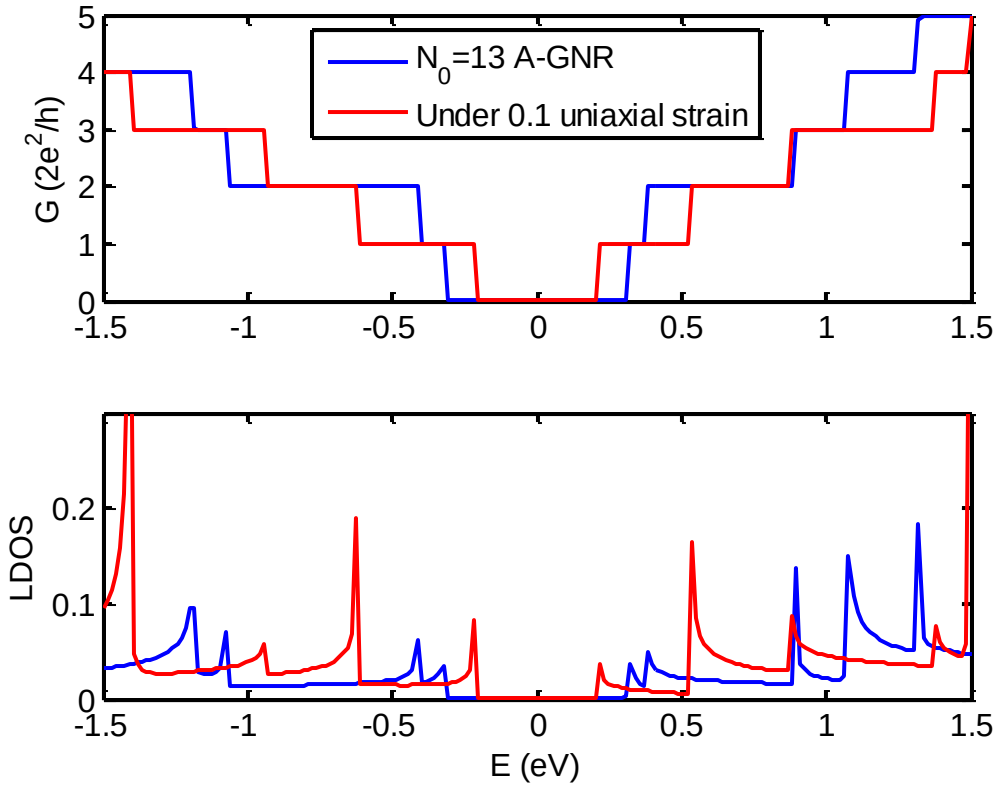

Figure 4.12 Conductance and local density of states of an N_0=13 armchair GNR (blue lines). Red lines show the conductance and LDOS under a uniaxial strain of 0.1.

4.5 Conclusions

In this chapter we have determined the conductance of nanoribbons and graphene metal/semiconductor junctions using a NEGF formalism based on the tight binding method approximated to first nearest-neighbour and third nearest-neighbour including the effects of defects. We observe that defects play a significant role in determining the conductance and local density of states of nanoribbons and junctions formed with them when first nearest neighbour interactions are considered. The position of the defect also affects the observed conductivity. However, few studies report the effect of third nearest neighbour interactions on conductivity. In this work we find significant differences are observed suggesting the commonly used first nearest-neighbour approximation may not be sufficiently accurate in some circumstances. The most notable differences are observed when defects are introduced in the metal/semiconductor junctions. Finally, we find that strain can be used to engineer the conductance and local density of states of graphene nanoribbons.

Chapter 5 Conclusions and further work

Since the invention of the transistor in 1947 the rapid and continuous growth of the semiconductor industry has been based on one material, silicon. Other materials such as gallium arsenide have found uses in specialised applications but the market for semiconductor devices has been dominated by those based on silicon. Although this dominance is expected to continue into the foreseeable future the formation of freeform graphene in the mid-1980s has revolutionised semiconductor device research. As described in the introduction to this thesis the number of research publications has risen exponentially since the mid-1980s. Although the development of this material provides excellent opportunities for research, the large number of researchers studying graphene has led to strong competition within the area. Prior to the fabrication of graphene devices carbon nanotubes were being considered as the basis for electronic devices in a post-silicon era. However, carbon nanotubes are not compatible with silicon technology whereas graphene is as it is planar. One of the main attractions of graphene is the very high electron mobility is observed within the material. However, graphene has demonstrated other surprising properties including unusual magnetic effects. This thesis reports research on charge transport within graphene devices. A comparison is made or charged transport within carbon nanotubes and graphene nanoribbons. Different techniques are explored for modelling charge transport within graphene-based devices. In particular, a self consistent solution of Schrödinger and Poisson's equations is developed. Charge transport within graphene nanoribbons is studied using the nonequilibrium Green's function.

In order to obtain the current and voltage characteristics of a semiconductor device the energy dispersion relation of the material on which it is based must first be obtained. The energy band structure of graphene has been known for long time and had been determined using the tight binding model. However, the energy dispersion relations of structures formed with graphene can depend on geometry, edge effects and the model parameters used in the simulation. The second chapter of this thesis was therefore devoted to the determination of the energy band structures of graphene and graphene nanoribbons using different tight binding models. Initially, only first nearest-neighbour interactions were considered but it was found that third nearest-neighbour interactions must be taken into account to achieve an accurate bandstructure. The method was used to determine the bandstructure and energy bandgap in armchair and zigzag graphene nanoribbons. It was observed that the computational efficiency could be improved using a quasi-one dimensional model of graphene nanoribbons to obtain

the energy bandstructures with no loss of accuracy. The effect of edge distortion and strain on the energy bandstructures of graphene nanoribbons were also considered. Parabolic and non-parabolic expressions were used to fit to the energy bandstructures in order to obtain an effective mass for use in a Poisson-Schrödinger solver developed in chapter 3 to simulate charge transport in a graphene field effect transistor.

In Chapter 3 charge transport in MOS systems based on graphene nanoribbons and carbon nanotubes were modeled and compared. Poisson's equation was discretized in three-dimensions and solved self-consistently in conjunction with Schrödinger's equation, with the latter solved using the scattering matrix method. For the MOSFET a wrap-around gate structure was used. In the graphene-based FETs edge effects influence the energy band structure and charge density. Differences were observed in the output characteristics of the two devices which were ascribed to differences in transmission probabilities. By symmetry the transmission probability was the same at all points on the circumference of the carbon nanotube nanotube. Whereas for graphene nanoribbons potential differences between the edges and the centre of the graphene resulted in differences in transmission probabilities, Integrated across the width of the nanoribbon these differences caused disparities in the I-V characteristics of the two devices. The maximum current drive of the graphene device was observed to occur at a much lower drain bias than for the CNT device. This result suggests that circuits based on graphene MOSFETs may have a superior switching performance than those based on CNTs.

In chapter 4 of the thesis the conductance of graphene nanoribbons and graphene metal/semiconductor junctions were obtained using a NEGF formalism based on the tight binding method approximated to first nearest-neighbour and third nearest-neighbour including the effects of defects. It was observed that defects play a significant role in determining the conductance and local density of states of nanoribbons and junctions formed with them when first nearest neighbour interactions are considered. The position of the defect was also observed to affect the observed conductivity. An important result of this work is the observation that the there are significant differences in the conductivities obtained using the first nearest-neighbour approximation commonly made in the literature and the third nearest neighbour approximation employed here. More notable differences are observed when defects are introduced in the metal/semiconductor junctions. The effect of strain on graphene devices strain was also analysed and we conclude that it can be employed to engineer the conductance and local density of states of graphene nanoribbons.

A natural extension of this research is the formulation of a self consistent analysis coupling Poisson's equation with the nonequilibrium Green's function formalism. This has been developed but insufficient results were obtained to include within the thesis. From a theoretical point of view future work could examine the effects of defects and strain within the self consistent device model. Ideally the analysis presented in this work should be compared with experimental results. The very rapid progress made by experimentalists should ensure that results become available in the near future.

References

[1] P. R. Wallace, "The Band Theory of Graphite," *Physical Review,* vol. 71, p. 622, 1947.

[2] K. S. Novoselov*, et al.*, "Electric Field Effect in Atomically Thin Carbon Films," vol. 306, ed: American Association for the Advancement of Science, 2004, pp. 666-669.

[3] K. S. Novoselov*, et al.*, "Two-dimensional gas of massless Dirac fermions in graphene," *Nature,* vol. 438, pp. 197-200, 2005.

[4] D. L. John*, et al.*, "A Schrodinger-Poisson Solver for Modeling Carbon Nanotube FETs," *Proc. NSTI Nanotech,* vol. 3, pp. 65-68, 2004.

[5] M. Pourfath*, et al.*, "A fast and stable Poisson-Schrodinger solver for the analysis of carbon nanotube transistors," *Journal of Computational Electronics,* vol. 5, pp. 155-159, 2006.

[6] G. Gu*, et al.*, "Field effect in epitaxial graphene on a silicon carbide substrate," *Applied Physics Letters,* vol. 90, pp. 253507-3, 2007.

[7] D. L. John*, et al.*, "Quantum capacitance in nanoscale device modeling," *Journal of Applied Physics,* vol. 96, pp. 5180-5184, 2004.

[8] M. M. Jose and S. Ashok, "Carrier density and effective mass calculations in carbon nanotubes," *physica status solidi (b),* vol. 245, pp. 2558-2562, 2008.

[9] G. Pennington and N. Goldsman, "Semiclassical transport and phonon scattering of electrons in semiconducting carbon nanotubes," *Physical Review B,* vol. 68, p. 045426, 2003.

[10] R. Saito*, et al.*, *Physical Properties of Carbon Nanotubes*. London: Imperial College Press, 1998.

[11] J. Fernandez-Rossier*, et al.*, "Electronic structure of gated graphene and graphene ribbons," *Physical Review B,* vol. 75, p. 205441, 2007.

[12] A. Bostwick*, et al.*, "Renormalization of graphene bands by many-body interactions," *Solid State Communications,* vol. 143, pp. 63-71, Jul 2007.

[13] Kim, "Carbon Wonderland," *Scientific American Magazine,* vol. 298, pp. 90-97, 2008.

[14] Y. Hatsugai*, et al.*, "Topological aspects of graphene - Dirac fermions and the bulk-edge correspondence in magnetic fields," *European Physical Journal-Special Topics,* vol. 148, pp. 133-141, Sep 2007.

[15] X. Z. Yan*, et al.*, "Thermo-Electric Power of Dirac Fermions in Graphene," *Arxiv preprint arXiv:0904.3303,* 2009.

[16] K. Nakada*, et al.*, "Edge state in graphene ribbons: Nanometer size effect and edge shape dependence," *Physical Review B,* vol. 54, pp. 17954-17961, 1996.

[17] D. Gunlycke and C. T. White, "Tight-binding energy dispersions of armchair-edge graphene nanostrips," *Physical Review B,* vol. 77, p. 115116, 2008.

[18] S. Reich*, et al.*, "Tight-binding description of graphene," *Physical Review B,* vol. 66, p. 035412, 2002.

[19] R. Kundu, "Tight binding parameters for graphene," *Arxiv preprint arXiv:0907.4264,* 2009.

[20] A. K. Geim and K. S. Novoselov, "The rise of graphene," *Nature Mater,* vol. 6, pp. 183-191, 2007.

[21] Y. Klymenko and O. Shevtsov, "Analytical Tight-binding Approach for Ballistic Transport through Armchair Graphene Ribbons: Exact Solutions for Propagation through Step-like and Barrier-like Potentials," 2008.

[22] J. B. Oostinga*, et al.*, "Gate-tunable band-gap in bilayer graphene devices," *eprint arXiv: 0707.2487,* 2007.

[23] H. Zheng*, et al.*, "Analytical study of electronic structure in armchair graphene nanoribbons," *J. Phys. Soc. Jpn Phys Rev B,* vol. 75, p. 165414, 2006.

[24] L. Pisani*, et al.*, "Electronic structure and magnetic properties of graphitic ribbons," *Physical Review B,* vol. 75, p. 64418, 2007.

[25] A. Akin and G. Neil, "Electron transport and full-band electron-phonon interactions in graphene," *Journal of Applied Physics,* vol. 103, p. 053702, 2008.
[26] T. Ando, "Anomaly of optical phonons in bilayer graphene," *Journal of the Physical Society of Japan,* vol. 76, Oct 2007.
[27] V. Barone*, et al.*, "Electronic structure and stability of semiconducting graphene nanoribbons," *Nano Letters,* vol. 6, pp. 2748-2754, Dec 2006.
[28] A. Bostwick*, et al.*, "Band structure and many body effects in graphene," *European Physical Journal-Special Topics,* vol. 148, pp. 5-13, Sep 2007.
[29] M. Fischetti*, et al.*, "Six-band [bold k p] calculation of the hole mobility in silicon inversion layers: Dependence on surface orientation, strain, and silicon thickness," *Journal of Applied Physics,* vol. 94, p. 1079, 2003.
[30] T. E. Chang*, et al.*, "Conductivity and mechanical properties of well-dispersed single-wall carbon nanotube/polystyrene composite," *Polymer,* vol. 47, pp. 7740-7746, 2006.
[31] R. Ribeiro*, et al.*, "Strained graphene: tight-binding and density functional calculations," *New Journal of Physics,* vol. 11, p. 115002, 2009.
[32] Y. Lu and J. Guo, "Band gap of strained graphene nanoribbons," *Nano Research,* vol. 3, pp. 189-199, 2010.
[33] R. Grassi*, et al.*, "Tight-binding and effective mass modeling of armchair graphene nanoribbon FETs," *Solid-state electronics,* vol. 53, pp. 462-467, 2009.
[34] D. Schmerek and W. Hansen, "Exchange and correlation effects on the ground states of quantum wires," *Physical Review B,* vol. 60, p. 4485, 1999.
[35] D. N. Christodoulides*, et al.*, "Analytical calculation of the quantum-mechanical transmission coefficient for a triangular, planar-doped potential barrier," *Solid-state electronics,* vol. 28, pp. 821-822, 1985.
[36] J. N. Lyness, "Notes on the adaptive Simpson quadrature routine," *Journal of the ACM (JACM),* vol. 16, pp. 483-495, 1969.
[37] Y. Ouyang*, et al.*, "Scaling Behaviors of Graphene Nanoribbon FETs: A Three-Dimensional Quantum Simulation Study," *Electron Devices, IEEE Transactions on,* vol. 54, pp. 2223-2231, 2007.
[38] S. Datta, *Quantum Transport: Atom to Transistor*: Cambridge University Press, 2005.
[39] M. Sancho*, et al.*, "Quick iterative scheme for the calculation of transfer matrices: application to Mo (100)," *Journal of Physics F: Metal Physics,* vol. 14, pp. 1205-1215, 1984.
[40] S. Hong*, et al.*, "Metal-semiconductor junction of graphene nanoribbons," *Applied Physics Letters,* vol. 92, p. 083107, 2008.
[41] D. I. Odili, "Simulation and Microwave Measurement of the Conductivity of Carbon Nanotubes," *PhD Thesis*, University of Birmingham, 2011.
[42] D. I. Odili, Y. Wu, *et al.*, "Modeling charge transport in graphene nanoribbons and carbon nontubes using a Schrödinger-Poisson solver," *Journal of Applied Physics*, vol. 106, 024509, 2009.
[43] Y. Wu, *et al.,* "Conductance of graphene nanoribbon junctions and the tight binding model," *Nanoscale Research Letters*, vol. 6, no. 62, 2011.

Appendix 1

Published papers

JOURNAL OF APPLIED PHYSICS **106**, 024509 (2009)

Modeling charge transport in graphene nanoribbons and carbon nanotubes using a Schrödinger-Poisson solver

D. I. Odili, Y. Wu, P. A. Childs,[a] and D. C. Herbert
Department of Electronic, Electrical and Computer Engineering, The University of Birmingham, Birmingham B15 2TT, United Kingdom

(Received 28 April 2009; accepted 12 June 2009; published online 27 July 2009)

Interest in carbon-based electronics has been stimulated in recent years, initially through the discovery of carbon nanotubes, but recently with the formation of graphene layers. In this paper metal-oxide-semiconductor (MOS) systems based on these carbon structures are used to model and compare charge transport within them. Schrödinger's equation is solved self-consistently with Poisson's equation, using the scattering matrix method. A tight-binding model is used to determine the energy band structure in graphene. The current-voltage characteristics of MOS devices based on graphene and those based on carbon nanotubes demonstrate significant differences associated with their respective transmission probabilities. © *2009 American Institute of Physics*.
[DOI: 10.1063/1.3174430]

Nanoscale Research Letters
a SpringerOpen Journal

NANO EXPRESS Open Access

Conductance of Graphene Nanoribbon Junctions and the Tight Binding Model

Y Wu, PA Childs*

Abstract

Planar carbon-based electronic devices, including metal/semiconductor junctions, transistors and interconnects, can now be formed from patterned sheets of graphene. Most simulations of charge transport within graphene-based electronic devices assume an energy band structure based on a nearest-neighbour tight binding analysis. In this paper, the energy band structure and conductance of graphene nanoribbons and metal/semiconductor junctions are obtained using a third nearest-neighbour tight binding analysis in conjunction with an efficient nonequilibrium Green's function formalism. We find significant differences in both the energy band structure and conductance obtained with the two approximations.

Introduction

Since the report of the preparation of graphene by Novoselov et al. [1] in 2004, there has been an enormous and rapid growth in interest in the material. Of all the allotropes of carbon, graphene is of particular interest to the semiconductor industry as it is compatible with planar technology. Although graphene is metallic, it can be tailored to form semiconducting nanoribbons, junctions and circuits by lithographic techniques. Simulations of charge transport within devices based on this new technology exploit established techniques for low dimensional structures [2,3]. The current flowing through a semiconducting nanoribbon formed between two metallic contacts has been established using a nonequilibrium Green's Function (NEGF) formalism based coupled with an energy band structure derived using a tight binding Hamiltonian [4-7]. To minimise computation time, the nearest-neighbour tight binding approximation is commonly used to determine the energy states and overlap is ignored. This assumption has also been used for calculating the energy states of other carbon-based materials such as carbon nanotubes [8] and carbon nanocones [9]. Recently, Reich et al. [10] have demonstrated that this approximation is only valid close to the K points, and a tight binding approach including up to third nearest-neighbours gives a better approximation to the energy dispersion over the entire Brillouin zone.

In this paper, we simulate charge transport in a graphene nanoribbon and a nanoribbon junction using a NEGF based on a third nearest-neighbour tight binding energy dispersion. For transport studies in nanoribbons and junctions, the formulation of the problem differs from that required for bulk graphene. Third nearest-neighbour interactions introduce additional exchange and overlap integrals significantly modifying the Green's function. Calculation of device characteristics is facilitated by the inclusion of a Sancho-Rubio [11] iterative scheme, modified by the inclusion of third nearest-neighbour interactions, for the calculation of the self-energies. We find that the conductance is significantly altered compared with that obtained based on the nearest-neighbour tight binding dispersion even in an isolated nanoribbon. Hong et al. [12] observed that the conductance is modified (increased as well as decreased) by the presence of defects within the lattice. Our results show that details of the band structure can significantly modify the observed conductivities when defects are included in the structure.

Theory

The basis for our analysis is the hexagonal graphene lattice shown in Figure 1. $\mathbf{a_1}$ and $\mathbf{b_1}$ are the principal vectors of the unit cell containing two carbon atoms belonging to the two sub-lattices. Atoms on the concentric circles of increasing radius correspond to the nearest-neighbours, second nearest-neighbours and third nearest-neighbours, respectively.

* Correspondence: p.a.childs@bham.ac.uk
School of Electronic, Electrical and Computer Engineering, University of Birmingham, B15 2TT, Birmingham, UK.

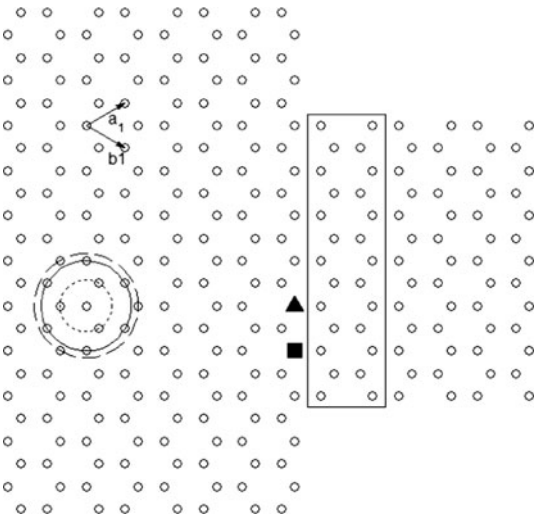

Figure 1 Armchair-edge graphene metal (index *N* = 23)/ semiconductor (index *N* = 13) junction. The *rectangle* shows the semiconductor unit cell, and the *concentric circles* of increasing radius show first, second and third nearest-neighbours, respectively.

Saito et al. [8] derived the dispersion relation below using a nearest-neighbour tight binding analysis including the overlap integral s_0.

$$E^{\pm}(\mathbf{k}) = \frac{\varepsilon_{2p} \mp \gamma_0\sqrt{f(\mathbf{k})}}{1 \mp s_0\sqrt{f(\mathbf{k})}} \tag{1}$$

Here, $f(k) = 3 + 2\cos \mathbf{k}\cdot\mathbf{a_1} + 2\cos \mathbf{k}\cdot\mathbf{b_1} + 2\cos \mathbf{k}\cdot(\mathbf{a_1} - \mathbf{b_1})$ and the parameters, ε_{2p}, γ_0 and s_0 are obtained by fitting to experimental results or ab initio calculations.

Most analyses of charge transport in graphene-based structures simplify the result further by ignoring s_0. Reich et al. [10] derived the dispersion relation for graphene based on third nearest-neighbours. In this work, the energy band structure of a graphene nanoribbon including third nearest-neighbour interactions is obtained from the block Hamiltonian and overlap matrices given below for the unit cell defined by the rectangle in Figure 1.

$$E\begin{bmatrix} S_{0,0} & S_{0,1} & & & & \\ & \ddots & & & & \\ & S_{n,n-1} & S_{n,n} & S_{n,n+1} & & \\ & & & \ddots & & \\ & & & S_{N,N-1} & S_{N,N} \end{bmatrix}\begin{bmatrix} \phi_0 \\ \vdots \\ \phi_n \\ \vdots \\ \phi_N \end{bmatrix} = \begin{bmatrix} H_{0,0} & H_{0,1} & & & & \\ & \ddots & & & & \\ & H_{n,n-1} & H_{n,n} & H_{n,n+1} & & \\ & & & \ddots & & \\ & & & H_{N,N-1} & H_{N,N} \end{bmatrix}\begin{bmatrix} \phi_0 \\ \vdots \\ \phi_n \\ \vdots \\ \phi_N \end{bmatrix} \tag{2}$$

For the nth row of the above equation, we have

$$\begin{aligned} &H_{n,n-1}\phi_{n-1} + H_{n,n}\phi_n + H_{n,n+1}\phi_{n+1} \\ &\quad - E(S_{n,n-1}\phi_{n-1} + S_{n,n}\phi_n + S_{n,n+1}\phi_{n+1}) = 0 \end{aligned} \tag{3}$$

Considering the energy dispersion in the direction of charge transport, the Bloch form of the wavefunction ensures that $\phi_n \sim e^{ikn}$. Substitution of ϕ_n into the above equation yields the secular equation

$$\begin{aligned} &\det[H_{n,n-1}e^{-ik} + H_{n,n} + H_{n,n+1}e^{ik} \\ &\quad - E(S_{n,n-1}e^{-ik} + S_{n,n} + S_{n,n+1}e^{ik})] = 0 \end{aligned} \tag{4}$$

In the case of first nearest approximation without orbital overlap, $S_{n,n-1}$ and $S_{n,n+1}$ are empty matrices. To facilitate comparison with published results, we use an armchair-edge with index [13] $N = 13$ as our model nanoribbon. In the paper by Reich, tight binding parameters were obtained by fitting the band structure to that obtained by ab initio calculations. Recently, Kundo [14] has reported a set of tight biding parameters based on fitting to a first principle calculation but more directly related to the physical quantities of interest. These parameters have been utilised in our calculation and are presented below for third nearest-neighbour interactions (Table 1).

Figure 2 compares the energy band structure of the modelled armchair-edge graphene nanoribbon obtained from the first nearest-neighbour tight binding method with that obtained by including up to third nearest-neighbours. Agreement is reasonable close to the K point but significant discrepancies occur at higher energies.

Conductance of Graphene Nanoribbons and Junctions

Conductance in graphene nanoribbons and metal/semiconductor junctions is determined using an efficient nonequilibrium Green's function formalism described by Li and Lu [15]. The retarded Green's function is given by

$$G = [E^{+}S - H - \Sigma^{L} - \Sigma^{R}]^{-1} \tag{5}$$

Here, $E^{+} = E + i\eta$ and η is a small positive energy value (10^{-5} eV in this simulation) which circumvents the singular point of the matrix inversion [16]. H is a tight binding Hamiltonian matrix including up to third nearest-neighbours, and S is the overlap matrix. Open

Table 1 Tight binding parameters [14]

Neighbours	E_{2p}(eV)	γ_0(eV)	γ_1(eV)	γ_2(eV)	s_0	s_1	s_2
3rd-nearest	-0.45	-2.78	-0.15	-0.095	0.117	0.004	0.002

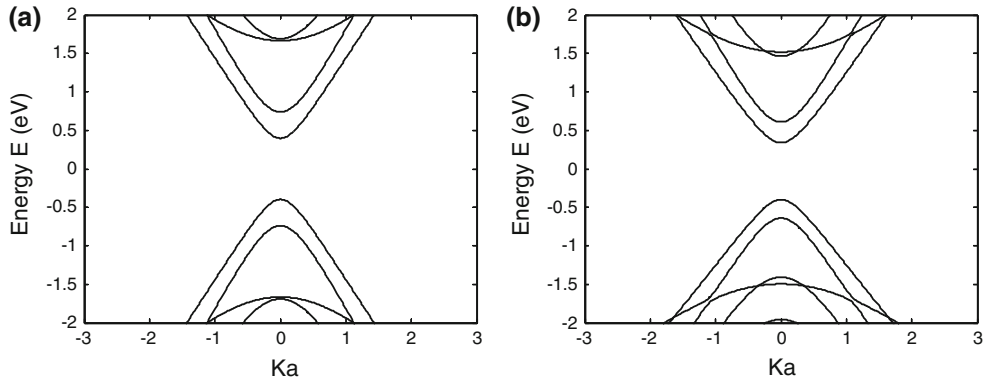

Figure 2 Energy band structure of an *N* = 13 armchair graphene nanoribbon, a obtained from the first nearest-neighbour tight binding method and b including third nearest-neighbours.

boundary conditions are included through the left and right self-energy matrix elements, $\Sigma^{L,R}$. The self-energies are independently evaluated through an iterative scheme described by Sancho et al. [11], modified to include third nearest-neighbour interactions. Determination of the retarded Green's function through equation 5 is facilitated by the inclusion of the body of the device in the right-hand contact through the recursive scheme described in ref. [15]. We will now outline the numerical procedure for deriving the conductance with third nearest-neighbour interactions included. Figure 3 shows a schematic of the unit cell labelling used to formulate the Green's function.

We calculate the surface retarded Green's functions of the left and right leads by

$$g^{L}_{0,0} = [E^{+}S_{0,0} - H_{0,0} - (E^{+}S_{0,-1} - H_{0,-1})\tilde{\theta}]^{-1} \quad (6)$$

$$g^{R}_{M+1,M+1} = [E^{+}S_{0,0} - H_{0,0} - (E^{+}S_{-1,0} - H_{-1,0})\theta]^{-1} \quad (7)$$

where θ and $\tilde{\theta}$ are the appropriate transfer matrices calculated from the following iterative procedure.

$$\theta = t_0 + \widetilde{t_0}t_1 + \widetilde{t_0}\widetilde{t_1}t_2 + \cdots + \widetilde{t_0}\widetilde{t_1}\widetilde{t_2}\cdots t_n \quad (8)$$

$$\tilde{\theta} = \widetilde{t_0} + t_0\widetilde{t_1} + t_0t_1\widetilde{t_2} + \cdots + t_0t_1t_2\cdots\widetilde{t_n} \quad (9)$$

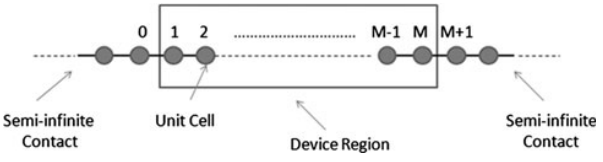

Figure 3 Schematic showing the unit cell labelling used to formulate the Green's function.

where t_i and $\widetilde{t_i}$ are defined by

$$t_i = (I - t_{i-1}\widetilde{t_{i-1}} - \widetilde{t_{i-1}}t_{i-1})^{-1}t^2_{i-1} \quad (10)$$

$$\widetilde{t_i} = (I - t_{i-1}\widetilde{t_{i-1}} - \widetilde{t_{i-1}}t_{i-1})^{-1}\widetilde{t_{i-1}}^2 \quad (11)$$

and

$$t_0 = (E^{+}S_{0,0} - H_{0,0})^{-1}(E^{+}S_{0,-1} - H_{0,-1}) \quad (12)$$

$$\widetilde{t_0} = (E^{+}S_{0,0} - H_{0,0})^{-1}(E^{+}S_{-1,0} - H_{-1,0}) \quad (13)$$

The process is repeated until $t_0\widetilde{t_0} < \delta$ with δ arbitrarily small. The nonzero elements of the self-energies $\Sigma^{L}_{1,1}$ and $\Sigma^{R}_{M,M}$ can be then obtained by

$$\Sigma^{L}_{1,1} = (E^{+}S_{1,0} - H_{1,0})g^{R}_{0,0}(E^{+}S_{0,1} - H_{0,1}) \quad (14)$$

$$\Sigma^{R}_{M,M} = (E^{+}S_{0,1} - H_{0,1})g^{R}_{M+1,M+1}(E^{+}S_{1,0} - H_{1,0}) \quad (15)$$

The conductance is obtained from the relation

$$G(E) = \frac{2e^2}{h}T(E) \quad (16)$$

where the transmission coefficient is obtained from

$$T(E) = Tr[\Gamma^{L}G\Gamma^{R}G^{\dagger}], \quad (17)$$

with $\Gamma^{L,R} = i[\Sigma^{L,R} - (\Sigma^{L,R})^{\dagger}]$.

Figure 4a, b compares the conductance of a graphene armchair-edge nanoribbon of index N = 13 and metal/semiconductor junction formed with the nanoribbon

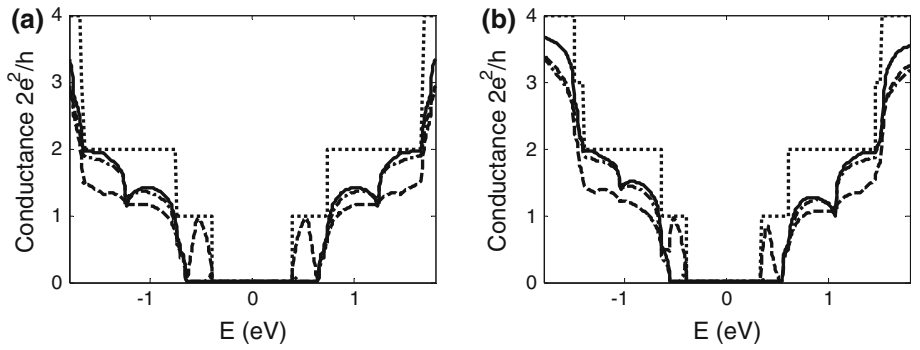

Figure 4 Conductance vs Energy for the junction shown in Figure 1, a using first nearest-neighbour parameters and b using third nearest-neighbours parameters. *Dotted lines* are for $N = 13$ armchair nanoribbon, *solid lines* are for ideal metal/semiconductor junctions, *dot–dash lines* and *dash lines* are for junctions with a single defect type A (*triangle* in Figure 1) and type B (*rectangle* in Figure 1) respectively.

assuming first and third nearest-neighbour interactions, respectively. For graphene nanoribbons, differences are observed in the step-like structure, reflecting differences in the calculated band structure. When only first nearest-neighbour interactions are considered, the conductance of the conduction and valence bands is always symmetrical as determined by the formulation of the energy dispersion relation, equation 1. In the case of graphene nanoribbons, the conductance within a few electron volts of the Fermi energy is symmetrical for both first and third nearest-neighbour interactions. However, it is notable that at higher energies, overlap integrals introduced by third nearest-neighbour interactions result in asymmetry between the conductance in the conduction and valence bands. For metal/semiconductor junctions, significant differences in conductivity occur even at low energies due to mismatches of the sub-bands. Asymmetry in the conduction and valence band conductance (absent for first nearest-neighbour interactions) is also apparent when third nearest-neighbour interactions are included in the Green's function. Differences are also seen when defects are incorporated within a metal/semiconductor junction, an interesting system explored by Hong et.al. [12]. In this work, vacancies are introduced in the lattice at the positions marked by the solid rectangle and triangle in Figure 1 and the conductance obtained in each case. Hong et al. derive a coupling term associated with differences in band structure. For third nearest-neighbour, the solution to the coupling strength must be derived numerically.

Conclusions

In this paper, we have determined the energy band structure of graphene nanoribbons and conductance of nanoribbons and graphene metal/semiconductor junctions using a NEGF formalism based on the tight binding method approximated to first nearest-neighbour and third nearest-neighbour. Significant differences are observed, suggesting the commonly used first nearest-neighbour approximation may not be sufficiently accurate in some circumstances. The most notable differences are observed when defects are introduced in the metal/semiconductor junctions.

Received: 9 July 2010 Accepted: 9 September 2010
Published: 7 October 2010

References

1. Novoselov KS, *et al*: **Two-dimensional gas of massless Dirac fermions in graphene.** *Nature* 2005, **438**:197-200.
2. Cresti A, *et al*: **Charge transport in disordered graphene-based low dimensional materials.** *Nano Res* 2008, **1**:361-394.
3. Neto A, *et al*: **The electronic properties of graphene.** *Rev Mod Phys* 2009, **81**:109-162.
4. Golizadeh-Mojarad R, *et al*: **Atomistic non-equilibrium Green's function simulations of Graphene nano-ribbons in the quantum hall regime.** *J Comput Electron* 2008, **7**:407-410.
5. Liang G, *et al*: **Ballistic graphene nanoribbon metal-oxide-semiconductor field-effect transistors: a full real-space quantum transport simulation.** *J Appl Phys* 2007, **102**:054307.
6. Zhao P, Guo J: **Modeling edge effects in graphene nanoribbon field-effect transistors with real and mode space methods.** *J Appl Phys* 2009, **105**:4503.
7. Odili D, *et al*: **Modeling charge transport in graphene nanoribbons and carbon nanotubes using a Schrödinger-Poisson solver.** *J Appl Phys* 2009, **106**:024509.
8. Saito R, *et al*: **Physical Properties of Carbon Nanotubes.** Imperial College Press, London; 1998.
9. Chen J, *et al*: **Low-energy electronic states of carbon nanocones in an electric field.** *Nano Micro Lett* 2010, **2**:121-125.
10. Reich S, *et al*: **Tight-binding description of graphene.** *Phys Rev B* 2002, **66**:035412.
11. Sancho M, *et al*: **Quick iterative scheme for the calculation of transfer matrices: application to Mo (100).** *J Phys F: Metal Phys* 1984, **14**:1205-1215.
12. Hong S, *et al*: **Metal-semiconductor junction of graphene nanoribbons.** *Appl Phys Lett* 2008, **92**:083107.
13. Nakada K, *et al*: **Edge state in graphene ribbons: nanometer size effect and edge shape dependence.** *Phys Rev B* 1996, **54**:17954-17961.

14. Kundu R: **Tight binding parameters for graphene.** 2009, Arxiv preprint arXiv:0907.4264.
15. Li TC, Lu S-P: **Quantum conductance of graphene nanoribbons with edge defects.** *Phys Rev B* 2008, **77**:085408.
16. Datta S: *Quantum Transport: Atom to Transistor* Cambridge University Press, Cambridge; 2005.

doi:10.1007/s11671-010-9791-y
Cite this article as: Wu and Childs: **Conductance of Graphene Nanoribbon Junctions and the Tight Binding Model.** *Nanoscale Res Lett* 2011 **6**:62.